STRATEGIES TO TUNE ACTIVE SITE ENVIRONMENTS FOR ALKENE EPOXIDATIONS WITH H_2O_2 OVER SUPPORTED TRANSITION METAL ATOMS

BY

ECE ZEYNEP AYLA

DISSERTATION

Submitted in partial fulfillment of the requirements
for the degree of Doctor of Philosophy in Chemical Engineering
in the Graduate College of the
University of Illinois Urbana-Champaign, 2022

Urbana, Illinois

Doctoral Committee:

Professor David W. Flaherty, Chair
Professor Baron G. Peters
Professor Paul J.A. Kenis
Professor Catherine J. Murphy

ABSTRACT

Atomically dispersed transition metal atoms within zeolite frameworks or grafted to surfaces of catalytically inactive mesoporous supports can activate hydrogen peroxide (H_2O_2) to form intermediates that selectively epoxidize alkenes, including propylene. Despite being reported four decades in the past, titanium-silicalite 1 remains the most widely used and benchmark heterogeneous catalyst for this chemistry. Principles to guide the development of more productive and selective dispersed metal catalysts remain elusive. Reported turnover rates, activation barriers, and the reasons for differences among ostensibly similar sets of materials often disagree across studies. These discrepancies may reflect unrecognized structural distinctions between catalysts or consequential differences among the catalytic conditions used. This report examines the electronic and topological factors that control rates, selectivities, and apparent activation enthalpies for alkene epoxidations with H_2O_2 by examining series of Groups 4–6 metals incorporated into the BEA zeolite framework and Ti atoms grafted onto non-microporous supports. Measurable electronic properties (inner-sphere interactions) and excess thermodynamic contributions (outer-sphere interactions) at or near the metal active site, assessed quantitatively by spectroscopic and calorimetric methods, correlate strongly with rates, selectivities and activation barriers. **Chapter 1** reviews the importance of inner- and outer-sphere interactions that control energy barriers for epoxidation. These interactions can be decoupled and manipulated through choice of the reactive metal, selection of the supporting oxide, and size of the substrate in relation to confined catalytic environments. This is followed by a discussion of extending the understanding of these interactions to more complex active site environments for enantioselective epoxidation and direct epoxidation of propene in Au/Ti-zeolite catalysts with H_2 and O_2.

Rates and selectivities for alkene epoxidations depend sensitively on the identity of the active metal center for both heterogeneous and homogeneous catalysts. While group 6 metals (Mo, W) have greater electronegativities and the corresponding molecular complexes have greater rates for epoxidations than group 4 or 5 metals and molecular complexes, these relationships are not established for zeolite catalysts. **Chapter 2** combines complementary experimental methods to determine the effects of metal identity on the catalytic epoxidation of 1-hexene with H_2O_2 for active sites within the BEA framework. Post-synthetic methods were used to incorporate groups 4−6 transition-metal atoms (Ti, Nb, Mo, W) into the framework of zeolite BEA. In situ Raman and UV−vis spectroscopies show that H_2O_2 activates to form peroxides (M-(η_2-O_2)) and hydroperoxides (M-OOH) on all M-BEA but also metal-oxos (M=O) on W- and Mo-BEAs, the latter of which leaches rapidly. Changes in turnover rates for epoxidation as functions of reactant concentrations and the conformation of cis-stilbene epoxidation products indicate that epoxide products form by kinetically relevant O-atom transfer from M-OOH or M-(η_2-O_2) intermediates to the C=C bond and show two distinct kinetic regimes where H_2O_2-derived intermediates or adsorbed epoxide molecules prevail on active sites. Ti-BEA catalyzes epoxidations with turnover rates 60 and 250 times greater than Nb-BEA and W-BEA, which reflect apparent activation enthalpies ($\Delta H^{\ddagger}$) for both epoxidation and H_2O_2 decomposition that are lower for Ti-BEA than for Nb- and W-BEAs. Values of $\Delta H^{\ddagger}$ for epoxidation differ much more between metals than barriers for H_2O_2 decomposition and give rise to large differences in 1-hexene epoxidation selectivities that range from 93% on Ti-BEA to 20% on W-BEA. Values of $\Delta H^{\ddagger}$ for both pathways scale linearly with measured enthalpies for adsorption of 1,2-epoxyhexane from the solvent to active sites measured by isothermal titration calorimetry. These correlations confirm that linear free-energy relationships hold for these systems, despite differences in the coordination of active metal

atoms to the BEA framework, the identity and number of pendant oxygen species, and the complicating presence of solvent molecules.

Chapter 3 investigates the deconvolution of inner- and outer-sphere effects by examining atomically disperse Ti sites on metal oxides (MO_x, including SiO_2, γ-Al_2O_3, ZnO, GeO_2) that activate H_2O_2 to create intermediates active for alkene epoxidations. Turnover rates for 1-hexene epoxidation in acetonitrile vary 1000-fold at identical conditions due to differences in apparent activation enthalpies ($\Delta H^{\ddagger}_{epox}$) and entropies ($\Delta S^{\ddagger}_{epox}$). Ligand-to-metal charge transfer energies and vibrational frequencies of reactive species assessed by *in situ* UV-Vis and Raman spectroscopy, respectively, indicate supports do not detectably change electronic properties of H_2O_2-derived intermediates. However, isoelectric points and solution-phase water uptakes for these metal oxides correlate with $\Delta H^{\ddagger}_{epox}$ and suggest that non-covalent interactions at the solid-liquid interface influence the stability of epoxidation transition states. Supports with lower pK_a values concentrate water near the solid-liquid interface and enthalpically stabilize the transition state. These findings illustrate that outer sphere interactions impact epoxidation reactions upon metal oxide catalysts including titanium silicates.

Interactions among fluid-phase molecules, reactive intermediates, and solid surfaces contribute to apparent activation barriers for alkene epoxidations with H_2O_2 through outer sphere interactions, which lead to differences in turnover rates even in the absence of a bulk liquid-phase. **Chapter 4** demonstrates the significance of these interactions through comparisons of the kinetics for gas-phase epoxidations of alkenes (C_3-C_{10}) over Ti atoms substituted within the framework of BEA* zeolite. The microporous and hydrophilic environment of zeolite BEA induces capillary condensation and stabilizes liquid-like densities of solvent molecules (e.g., CH_3CN) nearby Ti-atom active sites. Although the reaction mechanism, dominant reactive intermediates, and

kinetically relevant steps remain identical as the alkyl chain length increases for C_3H_6 to $C_{10}H_{20}$, the turnover rates differ by a factor of 30-fold. Formation of epoxidation transition states disturbs these solvating molecules, which leads to changes in apparent activation enthalpies **(**$\Delta H^{\ddagger}$) and entropies ($\Delta S^{\ddagger}$) that change with a complex dependence on the number of methylene groups (-CH_2-) within the alkene. Moreover, we observe less solvent (CH_3CN) displacement with shorter alkyl chains, indicating a greater number of molecular interactions between reactants, solvent, and catalyst pore walls for smaller substrate molecules. These changes influence excess enthalpies and entropies which are reflected in the free energy of epoxidation transition states, leading to differences in turnover rates. These results provide guidelines to control the effects of fluid-solid interactions near catalytic active sites, which control the free energies of intermediate states that impact apparent activation barriers for epoxidation reactions in microporous environments.

Chapter 5 reviews the findings from **Chapters 2-4** on the effects of inner- and outer-sphere interactions on selective liquid- and vapor-phase alkene epoxidation with H_2O_2 over transition metal atoms dispersed on solid metal oxides. **Chapter 5** also includes proposals for potential future investigations to further explore active site environments, specifically for (1) enantioselective epoxidation with H_2O_2 on supported group 5 transition metals as well as (2) direct propylene epoxidation from H_2 and O_2 over TS-1 supported metal nanoparticles. Enantioselective chemistry is important to produce biologically active molecules used in the manufacture of drugs and other pharmaceuticals. Enantioselective catalysis combines the effects of electronic and solvent structure at or near the active site with the presence of chiral ligands or an inherently chiral catalyst. Moreover, insight into the direct epoxidation propylene with H_2 and O_2 over Au-incorporated Ti-zeolites motivates examination of multiple active site environments in proximity and will provide tools to evaluate similar concurrent tandem or “one-pot” catalytic systems. The

vapor-phase epoxidation system and methods already developed, introduced in detail in **Chapter 4**, allow for facile experimental set-up for this study. These future projects examine industrially relevant-chemistries that add another level of complexity to active site surroundings and will provide additional insight into understanding the influence of inner- and outer-sphere effects on oxidation catalysis.

Collectively, these studies explore methods to deconvolute inner- and outer-sphere effects that influence electronic and excess thermodynamic properties of active site environments for alkene epoxidations with H_2O_2 over supported transition metal atoms. The kinetic, spectroscopic, and calorimetric methods introduced can be further applied to provide design principles for the design of solid catalysts for various industrial reactions.

To tall peppermint mochas, ½ pump mocha, 1 pump pep

ACKNOWLEDGEMENTS

Cramming a lifetime of experience, adventure, and friendships into the last sixty months wasn't easy, and not something I could have done alone. My advisor, mentors, lab mates, colleagues, friends, and family made my second home, Davenport Hall and Roger Adams Laboratory at the department of Chemical and Biomolecular Engineering at University of Illinois Urbana-Champaign, more than bearable for the past five years.

My advisor, Professor David Flaherty, has been nothing less than an inspiring scientific leader, and I thank him for his patience throughout my journey to become a researcher and appreciate the hours of work he has put in to provide extremely thorough feedback for all of my manuscripts, conference abstracts, and presentations. His eye for detail in technical communication and effort to deliver meticulous feedback will always be qualities I strive for.

Thank you to my lab mates, past and present, who made graduate school a stepping-stone to not only my career, but to the rest of my life. There is no doubt that you all are friends first, colleagues second. It's hard to imagine that the current Flaherty lab alumni were only 2nd, 3rd, 4th, and 5th year graduate students when I first met them, and I am grateful for their support and mentorship throughout the years. Thank you to Andy, Neil, Megan, Pranjali, Daniel, Yao, Abinaya, and Jason for taking the time to patiently answer the countless questions I had during some of the most stressful years of your careers. I learned so much from all of you – almost as much as my current colleagues, who I have spent the last several years working alongside, who stayed by side at my best and at my worst. Thank you to Tom for always being ready and available to answer my random questions and providing thoughtful feedback, sometimes even several days later when you've been thinking longer about my question than I have. Claudia, you are an inspiring leader and friend, thank you for valuing everyone else's success just as much as your

own. Thank you to Chris for your friendship and encouragement, and for the breakfast burritos I didn't know I needed, I admire all your efforts to be the friend everyone not only wants, but also needs. Thank you Yangsik, for all your help and for being a super supportive colleague. Thank you to Danim for all our conversations, all your positivity and support, I appreciate your trust and your friendship. Thank you Ohsung for all the time and effort you put into the gas-phase epoxidation system, for allowing me to talk and vent about so many things, and for always responding positively to my jokes. Thank you, David, for your willingness to spend hours discussing entropic changes (I think I finally understand it now), but also for your endless encouragement and reassurance through some of the most difficult times of grad school. The pandemic has been difficult for all of us, but I applaud Matt, Jieun, Richa, Suchi, and Vijay for their hard work and progress during their first couple of years and am excited to see their success as a part of the lab and beyond. Finally, thank you to my undergraduate mentees, Arzam and Darshan for your curiosity and hard work. Thank you to all for the great times we've had in and out of lab.

Thanks to all of my friends in Champaign-Urbana and my friends everywhere else for making the ending to an exceptionally stressful last five years, a bittersweet one. A huge thank you to David and Ohsung for training with me and pushing me to run not one, but TWO, half-marathons with me, and Yash for planning and guiding us through several road trips to make it happen. Also, thank you to the entire "friends' dinner" crew for having a wholesome weekly tradition to look forward to and to Yash for making spicy food tolerable and worth the pain. Thank you to all friends who helped make the big yellow house a ChBE home for the past several years and to all my roommates, with whom I've had the pleasure of sharing a space, stories, and adventures. I can't imagine the last five years without all of you, and also my friends who

supported me from thousands of miles away. Thank you to my best friend Rathna for being one of the most reliable, compassionate, and rational sources of comfort for the past decade. My friends, Morgan, Tyler, Merced, and Jack, thank you for the late-night phone calls, the spontaneous trips all over the country, and for being my connection to the "real-world" to keep me, a perpetually panicking grad student, grounded.

Special thanks to Adam for emphasizing the importance of certain chemical reactions (e.g., Maillard) over alkene epoxidation, but most importantly for providing the most honest and selfless patience, reassurance, and support during some of the most bizarre and uncertain times of the last a few years. Finally, my biggest inspiration for kindness, patience, and hard work is my family. Working tirelessly with very little, my parents showed me the value of determination in the face of countless obstacles, and I could not have even dreamed to be where I am without their example. My sister Müge, my second parents, Nurcan bacı and dad, my uncles, Ali bey and dayı bey, and my aunt Neslihan teyzecim, thank you for your love and support. I owe my family and friends a great part of my strength, hope, and accomplishments during my Ph.D.

Thank you to everyone who I have met, and have yet to meet, who motivates me to become a better scientist, researcher, colleague, friend, and person.

The work presented in this thesis was supported by the U.S. Army Research Office under grant number W911NF-18-1-0100. I also acknowledge the SURGE Fellowship from The Grainger College of Engineering and the Frederick Seitz Materials Research Laboratory Central Research Facilities at the University of Illinois at Urbana-Champaign.

TABLE OF CONTENTS

CHAPTER 1: INTRODUCTION 1

CHAPTER 2: TUNING THE ELECTRONIC PROPERTIES OF GROUPS 4-6 METAL-SUBSTITUTED BEA ZEOLITES: REACTIVE INTERMEDIATES, REACTION PATHWAYS, AND LINEAR FREE ENERGY RELATIONSHIPS 8

CHAPTER 3: IDENTITY OF METAL OXIDE SUPPORT CONTROLS OUTER SPHERE INTERACTIONS THAT AFFECT RATES AND BARRIERS FOR ALKENE EPOXIDATION AT ISOLATED TI ATOMS 46

CHAPTER 4: EFFECTS OF ALKYL CHAIN LENGTH ON VAPOR-PHASE ALKENE EPOXIDATIONS WITH H_2O_2 OVER TI-BEA 73

CHAPTER 5: CONCLUSIONS AND FUTURE DIRECTIONS.....93

REFERENCES.....104

APPENDIX A: SUPPLEMENTAL DATA AND ANALYSIS FOR CHAPTER 2.....116

APPENDIX B: SUPPLEMENTAL DATA AND ANALYSIS FOR CHAPTER 3 132

APPENDIX C: SUPPLEMENTAL DATA AND ANALYSIS FOR CHAPTER 4.....145

APPENDIX D: SUPPLEMENTAL DATA AND ANALYSIS FOR CHAPTER 5 FUTURE DIRECTIONS…….....157

CHAPTER 1

INTRODUCTION

Epoxides are essential functional groups and precursors used in the production of plastics, pharmaceuticals, fragrances, and several other fine and commodity chemicals, making up a greater than 60-billion dollar industry.[1, 2] The epoxidation of alkenes creates polymer building blocks (e.g., propylene glycol, polyurethane polyols, etc.) for the manufacture of various everyday products.[3, 4] Optimizing any industrial process commonly involves exploring environment-friendly alternatives (e.g., resources, techniques, etc.) to manufacture high-demand chemicals. Propylene oxide (PO) is one of the most widely produced epoxides, with more than 10 million tons produced annually.[4] Many methods for PO production (in addition to other epoxides) employ processes which utilize caustic reactants (organic peroxides) and create toxic co-products (e.g., aqueous Cl_2, HOCl) that must be chemically remediated prior to disposal. Specifically, the Halcon and Sumitomo processes utilize organic hydroperoxides (e.g., ethylbenzene hydroperoxide, cumene hydroperoxide, etc.) with soluble Mo-based catalysts and the chlorohydrin process requires the use of chlorine and produces chlorinated salts as byproducts.[5, 6] These processes rely on dated technologies that are hazardous to both humans and the environment. For example, in August 2017, a large explosion at an Arkema chemical plant in Houston, Texas[7] resulted from the improper storage of organic peroxides that could have been avoided by replacing the organic peroxides with a safer, more environmentally conscious, alternative.

Hydrogen peroxide (H_2O_2) is one such alternative that can produce epoxides and has the advantage of only forming H_2O as a byproduct while promoting an overall inherently safer design for PO production. The focus of this dissertation is inspired by the use of titanium zeolites, which have paved the way for the selective and environment-friendly epoxidation of propylene with

hydrogen peroxide in the Hydrogen Peroxide Propylene Oxide (HPPO) process.[6, 8] Here, we examine the catalytic properties that make Ti-zeolites highly successful epoxidation catalysts and how they can be applied to similar catalytic systems.

The kinetic, calorimetric, and spectroscopic tools developed in this study investigate well-defined active site environments for alkene epoxidation with H_2O_2 over solid transition metal atom catalysts. The electronic and molecular interactions that occur at or near active sites can influence rates and selectivities for various catalytic reactions, including epoxidation. These interactions contribute to changes in free energy that occur to form the transition state for alkene epoxidation with H_2O_2. The change in free energy during transition state formation, $\Delta G^{\ddagger}$, relies on the differences in the standard state free energies, $\Delta G^{\ddagger,0}$, and excess free energies, $\Delta G^{\ddagger,\varepsilon}$, of reactants (Equation 1.1).

$$\Delta G^{\ddagger} = \Delta G^{\ddagger,0} + \Delta G^{\ddagger,\varepsilon} \tag{1.1}$$

Inner-sphere interactions lead to $\Delta G^{\ddagger,0}$ and commonly involve the electronic properties of the active site. For epoxidation reactions catalyzed by supported transition metals, the pendant oxygen ligands, derived from H_2O_2 and covalently bound to transition metal centers, constitute a majority of inner-sphere interactions. These electronic properties can be directly manipulated by changing the elemental identity of the active metal atom.[9, 10] Outer-sphere interactions are a direct result of reactant and solvent reorganization during transition state formation and contribute to $\Delta G^{\ddagger,\varepsilon}$.[11, 12] To deconvolute these contributions it is helpful to visualize the free energies of kinetically relevant step in a reaction coordinate diagram (Scheme 1.1).

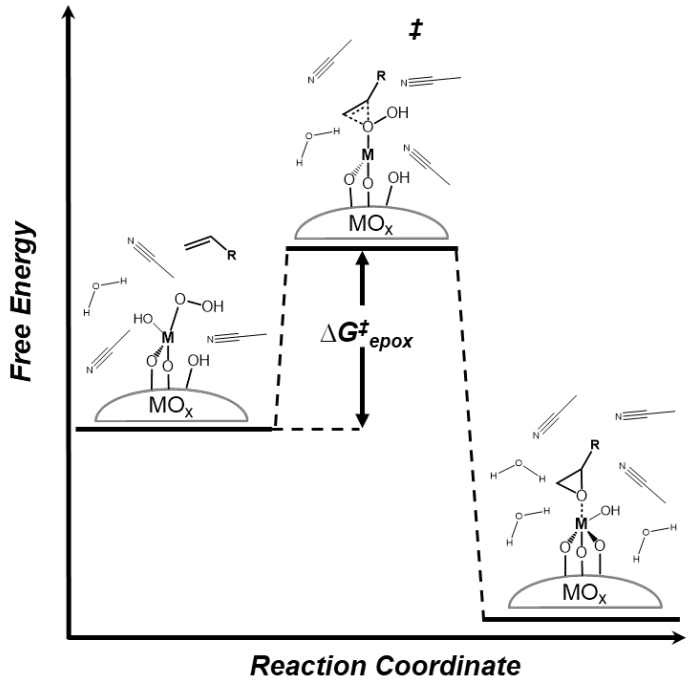

Scheme 1.1. Reaction coordinate diagram for the formation of the transition state for C_nH_{2n} epoxidation by reaction between fluid-phase C_nH_{2n} and M-OOH over a metal oxide supported transition metal catalyst. The physical states that correspond to the value of $\Delta G^{\ddagger}_{epox}$ is depicted.

For alkene epoxidation over a supported metal catalyst, we must consider the free energies of the transition state in addition to the alkene and a reference state, which in this case is a metal-hydroperoxo surface intermediate (Equation 1.2).

$$\Delta G^{\ddagger}_{epox} = G^{\ddagger} - G_{alkene} - G_{Ti\text{-}OOH} \quad (1.2)$$

These free energy values reflect deviations from the standard or initial free energy of the components and fluctuations due to excess enthalpic and entropic gains or losses (Equation 1.3).

$$\Delta G^{\ddagger}_{epox} = (G^{0,\ddagger} + G^{\varepsilon,\ddagger}) - (G^{0}_{alk} + G^{\varepsilon}_{alk}) - (G^{0}_{Ti\text{-}OOH} + G^{\varepsilon}_{Ti\text{-}OOH}) \quad (1.3)$$

Studies identified properties of the active site (e.g., electrophilicity, Lewis acid strength, etc.) and its surroundings (e.g., surface hydrophilicity, micropore size, solvent identity, etc.) that influence thermodynamic contributions. This dissertation aims to further deconvolute these contributions by exploring alkene epoxidation chemistry over supported transition metal catalysts to improve understanding towards tuning specific interactions that make fast and selective epoxidation catalysts.

Several studies report the effects of the identity of active metal on electronic properties of active sites.[10, 13, 14] Bregante et al. describe a trend for groups 4-5 transition metal in zeolite BEA shows that the cyclohexene epoxidation activation barrier decreases as the electron affinity or Lewis acid strength of the active site increases, primarily due to differences in the electrophilicity of the reactive oxygen intermediates that form when H_2O_2 is activated.[10] A similar study by Thornburg et al. correlates the Pauling electronegativity of highly disperse groups 4-5 transition metal atoms grafted onto SiO_2 with rates and selectivities for cyclohexene and styrene epoxidation with H_2O_2.[13] Work from Maksimchuk and coworkers showed a similar trend but for polyoxometallates, where they claim that Nb's higher oxidation state allows the metal center to be more readily reduced, making it more electrophilic for alkene oxidation.[14] Following these trends which suggest increasing active metal electronegativity favors epoxidation, **Chapter 2** aims to further improve epoxidation rates and selectivities by comparing the more electronegative group 6 metals in zeolite BEA to their groups 4 and 5 counterparts. Group 6 metals Mo and W are highly successful epoxidation catalysts as homogeneous complexes[15, 16] but are less studied on solid supports due to reports of severe leaching. **Chapter 2** reveals Pauling electronegativity to be a weak predictor of the catalytic activity for groups 4-6 transition metals (Ti, Nb, W) incorporated into zeolite BEA. However, the work defines *in situ* spectroscopic and calorimetric methods to

quantify the Lewis acidity and electron affinity for these active metal centers as they exist in the BEA framework under reaction conditions. A linear free energy relationship is established between apparent activation enthalpies ($\Delta H^{\ddagger}_{epox}$) for 1-hexene epoxidation and the heats of adsorption of 1,2-epoxyhexane ($\Delta H^{\ddagger}_{ads,epox}$) on active metal atoms as a way to better quantify and describe electronic properties and inner-sphere interactions of supported transition metal atoms in distinct catalytic systems and under specific reaction conditions.

In the past, several groups have studied the modification of catalyst surfaces with the additions of methyl- or metal-based ligands or promoters as extensions of the surface to modify the Lewis acidity of active metal centers. This has been studied for epoxidation with homogeneous complexes[17], as well as heterogeneous complexes[18] and these modifications have led to significant differences in epoxidation rates (as much as 3-fold) and selectivities, likely as a result of changing charge density near the active site. However, these somewhat complex structures have the disadvantages of being unstable at high temperatures or easily deactivated during catalysis. Moreover, it is unclear whether these differences in activity are due to electronic or steric effects from the added bulky ligands. **Chapter 3** proposes to simplify the surface modifications by studying atomically disperse Ti atoms on metal oxide surfaces (SiO_2, γ-Al_2O_3, ZnO, and GeO_2) to decouple inner- and outer-sphere effects resulting from varying the chemical identity of the active site surroundings, while maintaining the elemental identity of the active metal center. *In situ* Raman and UV-Vis spectroscopy examines the electronic interactions between the active site and reactive intermediates and confirms no observable differences in inner-sphere interactions when H_2O_2 is activated on Ti atoms supported on different the different metal oxides. Correlations of apparent activation enthalpies for 1-hexene epoxidation with values of isoelectric point and water uptake with NMR spectroscopy show that more acidic metal oxide surfaces tend to agglomerate

water near the surface which favors lower energy barriers for epoxidation. These observations also indicate that outer-sphere interactions due to solvent reorganization, rather than inner-sphere interactions due to covalent bonding structure, are the primary contributors to the differences in transition state free energies when Ti atoms are supported on different metal oxides.

Finally, an extensive study from our group of outer-sphere effects shows that Ti-BEA zeolites yield higher turnover rates with the increased presence of water and silanol defects in the zeolite pores.[19] Other groups also report the impact of solvent interactions and properties on hydrogenation[20] and propylene epoxidation rates[21] in transition metal zeolites. These results indicate solid-fluid interactions provide excess contributions which are reflected in epoxidation free energies and rates of reaction. The adoption of H_2O_2 for specific epoxidation reactions (and not just PO) requires the design of increasingly active and selective catalysts that can be tailored to the substrate geometry. **Chapter 4** examines the effects of increasing alkene chain length on excess thermodynamic contributions that affect energy barriers and turnover rates for epoxidation in the vapor-phase. Studying the reaction in the absence of bulk-solvent helps decouple outer-sphere interactions that occur as solvent molecules reorganize during transition state formation. *In situ* infrared spectroscopy can quantify displaced CH_3CN, disrupted H-bonds, and intrapore epoxide to provide evidence for the several sources of excess entropic contributions in these catalytic environments.

Chapter 5 summarizes the findings about the effects of the identity of the active metal, the metal oxide support, and the linear alkene substrate on inner- and outer-sphere interactions that influence reaction free energies which ultimately determine rates and selectivities for transition metal-catalyzed epoxidation reactions with H_2O_2. Chapters 2-4 demonstrate the decoupling of standard state and excess properties to influence apparent activation enthalpies for transition state

formation in liquid- and vapor-phase reaction environments. In **Chapter 2**, we establish a linear free energy relationship that shows elemental identity of the transition metal centers in zeolite BEA controls the Lewis acid strength of the active sites, resulting in lower epoxidation energy barriers for incorporated metals exhibiting greater electron affinity. **Chapter 3** shows outer-sphere interactions (excess thermodynamic contributions) dominate free energy differences when Ti atoms are supported on various metal oxides. *In situ* UV-Vis, Raman, and NMR spectroscopic studies confirm that changing support identity modifies intermolecular interactions near the active site rather than the covalent interactions between the active metal and reactive intermediates to influence $\Delta G^{\ddagger}_{epox}$ in aqueous environments. **Chapter 4** details the design and development of a vapor-phase epoxidation system to examine the differences in excess entropic contributions that result from solvent reorganization and displacement as alkenes of varying chain length enter the zeolite micropore and react with surface oxygen species (i.e., Ti-OOH) to form the epoxidation transition state. Finally, future work can apply these techniques to decouple inner- and outer-sphere interactions in active site environments for enantioselective epoxidations as well as the epoxidation of propylene with the *in situ* synthesis of H_2O_2 in the presence of H_2 and O_2. In situ site titrations and spectroscopic tools can be used to characterize chiral active sites required for enantioselective epoxidation to assess thermodynamic contributions of various chiral ligands used to modify enantioselective catalysts. Additionally, coupling the vapor-phase epoxidation system with *operando* spectroscopy allows for a detailed investigation of reactive intermediates that form to produce H_2O_2 and the propylene oxide on Au and Au alloy nanoparticle and Ti-zeolite surfaces, respectively. The combination of kinetic, calorimetric, and spectroscopic techniques developed in this work can improve understanding of solid catalytic systems and provide design principles for the next generation of industrial epoxidation catalysts.

CHAPTER 2

TUNING THE ELECTRONIC PROPERTIES OF GROUPS 4-6 METAL-SUBSTITUTED BEA ZEOLITES: REACTIVE INTERMEDIATES, REACTION PATHWAYS, AND LINEAR FREE ENERGY RELATIONSHIPS[i]

2.1 Introduction

Epoxides are important precursors for the production of performance solvents, solutions, materials, and biologically active ingredients within the food, cosmetic, construction, automobile, and pharmaceutical industries.[3] The synthesis and characterization of a catalyst comprised of titanium substituted into the framework of MFI zeolite (i.e., titanium- silicate-1, TS-1) by ENI in 1983 gave rise to the use of hydrogen peroxide (H_2O_2) as an environmentally benign alternative to chlorine and organic hydroperoxides for the production of propylene oxide The success of this system continues to motivate the development of new transition metal - silicate catalysts,[13, 22-26] integrated processes,[27-29] and investigations of fundamental surface chemistry for the epoxidation of alkenes with H_2O_2.[24, 30, 31] Recent finding show that rates and selectivities for epoxidations with H_2O_2 depend strongly upon the identity of the active transition metal[10, 13] and the topology, pore size, and the silanol density of the silicate support.[19, 22, 30] These attributes influence the form and

---

i This chapter has been reproduced, with permission, from the following publication:
E. Zeynep Ayla, David S. Potts, Daniel T. Bregante, and David W. Flaherty, "Alkene Epoxidations with H_2O_2 over Groups 4–6 Metal-Substituted BEA Zeolites: Reactive Intermediates, Reaction Pathways, and Linear Free-Energy Relationships", *ACS Catalysis,* **2021**, 11, 1, 139-154.

electronic structure of H_2O_2-derived intermediates and solvent-mediated interactions among reactive species and the extended surface of the silicate support.

Early transition metals activate H_2O_2 for epoxidations.[32] Groups 4 and 5 metals (Ti, Nb, Ta) grafted onto mesoporous supports,[23, 31, 33, 34] incorporated into zeolite frameworks[10, 25, 26, 35] or as polyoxometalates (POMs)[36-39] have been widely studied to examine the effects of active metal identity on epoxidation catalysis over solid materials. The electron affinity of the active metal atom likely impacts catalysis by influencing the electrophilicity of reactive forms of oxygen bound to active sites. In agreement with intuition, the electronic properties of active sites for these catalysts depend strongly on those of the associated transition metals and influence activation enthalpies for epoxidation. Multiple studies have shown that more electrophilic reactive intermediates epoxidize alkenes with greater turnover rates.[10, 13, 40] Ti, Nb, Ta, Zr, and Hf in framework sites of zeolite BEA all form metal-peroxo (M-(η^2-O_2)) and metal-hydroperoxo (M-OOH) structures from H_2O_2, however, turnover rates for epoxidation are as much as 5000-, 100-, and 50-fold higher on Ti-based catalysts than on analogous Zr- or Hf-, Ta- and Nb-based catalysts, respectively.[10, 23] The ligand-to-metal charge transfer (LMCT) energies of these reactive intermediates serve as a quantitative measure of the electrophilicity of reactive oxygen species and can be determined by *in situ* UV-Vis spectroscopy. For both amorphous silicates and crystalline zeolite BEA, the apparent activation enthalpies ($\Delta H^{\ddagger}$) for alkene epoxidation and H_2O_2 decomposition correlate linearly with the LMCT energies of reactive intermediates and also with the enthalpies of adsorption for gaseous basic probe molecules (e.g., pyridine or deuterated acetonitrile) onto the Lewis acidic active sites.[10, 23] Kholdeeva et al. examined cyclooctene epoxidation on Ti- and Nb-silicates[14, 34] and Carbo and coworkers studied reactions of H_2O_2 and cyclohexene over Ti- and Nb-atoms grafted to tungsten-based Lindqvist polyoxometallates (POM).[38, 39] These reports

proposed that both Ti and Nb active sites epoxidize alkenes via metal-hydroperoxo (M-OOH) reactive intermediates, and Nb catalysts provide lower apparent activation energies for epoxidations than the corresponding Ti-based catalysts. These differences were concluded to reflect the greater electrophilicity of the Nb active sites.[14, 38, 39] Overall, the strong correlation of these kinetic and thermodynamic quantities suggests that active sites with greater electron affinities (i.e., stronger Lewis acid character) provide lower $\Delta H^{\ddagger}$ and also greater rates and selectivities for alkene epoxidations among series of otherwise similar metal – silicate catalysts.

We hypothesized these trends would extend to catalytically relevant group 6 metals (e.g., Mo and W), which due to their relatively high Pauling electronegativities (2.16 and 2.36 for Mo and W compared to 1.54 and 1.6 for Ti and Nb, respectively)[41], may explain the previous reports of high rates on W- and Mo-based molecular catalysts. For example, Sheldon reports higher redox potentials and Lewis acidity of soluble transition metal complexes lead to increasing reactivity for epoxidation with organic hydroperoxides and ranks the reactivity of molecular metal complexes in order of decreasing rates: Mo > W > Ti, V.[42, 43] Propylene epoxidation processes employ solid Ti-silicates (e.g., Shell Styrene Monomer Propylene Oxide process with ethylbenzene hydroperoxide, Dow Hydrogen Peroxide-Propylene Oxide process) in addition to soluble Mo-complexes (e.g., Halcon process with tert-butyl hydroperoxide).[15, 44, 45] Extensive studies of molecular Mo and W catalysts suggest that reaction with H_2O_2 forms homogeneous Mimoun complexes (i.e., stable metal centers possessing both metal-oxo and metal-peroxo functions), which transfer oxygen atoms from peroxo groups to alkenes during epoxidations.[16, 46-49] In comparison, only a few studies have examined heterogeneous group 6 metal catalysts for epoxidations.[50-56] For example, Hammond et al. reported that bulk WO_3 species are the more active form of supported W catalysts for cyclooctene epoxidation.[56] The absence of comparisons between

supported groups 4-6 early transition metal catalysts stems, in part, from the instability of Mo and W on amorphous solid supports, which allows these metals to leach into solution or polymerize on surfaces.[57, 58] In addition, most investigations of supported group 6 metals use organic hydroperoxides as oxidants and fewer examine catalysis with H_2O_2.[43, 59, 60]

Here, we synthesize groups 4-6 metal atom (Ti, Nb, Mo, and W) substituted zeolite BEA materials with the intent to create a homologous series of catalysts that possess isolated metal active sites within pores of identical topology and polarity. We combine kinetic, spectroscopic, and calorimetric methods to determine how the identity of the reactive intermediates, the reaction pathways, and relevant kinetic barriers for the epoxidation of alkenes with H_2O_2 depend on differences in the identity of the framework-substituted transition metal atoms. UV-Vis and Raman spectroscopy together with *in situ* titrations of active sites with phosphonic acids demonstrate that selected W-, Ti-, and Nb-BEA materials predominantly stabilize monomeric active sites present at tetrahedral sites likely within the BEA framework. However, Mo leaches rapidly from the framework that the stable M-BEA (M = Ti, Nb, W) catalysts mediate epoxidations by equivalent series of elementary steps that are described with a single rate expression. Analysis of the products of cis-stilbene epoxidation and of *in situ* Raman and UV-Vis spectra give evidence that Ti-OOH, Nb-(η^2-O_2), and W-(η^2-O_2) are the reactive intermediates for epoxidation on each of the respective metal atoms. Turnover rates and selectivities for 1-hexene epoxidation are lower for W-BEA despite expectations that W's greater Pauling electronegativity would give rise to much higher rates. Consistent with these differences, $\Delta H^{\ddagger}$ for epoxidation on W-BEA exceeds those for Ti- and Nb-BEA by more than 30 kJ mol^{-1} at equivalent coverages of reactive intermediates. Despite these deviations from expectations, the differences among $\Delta H^{\ddagger}$ values correlate with enthalpies for liquid-phase adsorption of 1,2-epoxyhexane, as measured by isothermal titration calorimetry

(ITC). These comparisons confirm that group 4-6 active metal sites in the BEA framework follow classical linear free energy relationships and show that comparisons of electronegativities of individual elements do not provide accurate predictions for the electronic properties of active sites in these zeolite catalysts. These distinctions likely reflect variations in framework coordination and pendant functions (e.g., hydroxyl, oxo groups) among these active sites.

2.2 Materials and Methods

2.2.1 Catalyst Synthesis

M-BEA catalysts, where M refers to the identity of the metal incorporated into the zeolite (M = Ti, Nb, Mo, W), were synthesized by post-synthetic modification of commercial Al-BEA samples. Al-BEA (TOSOH, lot No. 94HA6X02Y; Si:Al = 20) was refluxed in HNO_3 (Macron Chemicals, 68-70 wt%; *Caution: HNO_3 can cause severe chemical burns and should be handled with care*) to remove Al atoms from the BEA framework, likely by forming soluble $Al(NO_3)$ species that traverse pores and enter the bulk liquid. The dealuminated BEA was recovered by vacuum filtration and washed with H_2O (17.5 MΩ cm, 60 $cm^3\ g^{-1}$). These samples were then heated to 823 K (4 K min^{-1}) in flowing dry air (100 $cm^3\ min^{-1}$; Airgas, Ultra Zero Grade) and held at 823 K for 6 h to desorb or oxidize residues (e.g., water, organics) remaining after the synthesis and dealumination processes. Subsequent characterizations by energy dispersive X-ray fluorescence (EDXRF) and X-ray diffraction (XRD) show that these treatments remove nearly all Al, leaving only trace quantities (Si:Al > 2400), but leave the crystalline BEA framework intact.

Transition metal atoms were incorporated into tetrahedral vacancies in the BEA framework by adsorption of metal chlorides within appropriate polar solvents, using a methodology similar to our prior reports for Ti-, Nb-, and Ta-BEA catalysts.[10, 23] The dealuminated BEA (Si-BEA) was

loaded into a round bottom flask heated under vacuum (< 5 Pa, 473 K) for 2 h to remove free water molecules. The moisture-free solids are suspended in solvent (dichloromethane (Fisher Chemicals, 20 cm^3 $g_{zeolite}^{-1}$) for Ti-BEA and Mo-BEA, isopropyl alcohol (Fisher Chemicals, 20 cm^3 $g_{zeolite}^{-1}$) for Nb-BEA, and chloroform (Fisher Chemicals, 20 cm^3 $g_{zeolite}^{-1}$) for W-BEA. Schlenk methods are used to introduce $TiCl_4$ (Sigma Aldrich, ≥99.0%), $MoCl_5$ (Sigma Aldrich, 99.99% trace metals basis (excluding W)), $NbCl_5$ (Sigma Aldrich, 99%), or WCl_6 (Sigma Aldrich, ≥99.9% trace metals basis) to the mixture of solvent and Si-BEA. The resulting mixture is heated to reflux under flowing Ar (Airgas, Ultra zero grade) and stirred (350 rotations per minute (rpm)) for 8 h with the intent to dissociatively bind the metal chloride at silanol nests ($(SiOH)_4$) generated by the dealumination treatment. The solutions of metal chlorides and Si-BEA are initially colored distinctly ($TiCl_4$ is white; $MoCl_5$ is orange; WCl_6 is dark green; and $NbCl_5$ is colorless), however, the solutions all became white and opaque after ~8 h as a result of the reactive adsorption of the metal complexes to the Si-BEA support. The solids were recovered by rotary evaporation (IKA, RV 10) and were heated at 5 K min^{-1} in flowing dry air (100 cm^3 min^{-1}) and held at 823 K for 6 h. Following this oxidative treatment, the M-BEA samples appear as white powders.

2.2.2 Catalyst Characterization

The elemental compositions of the M-BEA samples were determined by EDXRF. Finely ground samples of M-BEA (~ 50 mg) were placed in a 1 cm-diameter sample holder, sealed with an ultralene film, and loaded into the He-purged chamber of the spectrometer (Shimadzu, EDX-7000). The sample was scanned between 0 and 30 keV and the elemental composition of the sample was calculated using the relative intensities of the corresponding fluorescence peaks.

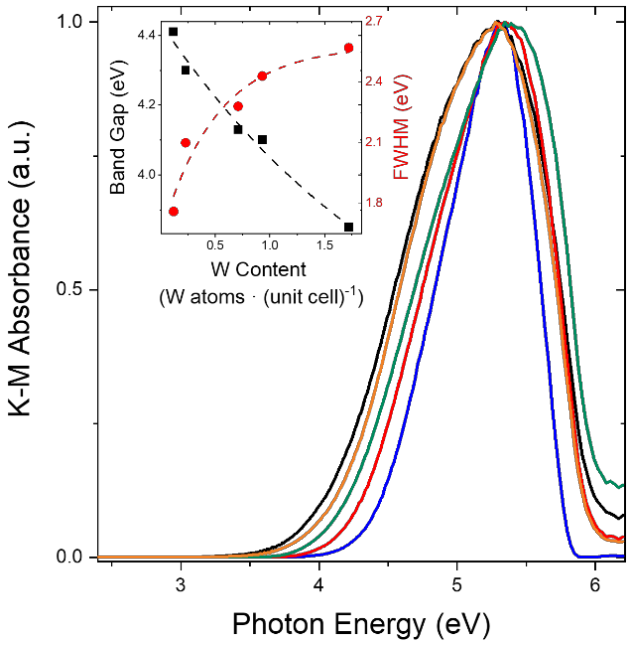

Figure 2.1. Tauc plots of W-BEA (0.12 (blue line —), 0.23 (red line —), 0.71 (green line —), 0.93 (orange line —), and 1.72 (black line —) W atoms per unit cell) derived from DRUV-Vis spectra under ambient conditions were used to plot (inset) band gap and FWHM of DRUV-Vis absorbance feature as functions of the tungsten content (W atoms (unit cell)$^{-1}$).

The dispersities of the Ti, Nb, Mo, and W atoms present on the M-BEA materials were examined with diffuse reflectance UV-Vis (DRUV-vis) spectroscopy to measure metal band gap energies using a UV-vis spectrophotometer (Varian Cary 5G). M-BEA samples were intimately mixed and ground with magnesium oxide (MgO; Sigma Aldrich, 99.995 %) at a MgO to M-BEA mass ratio of 10:1, and pure MgO was used to obtain background spectra. Band gap energies were determined by extrapolating the linear portion of the Tauc plots to the horizontal axis representing photon energy (eV) (Figure A1). Figure 2.1 shows Tauc plots (i.e., Kubelka-Munk (K-M) absorbances as a function of photon energy) for W-BEA samples with W contents ranging from 0.12 to 1.7 W atoms per unit cell (0.55 – 7.8 wt%). These samples possess band gaps that decrease systematically (3.85 – 4.41 eV) with increasing metal content and that are greater than the band gap for bulk WO_3 (2.8 eV),[61] which indicates that the W atoms in these samples are relatively

disperse. Both the band gap energies and the widths of the absorbance features change asymptotically with decreasing W atom loading (Figure 2.1 inset) suggesting that the distribution of W complexes becomes increasingly uniform and contains greater fractions of monomeric species.[62] We therefore maximize the fraction of isolated W atoms by use of low metal loadings during post-synthetic modification.[63, 64] We have previously reported synthesis and characterization of comparable Ti- and Nb-BEA materials.[10, 23, 65]

The crystallinities of the M-BEA samples were determined using an X-ray diffractometer (Siemens-Bruker, D5000) with Cu Kα radiation under ambient conditions. The diffractograms obtained (Figure A2) match reported powder diffraction patterns for zeolite BEA without observable changes in peak positions for the specific metal contents reported in Table 2.1. Higher metal loadings (> 0.95 atoms (unit cell)$^{-1}$) of Ti, Nb, and Ta, however, shift diffraction features to lower angles due to a slight expansion of the unit cell.[65] W loadings greater than 1.7 atoms (unit cell)$^{-1}$ show a similar change. These results show all M-BEA retain the BEA framework structure after dealumination and metal incorporation.

Table 2.1 displays the metal content of the M-BEA samples used for catalytic rate measurements, *in situ* UV-vis experiments, and isothermal titration calorimetry. These samples contain low transition metal contents (<0.25 atoms (unit cell)$^{-1}$, on average) in order to form monomeric species within the BEA framework, avoid internal mass transfer constraints,[66] and present active sites in intrapore environments with similar silanol densities.[19] M-BEA samples with greater densities of transition metal atoms were used for *ex situ* characterization and for *in situ* Raman experiments in order to examine changes in physical properties with metal content and to identify spectroscopic features related to monomeric and oligomeric species.

Table 2.1. Metal Loading, Metal Atoms per Unit Cell, Band Gap, and Percentage of Active Metal for M-BEA Samples Used in Catalytic Measurements

Catalyst	Metal loading (wt %)[a]	Metal atoms per unit cell	Band gap (eV)[b]	Bulk metal oxide band gap (eV)	Active metal (%)[c]
Ti-BEA	0.25	0.20	4.34	3.2	100 ± 4
Nb-BEA	0.22	0.09	4.73	3.4	100 ± 6
W-BEA	1.1	0.23	4.30	2.8	70 ± 5
Mo-BEA	0.4	0.16	3.96	2.9	n.d.[d]

[a]measured by EDXRF (Section 2.2.2), [b]determined by DRUV-vis (Section 2.2.2, Figure A1), [c]calculated from *in situ* tert-butyl phosphonic acid titrations (Section 2.3.2, Figure A8), [d]not determined; leaching of Mo from BEA framework during catalysis precluded attempts to titrate number of active sites.

2.2.3 Epoxidation and H_2O_2 Decomposition Turnover Rate Measurements

Turnover rates for 1-hexene (C_6H_{12}) epoxidation with H_2O_2 on M-BEA were measured in liquid CH_3CN, at low temperatures (303-333 K), and in stirred batch reactors (700 rpm) at differential conversion (< 0.5 %). These conditions avoid internal mass transfer constraints at turnover rates, particle sizes, and site densities used in this study, as we have shown using the Madon-Boudart criterion.[10, 23] The alkene substrate, decane (an internal standard), and H_2O_2 were stirred in CH_3CN at 313 K, and an initial aliquot (~0.5 cm^3) was taken after 30 min. After the addition of ~10-50 mg of catalyst, aliquots were taken at regular intervals using a syringe equipped with a polypropylene filter (Tisch Scientific, 0.05 μm) to separate the catalyst particles from the sample and halt the reaction. Products were analyzed with a gas chromatograph (Agilent, 6850) equipped with a flame ionization detector and liquid autosampler (CTC Analytics, GC Pal).

Comparisons between replicated rate measurements indicate that the experimental uncertainty of these measurements is ~10%.

Hot filtration tests were used to determine if metal atoms leach from the BEA zeolite and form soluble complexes active for epoxidation. During a batch reaction, an aliquot of the mixture (~10 ml) was taken at 10 min, filtered (0.05 μm), and transferred into a stirred and heated 20 cm^3 scintillation vial (700 rpm, 313 K). Subsequently, aliquots were taken from the scintillation vial as a function of time and the concentrations of all species were determined by gas chromatography. Hot filtered solutions taken from reactions with Ti-BEA, Nb-BEA, and W-BEA did not show any change in epoxide concentration following filtrations. Hot filtered solutions taken from reactions with Mo-BEA did, however, show measurable increases in the concentration of epoxide, which indicates this sample produces soluble metal complexes active for epoxidation.

Hydrogen peroxide decomposition rates were measured using colorimetric titration with an aqueous titrant solution of $CuSO_4(H_2O)_5$ (8.3 mM; VWR, 99%) and neocuproine hydrate (12 mM; SAGECHEM) in an aqueous solution of ethanol (4.3 M; Decon Laboratories, 100%). The reaction solution (0.15 cm^3) was titrated with a combination of titrant (1 cm^3) and DI H_2O (0.85 cm^3), and the absorbance at 454 nm was determined using a UV-Vis spectrophotometer (Spectronic, 20 Genesys). The corresponding H_2O_2 concentration values were used to calculate H_2O_2 decomposition rates by subtracting the formation rate of 1,2-epoxyhexane from the total rate of H_2O_2 consumption.

Catalytically active sites were titrated *in situ* with phosphonic acids (PA) to determine the fraction of metal atoms that contribute to measured epoxidation rates.[23, 67] Tert-butyl phosphonic acid (TBPA; Sigma Aldrich, 98%) or methyl phosphonic acid (MPA; Sigma Aldrich, 98%), 1-

hexene, decane, and the catalyst were combined with CH_3CN in the reaction flask and stirred for 30 min (700 rpm, 313 K) to allow the PA to bind to M atoms. H_2O_2 was then added to initiate the reaction and aliquots were taken and analyzed as before. These experiments were conducted for multiple ratios of [PA] to [M] with values ranging from 0 to 2 to determine how apparent turnover rates decrease as a function of the amount of titrant. The number of catalytically active sites within each sample was calculated by a linear fit of the titration results at the lowest coverages and with the assumption that each PA molecule binds to one metal center. Analysis of these results (Section 2.3.2) shows that *in situ* titrations with TBPA provide a more accurate estimate for site counts than titrations with MPA (see below). Consequently, the percentage of active metal atoms in Table 2.1 are determined from titrations with TBPA.

2.2.4 *In Situ* Raman and UV-Vis Spectroscopy

In situ Raman and UV-Vis spectra of species formed by the activation of H_2O_2 on M-BEA samples were obtained by placing catalyst pellets (30-50 mg) in a custom-built liquid flow cell. Steady-state spectra of the H_2O_2-derived surface species were collected in a solution of H_2O_2 (10 mM H_2O_2, 39 mM H_2O, 313 K) in flowing CH_3CN, introduced at 1 cm^3 min^{-1} by an HPLC pump (SSI, LS Class).

H_2O_2 activation on M-BEA was observed using a Raman spectrometer (Renishaw, InVia) equipped with a 442 nm laser that delivered a power density of 0.8 mW μm^{-2} at the sample, as measured directly by a power meter (Gentec-EO, PRONTO-Sl). Reported spectra were obtained with a long 50X objective and represent the average of 100 scans (10 scans s^{-1}) at an estimated resolution of 2 cm^{-1}. In order to increase Raman peak intensity and clearly observe features unique to H_2O_2 activation, we used M-BEA synthesized with high metal content (1.2 wt % Ti, 3 wt % Nb,

5 wt % W, 5 wt % Mo). Intermediates formed upon *in situ* H_2O_2 activation were also examined using a fiber-optic UV-Vis spectrometer (Avantes, AvaFast 2048). Absorbance features were deconvoluted by performing baseline subtraction and Gaussian peak fittings using OriginPro software.

2.2.5 Isothermal Titration Calorimetry on M-BEA Catalysts

Enthalpies for adsorption of 1,2-epoxyhexane onto M-BEA catalysts were determined using an isothermal titration calorimeter (TA Instruments, NanoITC) equipped with both reference and sample cells. A solution of 1,2-epoxyhexane (10 mM $C_6H_{12}O$; Sigma Aldrich, 97%) in CH_3CN (39 mM H_2O) was used to titrate a slurry of ~20-30 mg of M-BEA in CH_3CN (39 mM H_2O, 313 K, 250 rpm). Values of 1,2-epoxyhexane adsorption enthalpies were determined by averaging heats released upon titration of M-BEA at substoichiometric (< 0.2) quantities of 1,2-epoxyhexane relative to metal sites in M-BEA with the assumption that all titrant molecules adsorb to M atoms.

2.3 Results and Discussion

2.3.1 Reactive Species Formed Upon H_2O_2 Activation

Early transition metal atoms (Ti, Nb, W, and Mo) substituted in BEA activate H_2O_2 to form pools of surface intermediates, including metal peroxide (M-(η^2-O_2))[47], metal hydroperoxide (M-OOH)[10, 23], and metal oxo (M=O)[68] species that have been implicated in liquid-phase oxidation reactions. Here, we combine *in situ* Raman and UV-vis spectroscopies with analysis of product distributions from cis-stilbene epoxidation to determine the identities of reactive species that directly transfer oxygen atoms to alkenes during epoxidation. Figure 2.2 shows steady-state Raman spectra of Si-, Ti-, Nb-, W-, and Mo-BEA within flowing solutions of H_2O_2 (10 mM H_2O_2, 39 mM

H_2O, in CH_3CN, 313 K). All spectra are normalized to vibration of the BEA zeolite framework at 312 cm^{-1} [69] to facilitate comparisons among materials, and spectra include large features associated with the CH_3CN solvent at 375 cm^{-1} and 920 cm^{-1}.[70] In addition, all spectra of M-BEA samples contain features at 694 cm^{-1} and from 750 – 825 cm^{-1}, which correspond to framework vibrations of zeolite BEA[71] and appear in *ex situ* spectra (Figure A3).

The Raman spectra of H_2O_2-activated Ti-, Nb-, Mo-, and W-BEA contain features between 550 – 620 cm^{-1} that correspond to the symmetric and asymmetric stretching modes of metal-peroxo (M-(η^2-O_2)) intermediates.[72-75] The position of ν(M-(η^2-O_2)) shifts to lower wavenumbers from Ti-BEA[72] to Nb-BEA, Mo-BEA, and W-BEA[73] due to greater charge transfer from the group 6 metal center to the peroxide moiety.[76] In addition to features that appear only after contact with H_2O_2, spectra for Mo- and W-BEA possess a distinct feature near 970 cm^{-1} (Figure 2.2), which is attributed to ν(M=O)[61, 77] and is absent from spectra of Ti-BEA and Nb-BEA. Mo-BEA and W-BEA also show Raman features reminiscent of oligomeric metal oxides complexes including bridging M-O-M bonds at 700 cm^{-1} [61] and 805 cm^{-1} for WO_3 and 880 cm^{-1} for MoO_3.[61, 77, 78] The vibrational features (700 cm^{-1} and 805 cm^{-1}) that correspond to bulk WO_3 increase monotonically with W content (Figure A3), which shows that extra-framework WO_x oligomers form at higher loadings.[79] Similarly, greater loadings tend to form oligomeric MoO_x on Mo-BEA. Collectively, these Raman spectra show that all Ti-, Nb-, W-, and Mo-BEA activate H_2O_2 to form M-(η^2-O_2) species, while W- and Mo-BEA materials also possess distinguishable M=O functions.

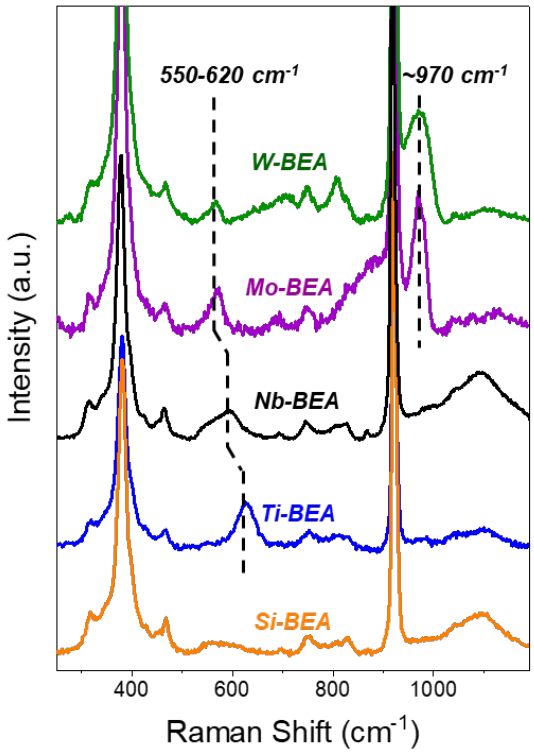

Figure 2.2. *In situ* Raman spectra (442 nm laser, 0.8 mW·μm^{-2}) in flowing CH_3CN (10 mM H_2O_2, 39 mM H_2O, 313 K, 1 cm^3 min^{-1}). Spectra are offset and normalized to a feature of the BEA framework at 312 cm^{-1}. The spectrum for Mo-BEA is obtained ~100 s after contact with the H_2O_2 solution, and all others are taken at steady-state.

Figure 2.3 shows steady-state UV-vis spectra of Ti-, Nb-, and W-BEA collected *in situ* after H_2O_2 activation (10 mM H_2O_2, 39 mM H_2O in CH_3CN, 313 K). These spectra contain broad asymmetric features between 250 – 500 nm, which agree with reports for the ligand-to-metal charge transfer (LMCT) peaks of M-(η^2-O_2) and M-OOH species on metal atoms grafted to mesoporous SiO_2,[23, 34, 80] incorporated into the framework of zeolite BEA,[10] and for homogeneous complexes.[81] These interpretations agree with earlier studies that assigned the UV-Vis absorbance features to the changing coordination state of Ti atoms incorporated into zeolite framework[82, 83] and more recent evidence from Tilley et al.[80, 84] and Ivanchikova and coworkers[34] that indicates

the observed UV features for H_2O_2-activated transition metal centers on silica reflect the presence of both metal hydroperoxo and metal peroxo species. These UV-vis spectra (Fig. 3) consist of two overlapping LMCT peaks, where the higher energy (lower wavelength) feature corresponds to M-(η^2-O_2) intermediates and the lower energy feature signifies M-OOH species. These features were confirmed over Ti-BEA, Nb-BEA, and Ta-BEA materials by correlating reversible changes in the relative intensities of the M-OOH and M-(η^2-O_2) features to concentration of protons in aqueous solutions.[23]

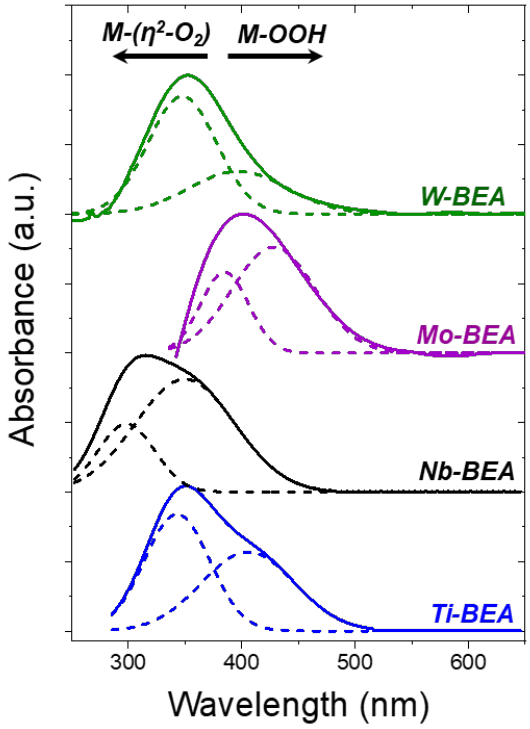

Figure 2.3. Difference UV-Vis spectra of H_2O_2 activated Ti-BEA (blue line —), Nb-BEA (black line —), Mo-BEA (purple line —), and W-BEA (green line —) acquired *in situ* within flowing CH_3CN (10 mM H_2O_2, 39 mM H_2O, 313 K, 1 cm^3 min^{-1}). Spectra are offset and normalized by the maximum absorbance value. The background spectrum for each M-BEA was obtained in CH_3CN (39 mM H_2O, 313 K) before contact with H_2O_2.

In situ Raman and UV-Vis spectra along with post-reaction EDXRF show that Ti-, Nb-, and W-BEA are stable and show little to no metal dissolution during catalysis (≤ 7% for W-BEA, immeasurable changes for Ti- and Nb-BEA after 2 h in CH_3CN (10 mM H_2O_2, 39 mM H_2O, 313 K, 700 rpm)); however, molybdenum atoms leach rapidly from the BEA framework following contact with H_2O_2. Time-resolved Raman (Fig. S4) and UV-vis spectra (Fig. S6) collected *in situ* show that vibrational features and LMCT bands specific to Mo-containing complexes completely attenuate after 0.5 -2.5 h of contact with H_2O_2 in CH_3CN (10 mM H_2O_2, 39 mM H_2O, 313 K), and EDXRF indicates at least 90% loss of Mo from BEA. Consequently, further comparisons among M-BEA catalysts omit Mo-BEA.

Scheme 2.1 displays plausible structures for reactive M-OOH and M-(η^2-O_2) intermediates detected by *in situ* Raman (Figure 2.2) and UV-Vis spectra (Figure 2.3) of M-BEA catalysts in contact with H_2O_2. Titanium and niobium ions substituted into zeolites commonly acquire four framework bonds (e.g., as $Ti(OSi)_4$[85] or $Nb(OSi)_4OH$[86]) and activate H_2O_2 to form M-OOH and M-(η^2-O_2) species.[86, 87] The coordination of metal hydroperoxo species (M-(η^2-OOH) or M-(η^1-OOH)) for metal silicates remains under debate.[14, 80] Detailed characterization of Mo[88-90] and W[62, 91, 92] atoms grafted to silica surfaces by X-ray absorption spectroscopy, infrared spectroscopy, and ^{29}Si nuclear magnetic resonance suggest these atoms may adopt bipodal surface coordination with M=O ligands under hydrated and dehydrated conditions. Density functional theory predicts that the predominant coordination structure of group 6 metal atoms at framework position in BEA possesses two framework bonds with remaining coordination to metal-dioxo ligands (i.e., $M(OSi)_2O_2$) in the presence of water, however the precise coordination structure has not yet been confirmed experimentally.[93] With these expectations, we tentatively interpret the Raman spectra in Figure 2.2 to suggest that $W(OSi)_2O_2$ moieties activate H_2O_2 to form W-(η^2-O_2) and W-OOH

species that bind together with oxo ligands (e.g., as $W(OSi)_2(\eta^2\text{-}O_2)O$), as depicted in Scheme 2.1. We depict the coordination of the W-atom based upon recent reports for W on silica surfaces,[94] although other coordination structures with three or four linkages to the BEA framework may exist.

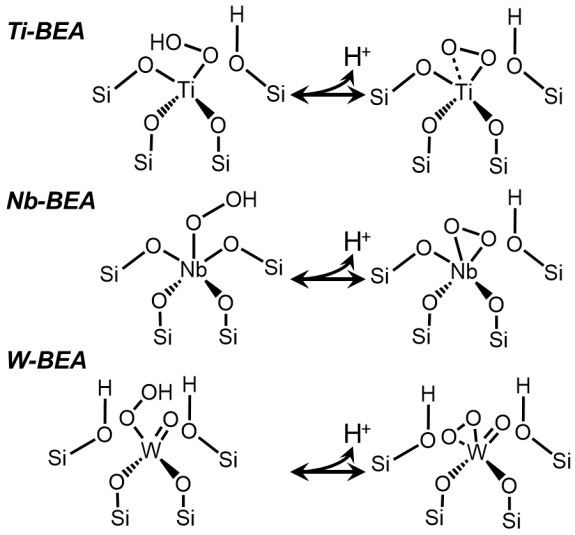

Scheme 2.1. Proposed structure of H_2O_2-derived intermediates on groups 4-6 metals in zeolite BEA. Solvent molecules have been omitted for clarity.

Prior literature establishes that one complex within these pools of reactive intermediates on a given metal center dominates rates for oxygen transfer to alkenes within epoxidation reactions.[10, 95] The most significant reactive intermediate for epoxidation on Ti and Nb atoms substituted into BEA[10, 23] or supported on amorphous silica[23] are Ti-OOH and Nb-(η^2-O_2), respectively. While there are fewer studies for heterogeneous W materials,[96, 97] catalytic investigations of molecular complexes of group 6 metals suggest W-(η^2-O_2) is the reactive intermediate for epoxidations.[16, 46, 47] *In situ* Raman spectra show no observable changes in the feature corresponding to W=O complexes (970 cm^{-1}) when 1-hexene contacts W-BEA in the absence of H_2O_2 and no detectable amounts of 1,2-epoxyhexane form over 1 h at 313 K. Therefore, the oxo functions do not transfer O-atoms to

alkenes at conditions used in this investigation. Consequently, M-OOH and M-(η^2-O_2) are the remaining plausible reactive intermediates for epoxidation over W-BEA.

Table 2.2. Products of Cis-Stilbene Epoxidation with H_2O_2, Reactive Oxygen Species, and Corresponding LMCT Energies

Catalyst	Ratio of cis- to trans-stilbene oxide[a]	Reactive intermediate for epoxidation[b]	LMCT energy of reactive intermediate (eV)[c]
Ti-BEA	2.6 ± 0.1	Ti-OOH	3.1
Nb-BEA	0.9 ± 0.1	Nb-(η^2-O_2)	4.2
W-BEA	0.7 ± 0.1	W-(η^2-O_2)	3.6
Mo-BEA	n.d.[d]	Mo-(η^2-O_2)[e]	3.2

[a]ratio of turnover rates for cis-stilbene epoxide and trans-stilbene epoxide measured with 20 mM cis-stilbene, 10 mM H_2O_2, 39 mM H_2O in CH_3CN at 313 K; [b]determined from the ratio of cis- to trans-stilbene oxide; [c]determined by deconvolution of UV-Vis spectra measured *in situ* in CH_3CN (10 mM H_2O_2, 39 mM H_2O, 313 K, 1 ml min^{-1}) over M-BEA; [d]not determined; leaching of Mo from BEA framework during catalysis precluded attempts to measure cis-stilbene epoxidation rates; [e]an extension of results for W-BEA and prior studies for Mo-complexes (Mo-(η^2-O_2))[47]

Analysis of the distribution of isomers formed during the epoxidation of cis-stilbene with H_2O_2 over W-BEA (and Ti- and Nb-BEA) catalysts provide evidence for the identity of the surface intermediate responsible for epoxidation on each material. Epoxidation reactions with M-OOH and M=O species both occur through a concerted oxidation mechanism that inhibits stereochemical rearrangement[98, 99] and forms cis-stilbene epoxide as the dominant product. In contrast, M-(η^2-O_2) functions react with alkenes through a stepwise mechanism that involves the formation of a radical M-OO• moiety and sequential formation of C-O bonds, which allows for C-C bond rotation and isomerization.[15, 100, 101] Consequently, reactions with M-(η^2-O_2) moieties yield

comparable concentrations of cis- and trans-stilbene oxide. Table 2.2 shows the distributions of product isomers from cis-stilbene epoxidation with H_2O_2 over each M-BEA, which were determined by measured concentration profiles as functions of time (Figure A7). Ti-BEA forms primarily cis-stilbene oxide, whereas Nb-BEA and W-BEA form similar quantities of cis- and trans-stilbene oxides. These results indicate that Ti-BEA reacts through Ti-OOH, and Nb-BEA and W-BEA react through Nb-(η^2-O_2) and W-(η^2-O_2) species, respectively.

The electronic properties of reactive M-OOH and M-(η^2-O_2) species affect the activation barriers for O-atom transfer during epoxidations. Table 2.2 lists the LMCT energies for the reactive M-OOH and M-(η^2-O_2) intermediates on Ti-, Nb-, and W-BEA observed in Figure 2.3, which decrease in the order Nb-(η^2-O_2), W-(η^2-O_2), and Ti-OOH. Lower LMCT energies correspond to more electrophilic reactive intermediates on groups 4-5 M-BEA. Active species on Ti-BEA absorb at lower energy wavelengths than those on Nb-BEA, which indicates a greater energy barrier to transfer charge to metal from the ligand, and therefore, the oxygen intermediates on Ti-BEA are more electrophilic than those on Nb-BEA. We reported previously that apparent activation enthalpies for cyclohexene epoxidation decrease linearly with the LMCT band for the reactive intermediate over groups 4-5 M-BEA.[10] Table 2.2 shows that the energies for LMCT from H_2O_2-derived species active for epoxidation on Ti-BEA and Nb-BEA lie at 3.1 eV (Ti-OOH) and 4.2 eV (Nb-(η^2-O_2)), respectively. In comparison, the LMCT energy for W-(η^2-O_2), the reactive species for W-BEA, falls between those for Nb-BEA and Ti-BEA at 3.6 eV, while Mo-BEA absorbs at energies similar to Ti-BEA. The values of these LMCT energies (Table 2.2) and the periodic trends for groups 4 and 5 metals led us to anticipate that epoxidation rates for W-BEA would fall between those for Ti-BEA and Nb-BEA (Ti-OOH > W-(η^2-O_2) > Nb-(η^2-O_2)) and that these differences

would be reflected in apparent activation enthalpies for epoxidation. These expectations prove to be incorrect (*vide infra*).

2.3.2 *In Situ* Titrations of Active Sites

Equitable comparisons of turnover rates among M-BEA catalysts require accurate measurements for the density of catalytically active metal atoms within each material. Prior reports hypothesize that alkyl phosphonic acids deprotonate, and the conjugate bases bind strongly to Lewis acidic transition metal atoms grafted onto silica and inhibit catalytic turnovers.[31, 67] The manner by which these titrants reduce reaction rates are not clear: phosphonic acids may inhibit the activation of H_2O_2 or make reactive M-OOH and M-(η^2-O_2) species inaccessible to the alkene. Figure 2.4 shows that epoxidation rates normalized by the total number of Ti atoms on Ti-BEA decrease as the ratio of methylphosphonic acid (MPA) or tert-butylphosphonic acid (TBPA) to Ti increases within the reaction mixtures. While 1-hexene epoxidation rates decrease modestly with the addition of MPA (e.g., ~20% at equimolar quantities), cyclohexene epoxidation rates decrease linearly at lower ratios of MPA to Ti (Figure 2.4a) but retain a significant fraction of their initial value as the MPA to Ti ratio approaches unity. In comparison, TBPA inhibits epoxidation kinetics significantly for both 1-hexene and cyclohexene (Figure 2.4b). These comparisons suggest that neither MPA nor TBPA prevent the formation of H_2O_2-derived reactive intermediates. Rather, TBPA competitively binds to the active metal sterically inhibiting 1-hexene from accessing the reactive intermediate, Ti-OOH. This interpretation is supported by the differences between *in situ* UV-vis spectra of Ti-BEA with and without addition of TBPA (Figure 2.4c). Contact with a H_2O_2 solution (10 mM H_2O_2, 39 mM H_2O, CH_3CN, 313 K) produces similar absorbance features on Ti-BEA samples in the presence and absence of TBPA, which demonstrates that significant coverages

of Ti-(η^2-O_2) and Ti-OOH intermediates (Section 2.3.1) form in both situations. The subsequent introduction of 1-hexene (0.1 M C_6H_{12}, 313 K, 60 min) leads to a significant decrease (30%) in the intensity of the LMCT feature in the absence of TBPA. However, contact with the same reactant solution causes a minimal attenuation of the absorbance feature (< 10%) when TBPA binds to the Ti site. These observations indicate that phosphonic acid titrants inhibit epoxidation reactions because the bound complex sterically hinders the reaction between active M-(η^2-O_2) and M-OOH intermediates and alkene co-reagents but do not prevent the activation of H_2O_2.

Extrapolation of the initial linear regime of TBPA titration plots to the horizontal axis (Figure A8) provides estimates for the percentage of metal atoms that produce active sites in each M-BEA sample. These results of TBPA titrations indicate that nearly all Ti and Nb atoms within the BEA framework form active sites for 1-hexene epoxidation (Table 2.1), however, the portion of catalytically active W atoms is lower (70 ± 5 %). The percentage of inactive W atoms increases with the mass loading of W on the dealuminated BEA zeolite (Figure A9), which correlates with a decrease in the band gap of these W-BEA samples from 4.41 eV to 4.10 eV (Table A2). Figure 2.5 shows that rates for 1-hexene epoxidation normalized by the total number of W atoms (determined by EDXRF) decrease monotonically as the W content increases. However, turnover rates determined by normalizing rates by the number of active sites from TBPA titrations do not change across this range of W loadings (0.1 – 1 W atoms (unit cell)$^{-1}$), which suggests that oligomerization reduces the fraction of W atoms accessible to reactants. Consequently, we can accurately compare rates among M-BEA when we normalize to the amount of active metal measured by TBPA titrations. Moving forward, we report turnover rates by normalizing measured rates by the number of active sites within each M-BEA, as determined by TBPA titrations (Figure A8, Table 2.1).

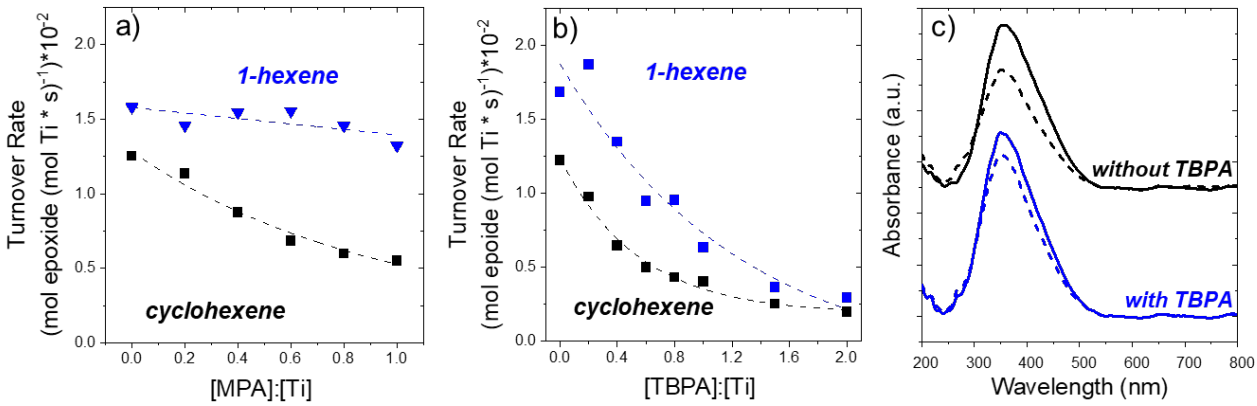

Figure 2.4. Turnover rates for cyclohexene and 1-hexene epoxidation with H_2O_2 over Ti-BEA as a function of (a) methyl phosphonic acid (MPA) to incorporated Ti ratio, and (b) tert-butylphosphonic acid (TBPA) to incorporated Ti ratio. (c) UV-Vis spectra of Ti-BEA collected *in situ* first in CH_3CN (10 mM H_2O_2, solid), then in CH_3CN (0.1 mM C_6H_{12}, dashed) with (blue) and without (black) addition of TBPA prior to contact with the H_2O_2 solution.

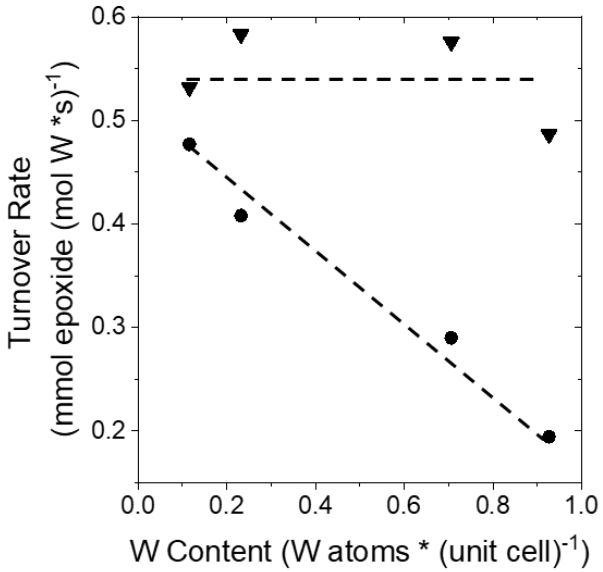

Figure 2.5. Rates for 1-hexene epoxidation in CH_3CN (10 mM C_6H_{12}, 1 mM H_2O_2, 3.9 mM H_2O, 313 K) normalized by the total number of W atoms (circle, solid ●) and by the number of active W atoms determined by TBPA site titrations (triangle, solid ▼) as functions of the tungsten content (W atoms (unit cell)$^{-1}$).

2.3.3 Mechanistic Interpretation of Epoxidation Kinetics

Turnover rates for alkene epoxidation over Ti-BEA, Nb-BEA, and W-BEA depend on the concentration of the alkene, the oxidant, and the reaction products, because the presence and concentration of these species determine the coverage of surface intermediates formed throughout the catalytic cycle. Scheme 2.2 depicts a catalytic cycle for epoxidation and H_2O_2 decomposition over group 4 metals, which can be extended to groups 5 and 6 and agrees with reported findings for cyclohexene,[10] 1-octene,[19] and styrene[23] epoxidation with H_2O_2 over Ti-, Nb-, and Ta-BEA catalysts and also with 1-octene epoxidation with tert-butyl hydroperoxide (TBHP) and cumene hydroperoxide (CHP) on Ti-BEA and Ti-SBA15.[102] This series of elementary steps involves the quasi-equilibrated adsorption of C_6H_{12} (step 1) and H_2O_2 (step 2). Adsorbed H_2O_2 activates irreversibly (step 3) to form reactive M-OOH and M-(η^2-O_2). Subsequently, these intermediates transfer oxygen to C_6H_{12} in the kinetically relevant step for epoxidation (step 4) or decompose by reaction with fluid-phase H_2O_2 (step 6). Step 6, though depicted as a single elementary step, likely involves the homolysis of M-OOH or M-(η^2-O_2) moieties followed by rapid secondary reactions among radicals to form O_2 and H_2O, as proposed for Ti-silicates,[80] and regenerate the active site. Finally, $C_6H_{12}O$ desorbs in a quasi-equilibrated manner (step 5) to yield the epoxide product.

Figure 2.6 shows turnover rates for 1-hexene (C_6H_{12}) epoxidation depend linearly on the concentration of C_6H_{12} ($[C_6H_{12}]$, where brackets denote the concentration of a species) and do not depend on $[H_2O_2]$ at low ratios of $[C_6H_{12}]$ to $[H_2O_2]$ on groups 4-6 M-BEA. At high ratios of $[C_6H_{12}]$ to $[H_2O_2]$, 1,2-epoxyhexane ($C_6H_{12}O$) formation rates increase in proportion to $[H_2O_2]$, depend weakly on $[C_6H_{12}]$, and depend inversely on $[C_6H_{12}O]$. These sets of coincident behavior signify two distinct kinetic regimes and agree with the mechanism depicted in Scheme 2.2.

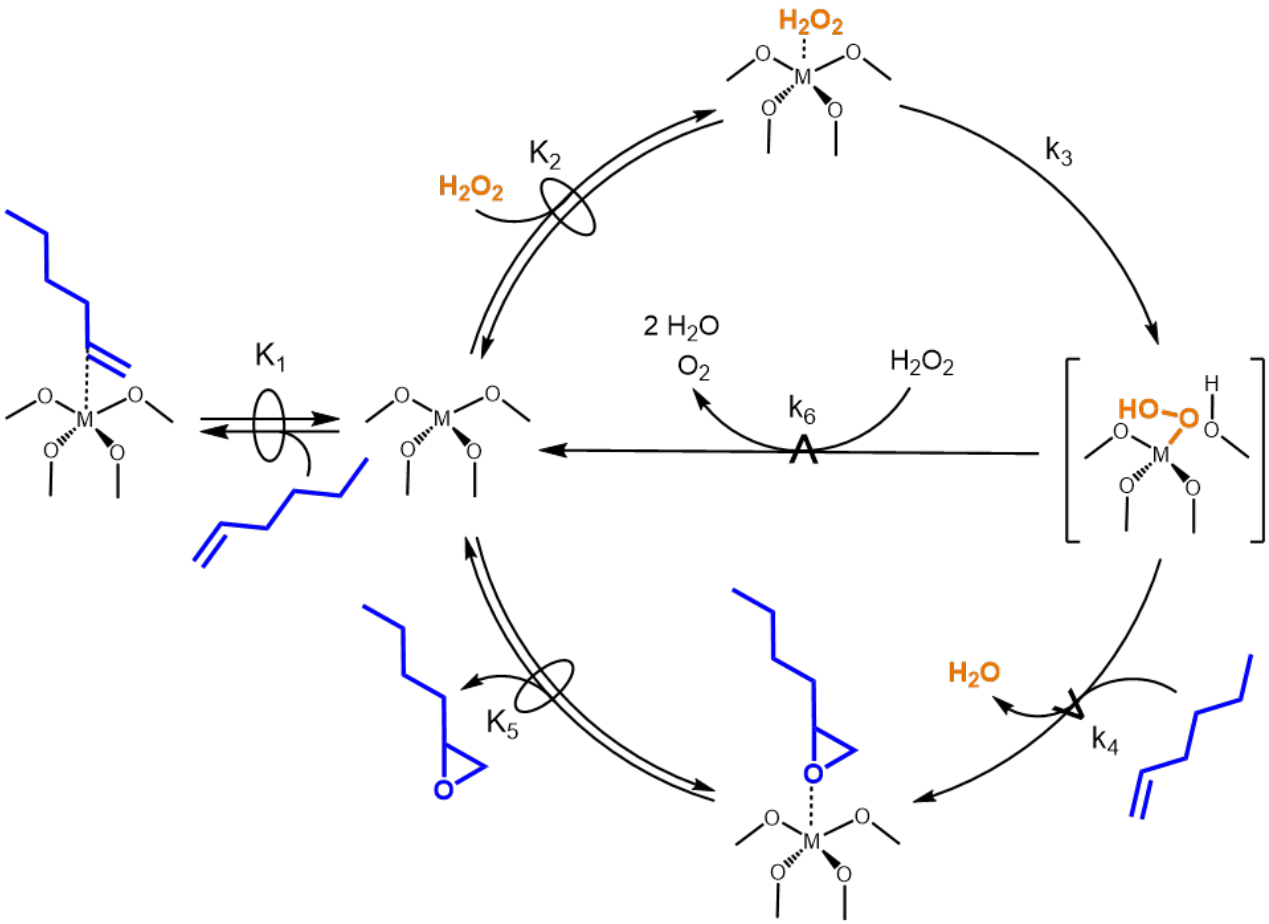

Scheme 2.2. Proposed mechanism for 1-hexene epoxidation with H_2O_2 and H_2O_2 decomposition depicted for group 4 M-BEA. The ⇌ symbol denotes a quasi-equilibrated step and the ⇝ symbol signifies the kinetically relevant steps for the formation of distinct products. Solvent molecules have been omitted for clarity.

Both involve kinetically relevant O-atom transfer from H_2O_2-derived reactive intermediates to C_6H_{12} (see Section 2.3.1), however, the prevailing surface intermediates differ. The first regime contains activated forms of H_2O_2 as the most abundant reactive intermediates (MARI), and the second regime presents sites predominantly covered by the epoxide product.

Scheme 2.2 indicates that rates for epoxidation (r_E) shown in Figure 2.6 can be predicted by a rate expression with the form:

$$r_E = k_4[M-OOH][C_6H_{12}] \tag{2.1}$$

where k_4 is the rate constant for step 4 in Scheme 2.2, and $[M-OOH]$ represents the number of H_2O_2-activated metal sites (the sum of both M-OOH and M-(η^2-O_2)). The functional dependence of r_E on reactant concentrations becomes apparent following use of the pseudo-steady state hypothesis to determine $[M-OOH]$ and by requiring that the sum of all adsorbed species equals the total number of active sites ($[L]$).[10, 19, 23, 65] This treatment yields:

$$\frac{r_E}{[L]} = \frac{\frac{k_3 k_4 K_2 [H_2O_2][C_6H_{12}]}{k_4[C_6H_{12}]+k_6[H_2O_2]}}{1+K_1[C_6H_{12}]+K_2[H_2O_2]+\frac{k_3 K_2 [H_2O_2]}{k_4[C_6H_{12}]+k_6[H_2O_2]}+\frac{[C_6H_{12}O]}{K_5}} \tag{2.2}$$

where the five terms in the denominator represent the numbers of sites occupied by the solvent CH_3CN, C_6H_{12}, H_2O_2, activated forms of H_2O_2, and 1,2-epoxyhexane, respectively. The full derivation of Equation 2 is shown in the Supporting Information (Section A5.0).

At low alkene concentrations, the activated form of H_2O_2 becomes the MARI, and consequently, the rate expression (Equation 2.2) simplifies to:

$$\frac{r_E}{[L]} = k_4[C_6H_{12}] \tag{2.3}$$

which predicts rates that match the observed near-first order dependence on $[C_6H_{12}]$ and lack of dependence on $[H_2O_2]$. High ratios of $[C_6H_{12}]$ to $[H_2O_2]$ cause $C_6H_{12}O$ to saturate active sites and the rate expression becomes:

$$\frac{r_E}{[L]} = \frac{k_3 k_4 K_2 K_5 \, [H_2O_2][C_6H_{12}]}{[C_6H_{12}O](k_4[C_6H_{12}]+k_6[H_2O_2])} \tag{2.4}$$

Equation 2.4 applies to all groups 4-6 M-BEA and describes trends in Figure 2.6 near greater $[C_6H_{12}]$ and lower $[H_2O_2]$ values. This rate expression simplifies further for catalysts with high selectivities for epoxidation (e.g., Ti-BEA selectivities > 90%, Section 2.3.4), because the rate of epoxidation far exceeds that of H_2O_2 decomposition ($k_4[C_6H_{12}] >> k_6[H_2O_2]$) such that:

$$\frac{r_E}{[L]} = \frac{k_3 K_2 K_5 \, [H_2O_2]}{[C_6H_{12}O]} \tag{2.5}$$

which agrees with the experimentally observed kinetic regime for Ti-BEA at a high $[C_6H_{12}]$ to $[H_2O_2]$ ratio where turnover rates do not depend on $[C_6H_{12}]$. Here, the MARI shifts from H_2O_2-derived species to a C_6H_{12}-derived MARI indicated by a near-first order dependence on H_2O_2 and a negative dependence on $C_6H_{12}O$ at high ratios of $[C_6H_{12}]$ to $[H_2O_2]$. The rate expression and corresponding derivation for decomposition of H_2O_2 (step 6) is given in the Supporting Information (Section A5.0).

Rate measurements for 1-hexene epoxidation with H_2O_2 over Ti-, Nb-, and W-BEA suggest all these catalysts utilize the same elementary steps and similar transition states to achieve epoxidations (Scheme 2.2). Yet, epoxidation turnover rates on Ti-BEA are 250- and 60-fold greater than W-BEA and Nb-BEA, respectively, at comparable conditions. These large differences in turnover rates reflect variations in electron affinities of the active sites and stability of the adsorbed epoxide as described next.

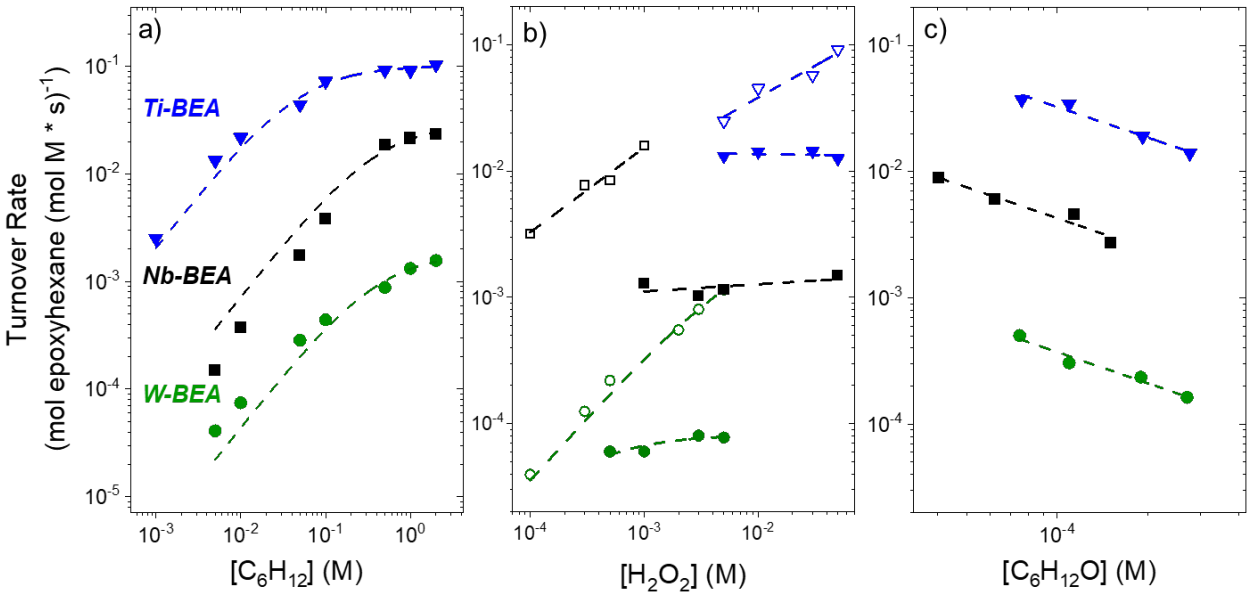

Figure 2.6. Turnover rates for 1,2-epoxyhexane formation in CH_3CN as a function of (a) $[C_6H_{12}]$ over Ti-BEA (blue triangle, solid ▼, 10 mM H_2O_2), Nb-BEA (black square, solid ■, 1 mM H_2O_2), and W-BEA (green circle, solid ●, 1 mM H_2O_2); (b) $[H_2O_2]$ over Ti-BEA (blue triangle, solid ▼, 0.1 mM C_6H_{12}; blue triangle, open ▽, 1 M C_6H_{12}), Nb-BEA (black square, solid ■, 0.5 mM C_6H_{12}; black square, open □, 2 M C_6H_{12}), and W-BEA (green circle, solid ●, 0.5 mM C_6H_{12}; green circle, open ○, 2 M C_6H_{12}); (c) $[C_6H_{12}O]$ over Ti-BEA (blue triangle, solid ▼, 2 M C_6H_{12}, 10 mM H_2O_2), Nb-BEA (black square, solid ■, 1 M C_6H_{12}, 1 mM H_2O_2), and W-BEA (green circle, solid ●, 2 M C_6H_{12}, 1 mM H_2O_2).

2.3.4 Linear Free Energy Relationships for Alkene Epoxidation and H_2O_2 Decomposition

Activation enthalpies (and free energies) for elementary steps depend intimately upon the reaction enthalpies (and free energies) of the same step, as postulated by Hammond.[103, 104] Recently, we demonstrated that heats of adsorption of pyridine (C_5H_5N) and deuterated acetonitrile (CD_3CN) in the gas-phase linearly correlate to activation enthalpies for liquid-phase epoxidation and H_2O_2 decomposition on groups 4-5 transition metal-bearing zeolite BEA.[19, 23, 30] These linear relationships suggest that groups 4-5 M-BEA that bind basic molecules with increasing stability,

quantified as a functional measure of Lewis acid strength, have lower activation enthalpies for liquid-phase epoxidation. While these measurements imply the intrinsic electronic interactions between the transition state and the active site, they do not capture other forms of chemical interactions that affect rate and equilibrium constants pertinent for this reaction. Scheme 2.3 illustrates that the formation of the transition state that forms 1,2-epoxyhexane within the pores of M-BEA requires the displacement and reorganization of solvent molecules (Scheme 2.3a) in ways that should closely resemble the structural changes induced by adsorption of the epoxide product (Scheme 2.3b). Excess free energy contributions that originate from interactions between the transition state, geminal chemical bound to the active site (e.g., hydroxyl or oxos on W atoms), the solvent, and the extended surface of the pores will affect both processes, as demonstrated by linear free energy relationships (LFER) for 1-octene epoxidation across a range of Ti-BEA catalysts with different densities of silanol groups (i.e., hydrophilicities).[30] Here, we account for these additional interactions within linear free energy relationships by using isothermal titration calorimetry (ITC) to directly measure the adsorption enthalpy of 1,2-epoxyhexane ($\Delta H_{ads,epox}$) onto M-BEA in the aqueous acetonitrile reaction solvent. 1,2-Epoxyhexane is a suitable titrant for these measurements (e.g., rather than pyridine, an alkene or an epoxide with a different alkyl group), because measured heats of adsorption reflect a combination of specific and non-specific interactions between the adsorbate, the framework metal atom, the zeolite pore wall and the confined solvent molecules. Specifically, we expect a certain enthalpic stabilization from the interaction between the oxirane ring and the framework metal center but also contributions from solvent displacement and restructuring that reflect the size of the epoxide (i.e., the van der Waals volume and surface area). Consequently, we anticipated that 1,2-epoxyhexane and values for $\Delta H_{ads,epox}$ would serve as the

most representative surrogate for the epoxide-like transition state (Scheme 2.3) and the complete set of interactions with its surroundings.

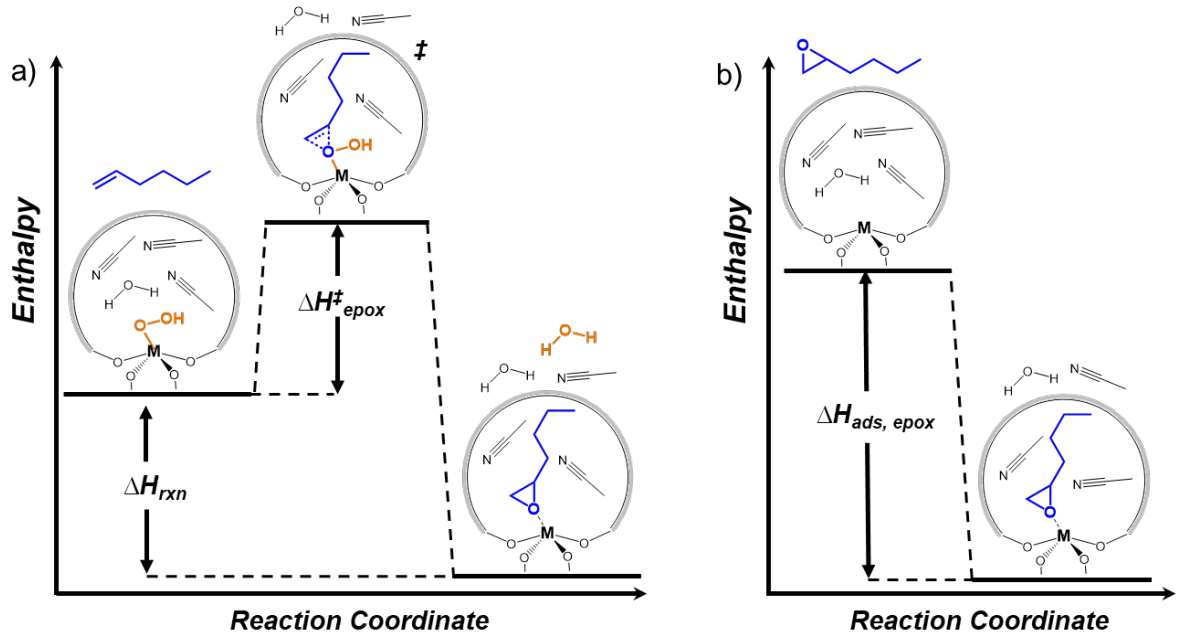

Scheme 2.3. Changes in enthalpy that correspond to (a) the formation of the transition state for epoxidation ($\Delta H^{\ddagger}_{epox}$) and the epoxide ($\Delta H_{rxn}$) from C_6H_{12} and a M-OOH intermediate; and (b) the adsorption of 1,2-epoxyhexane to the active site of an M-BEA catalyst (depicted for a group 4 metal).

Figure 2.7 presents apparent activation enthalpies for 1-hexene epoxidation ($\Delta H^{\ddagger}_{epox}$, Scheme 2.3a) and H_2O_2 decomposition ($\Delta H^{\ddagger}_{dec}$) measured on M-OOH saturated sites for all M-BEA to enable equitable comparisons between materials. The differences in $\Delta H^{\ddagger}_{epox}$ (21 – 77 kJ mol^{-1}) and $\Delta H^{\ddagger}_{dec}$ (38 – 49 kJ mol^{-1}) between group 4-6 M-BEA for 1-hexene epoxidation are consistent with previous reports for cyclohexene[10] and styrene[23] epoxidation with H_2O_2, where lower $\Delta H^{\ddagger}_{epox}$ corresponds to higher rates and selectivities for epoxidation over M-BEA (Figure 2.7).

Values of $\Delta H_{ads,epox}$ were measured by ITC in liquid solutions with compositions that resemble the reaction solvent. We titrated a slurry of ~20-30 mg of M-BEA in CH_3CN (39 mM H_2O, 313 K) with a solution of 1,2-epoxyhexane in CH_3CN (39 mM H_2O, 313 K). Figure 2.8 depicts a representative thermogram for 1 μl injections of the titrant solution, in which the titrant coverage increases with number of injections and time. As the experiment proceeds, the areas for peaks remain nearly constant but the maximum intensity decreases, because 1,2-epoxyhexane must diffuse further into the M-BEA particles to access unoccupied sites. Figure 2.9 shows heats measured for each injection, which represent the peak areas in Figure 2.8 normalized by the number of 1,2-epoxyhexane molecules within each injection. These measurements were performed at low titrant to metal atom ratios ($\theta_{epox,M} < 0.2$) to ensure every titrant molecule binds to active sites (all isotherms and thermograms are displayed in Figure A10). Table 2.3 contains the measured enthalpies of adsorption for 1,2-epoxyhexane ($\Delta H_{ads,epox}$) for Ti-BEA, Nb-BEA and W-BEA, and these values show that $C_6H_{12}O$ binds most strongly to Ti active sites (-134 ± 2 kJ mol^{-1}) and least strongly to W active sites (-97 ± 2 kJ mol^{-1}). Comparisons of heats of adsorption for $C_6H_{12}O$, CD_3CN,[10, 23] (Table 2.3) and C_5H_5N[23] indicate that basic molecules consistently bind more exothermically to framework Ti sites than to Nb sites and support the idea that Ti atoms have greater electron affinities than Nb or W atoms in the BEA framework.

The observed trends for both apparent activation enthalpies ($\Delta H^{\ddagger}_{epox}$, $\Delta H^{\ddagger}_{dec}$; Figure 2.7) and adsorption enthalpies (e.g., $\Delta H_{ads,epox}$; Table 2.3) demonstrate that that W-BEA stabilizes transition states and products for epoxidation less effectively than Ti-BEA and Nb-BEA, despite the greater electronegativity of W.

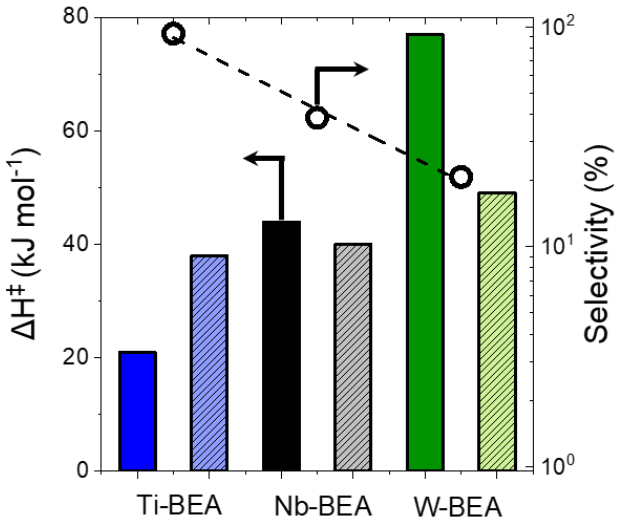

Figure 2.7. Apparent activation enthalpies ($\Delta H^{\ddagger}_{epox}$, solid bars; $\Delta H^{\ddagger}_{dec}$, dashed bars) and 1-hexene epoxidation selectivities on M-OOH saturated sites in CH_3CN (303-333 K) for Ti-BEA (0.5 mM C_6H_{12}, 10 mM H_2O_2, 39 mM H_2O), Nb-BEA (5 mM C_6H_{12}, 1 mM H_2O_2, 3.9 mM H_2O) and W-BEA (5 mM C_6H_{12}, 1 mM H_2O_2, 3.9 mM H_2O).

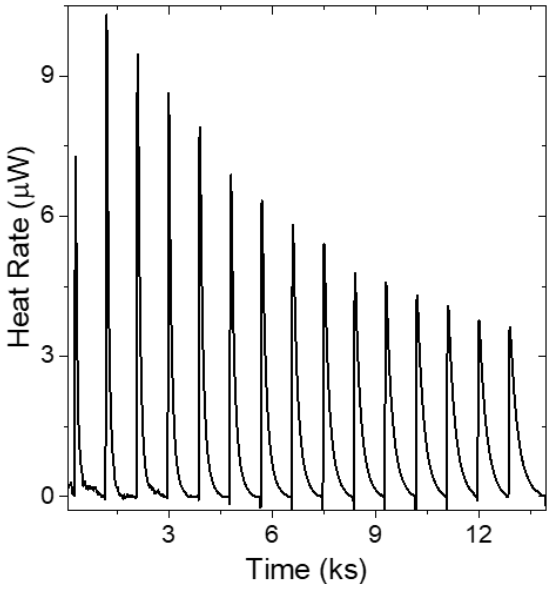

Figure 2.8. Thermogram from the titration of W-BEA with 1,2-epoxyhexane (10 mM $C_6H_{12}O$ in CH_3CN) during isothermal titration calorimetry (39 mM H_2O, 313 K, 1uL per injection).

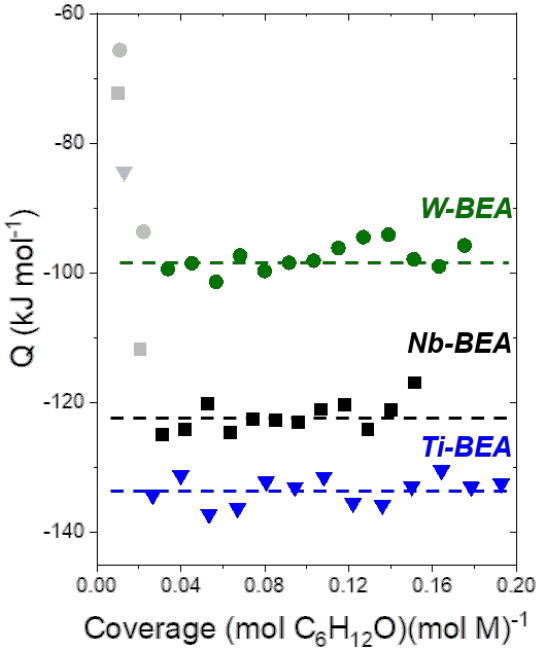

Figure 2.9. Heats released upon 1,2-epoxyhexane adsorption in CH_3CN (39 mM H_2O, 313 K) on Ti-BEA (blue triangle ▼), Nb-BEA (black square ■), and W-BEA (green circle ●) as a function of 1,2-epoxyhexane coverage. Transparent points are omitted from analysis due to common errors associated with early injections.

We hypothesized that W, the most electronegative among the metals incorporated into BEA (Figure A11), would present the smallest $\Delta H^{\ddagger}_{epox}$ by withdrawing electron density from reactive oxygen species and increasing their electrophilicity. The Pauling and Sanderson electronegativities of these elements do not correlate to either $\Delta H^{\ddagger}_{epox}$ or $\Delta H_{ads,epox}$ values on these M-BEA. These electronegativity scales reflect elemental properties that apparently do not extend accurately to groups 4-6 metals as present in the zeolite framework. The lack of correlation is not surprising, because these metals acquire distinct coordination structures to framework of BEA and different numbers and types of geminal oxygen functions.

Table 2.3. Adsorption Enthalpies for 1,2-Epoxyhexane and CD_3CN on M-BEA.

Catalyst	$\Delta H_{ads,epox}$[a] (kJ mol^{-1})	$\Delta H_{ads,CD3CN}$[b] (kJ mol^{-1})
Ti-BEA	-134 ± 2	-31 ± 2
Nb-BEA	-122 ± 2	-22 ± 2
W-BEA	-97 ± 2	n.d.[c]

[a] titrant surface coverage is 0-0.2 mol 1,2-epoxyhexane (mol metal)$^{-1}$ (39 mM H_2O in CH_3CN, 313 K, 250 rpm); [b]values taken from Reference 23; [c]not determined because CD_3CN deactivates Lewis acid sites on W-BEA at temperatures > 373 K

Mulliken electronegativities correlate linearly with values of $\Delta H^{\ddagger}_{epox}$, $\Delta H^{\ddagger}_{dec}$, and $\Delta H_{ads,epox}$, however, these relationships contradict our initial hypothesis and indicate that the metals with greater electron affinities give rise to weaker adsorption of 1,2-epoxyhexane (Figure A11a) and greater $\Delta H^{\ddagger}_{epox}$ (Figure A11b). Mulliken electronegativities represent an average of the electron affinity and the first ionization energy of a given element,[105] but these calculations cannot account for differences in oxidation states, the number and type of ligands, or bond angles and lengths for the metal as it exists during catalysis in BEA. These realizations and the nonintuitive anticorrelation between $\Delta H_{ads,epox}$ and Mulliken electronegativites show the need to interrogate molecular interactions at these sites experimentally.

Despite these complicating factors, Figure 2.10 shows values of $\Delta H^{\ddagger}_{epox}$ and $\Delta H^{\ddagger}_{dec}$ decrease linearly as $\Delta H_{ads,epox}$ values increase for Ti-, Nb, and W-BEA. The linear free-energy relationship for $\Delta H^{\ddagger}_{epox}$ demonstrates that the interactions of 1,2-epoxyhexane with active sites (and their distinct sets of hydroxyl and oxo groups) resemble closely the interactions of the transition state for epoxidation and obeys Hammond's postulate notwithstanding the significant

differences between the structure of active sites. Notably, $\Delta H^{\ddagger}_{epox}$ is more sensitive to $\Delta H_{ads,epox}$ (slope of correlation equal to 1.5 ± 0.2, Figure 2.10), which must stem from the structural similarities between the transition state and the adsorbate. These similarities cause the adsorbate to experience a combination of covalent, specific (e.g., hydrogen-bonding with the solvent and pore wall) and non-specific (van der Waals forces) interactions comparable to those that act upon the transition state. Values for $\Delta H^{\ddagger}_{dec}$ also scale linearly with $\Delta H_{ads,epox}$ but do so much more weakly (slope equal to 0.3 ± 0.01, Figure 2.10), because both the covalent and (non)-specific interactions differ between the transition state for H_2O_2 decomposition and adsorbed 1,2-epoxyhexane, as expected. These trends in $\Delta H_{ads,\,epox}$ values show that the lone pairs of the oxirane ring bind more strongly to Ti- and Nb-atoms in BEA, which implies these sites have greater electron affinities than W-atoms. The electron affinity of these sites impacts catalysis by regulating the electrophilicity of reactive oxygen species that exchange electrons with the electron-rich C=C bonds of C_6H_{12} and attack H_2O_2.

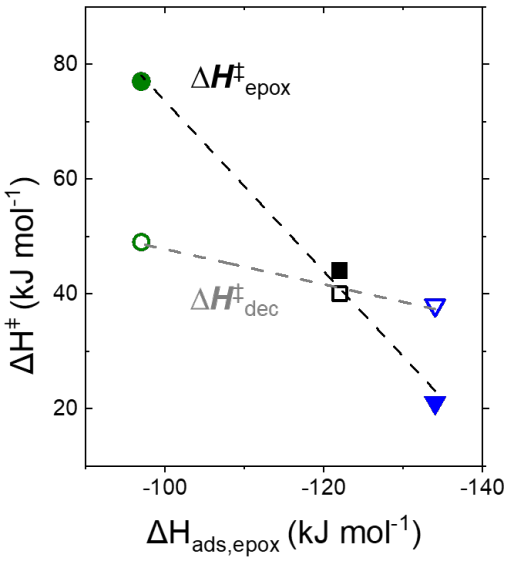

Figure 2.10. Apparent activation barriers for 1-hexene epoxidation in CH_3CN over Ti-BEA (blue triangle, solid ▼, 0.5 mM C_6H_{12}, 10 mM H_2O_2), Nb-BEA (black square, solid ■, 5 mM C_6H_{12},

Figure 2.10. (cont.) 1mM H_2O_2), and W-BEA (green circle, solid ●, 5 mM C_6H_{12}, 1 mM H_2O_2); and H_2O_2 decomposition in CH_3CN over Ti-BEA (blue triangle, open ▽, 1 mM H_2O_2, 3.9 mM H_2O), Nb-BEA (black square, open □, 1 mM H_2O_2, 3.9 mM H_2O), and W-BEA (green circle, open ○, 1 mM H_2O_2, 3.9 mM H_2O) as functions of 1,2-epoxyhexane heat of adsorption on M-BEA (W, green circle, solid ●, green circle, open ○; Nb, black square, solid ■, black square, open □; Ti, blue triangle, solid ▼, blue triangle, open ▽).

Notably, these trends in turnover rates and activation barriers differ from those previously reported for Ti and Nb silicates[13, 14, 34] and Ti and Nb-POMs[38, 39] where Nb materials revealed lower activation barriers and higher rates and selectivities for cyclooctene and cyclohexene epoxidation than those measured for their Ti counterparts. These differences could possibly be attributed to several factors, which include the relevance of distinct reactive intermediates between these studies and differences between the structure and form of the support for the active sites (e.g., tungstate POM or BEA zeolite). Here, we compared turnover rates and measured $\Delta H^{\ddagger}_{epox}$ at reaction conditions that ensured that H_2O_2-derived intermediates comprised the MARI upon all M-BEA catalysts. The reaction conditions employed to obtain activation energy measurements in prior work appear to result in active sites that are covered by several surface intermediates (i.e., both those derived from H_2O_2 and from cyclooctene) that exist at comparable coverages.[14] In addition, the supports that bind the active Ti and Nb differ significantly (i.e., amorphous silicates, Lindqvist-type tungstate POM, and BEA zeolite). Despite differences between the relative epoxidation turnover rates and apparent activation barriers among Ti-, Nb-, and W-BEA catalysts and those in prior reports on Ti- and Nb-silicate and POM materials, the findings among all reports do agree with the broad conclusion that active sites with greater electrophilicity (or Lewis acidity) provide higher turnover rates and lower activation barriers. We have directly examined the electrophilicity of sites in M-BEA catalysts by comparisons between LMCT energies obtained by

in situ UV-Vis experiments and quantified the enthalpy of adsorption of 1,2-epoxyhexane (a transition state mimic) by isothermal titration calorimetry. Both methods demonstrate that Ti-BEA presents active sites with greater electrophilicities (and greater Lewis acid strength) than Nb-BEA, which agrees with the considerably lower activation enthalpies for epoxidations on Ti-BEA and current understanding of structure function relationships for epoxidation catalysts.

2.4 Conclusions

Differences in the elemental identity of metal atoms substituted into the framework of zeolite catalysts influence rates and selectivities for alkene epoxidation reactions, and other liquid-phase chemistries, by stabilizing reactive intermediates and transition states through combinations of covalent, specific, and non-specific interactions. These differences cannot be accurately predicted based upon intrinsic properties (e.g., electronegativities) of the transition metal elements that form active sites alone, however, Hammond's postulate provides guidance for developing simple methods to probe the combination of these interactions using adsorption measurements. These concepts were investigated here by examining H_2O_2 activation and 1-hexene epoxidation over a series of groups 4 – 6 transition metal substituted zeolite BEA catalysts, which possess predominantly monomeric metal atoms located at tetrahedral positions of the BEA framework. *In situ* UV-Vis and Raman spectroscopy show these M-BEA materials form similar pools of reactive oxygen intermediates (M-OOH and M-(η^2-O_2)) following H_2O_2 activation, however, products of cis-stilbene epoxidation indicate that M-OOH intermediates dominate epoxidations on Ti-BEA while M-(η^2-O_2) are responsible for reactions on Nb- and W-BEA. 1-Hexene epoxidation occurs within Ti-, Nb-, and W-BEA catalysts with functionally identical dependencies on C_6H_{12} and H_2O_2 concentrations, despite differences in rates that span two-orders of magnitude. Comparisons across

these M-BEA catalysts at comparable conditions show epoxidation selectivities are greatest on Ti-BEA (93%), followed by Nb- (38%) and W-BEA (20%) and turnover rates (determined using *in situ* site titrations) are 250- and 60-fold lower on W-BEA and Nb-BEA than Ti-BEA, respectively. These large kinetic differences result from differences in the stability of the epoxidation transition state, relative to the reactive M-OOH intermediates, and not from differences in mechanism or numbers of active sites.

The stability of transition states is inferred through measurements of apparent activation enthalpies ($\Delta H^{\ddagger}$) and do not correlate with measures of the electronegativities of the transition metal atoms located within the framework of zeolite BEA. The lack of correlation suggests that these active sites stabilize transition states through a collection of interactions that cannot be completely described by the tendency of the metal atom to attract electrons and must be assessed by a more comprehensive probe of the interactions. Liquid-phase adsorption enthalpies of 1,2-epoxyhexane ($\Delta H_{ads,epox}$) measured within the reaction solvent by isothermal titration calorimetry (ITC) provides one method to quantify the complete set of interactions. Values of $\Delta H_{ads,epox}$ show W-BEA binds 1,2-epoxyhexane less strongly than Ti- and Nb-BEA, even though W was anticipated to possess the greatest electron affinity, which suggests that differences between the structure and coordination of these metal atoms within the BEA framework introduce catalytically consequential variations in the electronic structure of the metal site and the number and nature of pendant functional groups (e.g., -OH, =O, SiOH) that interact directly and indirectly with transition states. $\Delta H^{\ddagger}$ values for epoxidation and H_2O_2 decomposition decrease linearly as the adsorption of the epoxide becomes more exothermic, which shows that 1-hexene epoxidation follows a simple linear free energy relationship that provides a more meaningful descriptor for catalytic performance than tabulated electronegativities of the elements within these zeolite catalysts.

The relationships developed between these kinetic, spectroscopic, and calorimetric studies provide an explanation for the differences in the observed epoxidation turnover rates, selectivity, and apparent activation enthalpies for M-BEA catalysts. These findings suggest rates and selectivities for epoxidation reactions can be improved simultaneously by increasing the functional electron affinity (or Lewis acidity) of active sites within zeolite frameworks and that reported electronegativities of elements do not provide a sufficient description to predict the behavior of the active sites in various coordination environments. Moreover, these results serve to remind us of the insight gained from constructing appropriate comparisons between kinetic and thermodynamic properties of catalytic materials in complex environments.

CHAPTER 3

IDENTITY OF METAL OXIDE SUPPORT CONTROLS OUTER SPHERE INTERACTIONS THAT AFFECT RATES AND BARRIERS FOR ALKENE EPOXIDATION AT ISOLATED TI ATOMS[i]

3.1 Introduction

Epoxidation reactions produce solvents, surfactants, and materials used in food (e.g., limonene and α-pinene epoxides), cosmetics, and physiologically active components for the pharmaceutical industry.[3] Many catalytic epoxidation reactions utilize homogeneous or heterogeneous transition metal-based catalysts and organic oxidants (ethylbenzene hydroperoxide, tert-butyl hydroperoxide) or inorganic oxidants (H_2O_2).[15, 44] The incorporation of titanium atoms into the framework of zeolite MFI was a landmark achievement that provided a solid catalyst with exceptional rates and selectivities for the epoxidation of propylene with H_2O_2 in aqueous methanol (reported by ENI in 1983[106]). Ti-MFI remains one of the most efficient and widely-used heterogeneous catalysts for this reaction.[27, 28] This technology instigated subsequent studies that sought to understand the attributes of the active site environment (active metal identity,[9, 10, 13, 14] microporous environment,[19, 23] solvent identity and structure,[11, 12, 107] etc.) that influence turnover rates and selectivities for alkene epoxidation with H_2O_2.

Modification of active site environments with the intent to adjust inner or outer sphere interactions can lead to significantly higher turnover rates and selectivities. Multiple strategies have been used to modify the electronic structure (e.g., electron affinity) of the transition metal

---

i This chapter has been reproduced, with permission, from the following publication:
E. Zeynep Ayla, Darshan Patel, Arzam Harris, and David W. Flaherty, "Identity of Metal Oxide Support Controls Outer Sphere Interactions That Affect rates and Barriers for Alkene Epoxidation at Isolated Ti Atoms", *Journal of Catalysis,* **2022**, 411, 167-176.

centers that bind reactive forms of oxygen involved in elementary steps for epoxidation and H-abstraction over solid catalysts. Some of these methods intend to use first coordination sphere interactions (i.e., covalent or ionic bonding) to modify reactivity and include changes in the identity of the active metal atom[9, 10] and additions of organic and inorganic surface ligands[18, 84, 108] to influence electron density near the active site. However, surface modifications that introduce new elements or modify local topology can also introduce surface moieties with distinct hydrogen-bonding character or pK_a values, that create differences in outer sphere (i.e., non-covalent) interactions near the solid-liquid interface.[11, 12, 23, 102, 109-111] Individually or combined, these inner and outer sphere relationships influence the free energies of catalytic transition states.

Early transition metals (e.g., Ti, Nb, Ta, Mo, W, etc.) activate H_2O_2 for alkene epoxidation[32], however, Ti received significant attention due to comparatively high turnover rates and selectivities when incorporated onto silicate supports.[9, 10] Combining experiment and electronic structure simulation, Boronat et al. linked the success of isolated Ti active sites for alkene oxidation to their intrinsic Lewis acid strength (i.e., the metal center's ability to form acid-base adducts).[40] They proposed that differences between computational estimates for the energy of the lowest unoccupied molecular orbital (LUMO) of H_2O_2-activated transition metal centers gave rise to order of magnitude differences in hydrocarbon oxidation rates and demonstrated that Ti centers give greater turnover rates for alkene epoxidation than Sn and Zr sites in zeolite BEA, a silica-based support. Later, we compared rates, selectivities, and mechanisms for groups 4-6 atoms substituted at framework positions within zeolite BEA that demonstrated Ti- BEA provides higher turnover rates and selectivities (>90 %) for 1-hexene epoxidation than other group 4 -6 M-BEA catalysts.[9] These differences reflect apparent activation enthalpies ($\Delta H^{\ddagger}$) for epoxidation and H_2O_2 decomposition that correlate linearly with ligand-to-metal charge transfer (LMCT) energies

of the metal hydroperoxo (M-OOH) and metal peroxo (M-O_2) complexes[10, 23] but also with the enthalpies of adsorption of the epoxide product to the transition metal active site of M-BEA catalysts.[9] Taken together, these results provide strong evidence that active sites with the greatest functional Lewis acid strength form H_2O_2-derived reactive species that offer the lowest $\Delta H^{\ddagger}$ for epoxidation. Consequently, other factors that may influence the electronic properties (i.e., LUMO energy) of Ti or other transition metal centers may provide methods to increase turnover rates and selectivities for oxidation reactions.

Besides varying the active metal atom, multiple strategies have been used to adjust the electronic structure and density near reactive species bound to transition metal sites, by employing ligands and other metal atoms as extensions of the surface to act as promoters for oxidation. For example, Tatsumi et al. reported that adding trimethylsilyl groups to Ti-MCM-41 increased cyclohexene epoxidation selectivities by 13% in addition to inhibiting H_2O_2 decomposition.[112] In the same year, Oldroyd et al. found that deposition of Ge atoms upon MCM-41 followed by addition of Ti with molar ratios of Ge to Ti of 0.07 to 1) increased turnover rates for cyclohexene epoxidation with cumene hydroperoxide by 10%, while deposition of Sn atoms followed by Ti reduced turnover rates by 59%.[108] These changes were attributed to the electronic modification of Ti centers through Ti-O-Ge bonds and to the Ti site deactivation caused by SnO_2. Similarly, Tilley et al. modified surfaces of Ti-SiO_2 catalysts with trialkylsilane[84] and Ta-SiO_2 catalysts with trimethyl group 14 (M = Si, Ge, Sn)[18] ligands, to improve cyclohexene epoxidation selectivities as much as 40% and 50%, respectively. They concluded that modified metal centers with Ti-O-Ge or additional Ti-O-Si linkages are more electron deficient than their unmodified counterparts, which leads to more electrophilic M-O_2 and M-OOH species that provide lower barriers for oxygen transfer. In another study, Fang and coworkers report on improved 1-hexene epoxidation activity

of Ti incorporated into zeolite MWW by post-synthetic treatments with NH_4F with the intent to increase the Lewis acid strength of Ti atoms by incorporating vicinal fluorine atoms.[113]

Notably, surface modifications intended to modify the electronic structure of active sites by first coordination sphere interactions may cause other significant changes. For example, addition of other elements to a solid catalyst may modify the isoelectric point (IEP), pK_a based on support identity, and hydrogen bonding properties of the surface. Such changes can affect the organization of the solvent at the solid-liquid interface and impact catalysis through second coordination sphere effects (i.e., excess thermodynamic contributions).[11, 12, 19, 23, 30, 114-116] Extensive studies of zeolite pore polarity agree that increasing hydrophilicity (number of silanol groups within the micropore (and near the active site) encourage water adsorption on surfaces.[12, 30, 117] Specifically, increasing silanol density lowers free energy barriers for epoxidations by entropically stabilizing the catalytic transition state through hydrogen-bonded water networks in aqueous solvents.[23, 118] In certain cases, however, surfaces with affinity to solvent molecules can cause competition for active sites.[119-122] Lower turnover rates for thiophene oxidation were observed with increasing Lewis basicity of the solvent[65], implying that increasing Lewis acidity of the surface could cause substrate inhibition in a similar way. Considering the possibility of the presence of one or more of these effects (H-bond stabilization, competitive adsorption based on surface electrophilicity), metal oxide surface charge in catalytic reactions, especially in aqueous solvents and with electron-rich reactant groups (e.g., alkenes), can play an essential role in rates and selectivities.

Here, we examine titanium atoms supported on metal oxides (SiO_2, Al_2O_3, ZnO, GeO_2) to gain understanding for how inner and outer sphere interactions may influence epoxidation reactions. A combination of kinetic and spectroscopic evidence demonstrates that catalysis at

atomically disperse Ti active sites depends sensitively on the identity of the metal oxide support, due primarily to measurable outer sphere properties. The mechanism for 1-hexene epoxidation with H_2O_2 in acetonitrile remains constant for all metal oxide supported Ti catalysts (Ti-MO_x), which allows for direct comparisons between apparent activation enthalpies for epoxidation ($\Delta H^{\ddagger}_{epox}$). Turnover rates for 1-hexene epoxidation differ by four orders of magnitude across these Ti-MO_x catalysts and reflect significant differences between $\Delta H^{\ddagger}_{epox}$ and $\Delta S^{\ddagger}_{epox}$ across these materials. Yet, *in situ* UV-Vis spectra of Ti-OOH and Ti-O_2 complexes indicate LMCT energies for these H_2O_2-derived intermediates fall within a narrow range (~0.1 eV) of values. Similarly, *in situ* Raman spectra show that the vibrational structures of the Ti-O_2 complexes (e.g., ν(Ti-(η^2-O_2))) remain indistinguishable across Ti-MO_x samples. Together, these observations suggest that differences in turnover rates and $\Delta H^{\ddagger}_{epox}$ originate largely from outer-sphere effects. Correlations between $\Delta H^{\ddagger}_{epox}$ and values of the IEP and water uptake onto the metal oxides suggest that the surface charge of the support impacts epoxidation catalysis by controlling the solvent compositions and structure at the solid-liquid interface that contains the active site. The relationships established here provide compelling evidence that the identity of the metal oxide supports may affect catalysis on isolated active sites in ways other than the direct inner sphere modifications commonly invoked. These findings expand understanding of the impact of the solid-liquid interface on catalysis and guide creation of increasingly effective epoxidation catalysts.

3.2 Materials and Methods

3.2.1 Catalyst Synthesis

Ti-MO_x catalysts were synthesized by grafting titanocene dichloride ($TiCp_2Cl_2$) complexes onto metal oxide surfaces using a previously established method.[123] Supports used included SiO_2 (SBA15, ACS Material, 610 $m^2\ g^{-1}$), γ-Al_2O_3 (Millipore Sigma, 40 $m^2\ g^{-1}$), ZnO (Millipore Sigma,

11 m^2 g^{-1}), and GeO_2 (Millipore Sigma). Prior to grafting Ti-complexes to surfaces, each metal oxide was heat treated to (823 K, 4 K min^{-1}) in flowing dry air (100 cm^3 min^{-1}, Airgas, Ultra Zero Grade) for 6 h to minimize loss of surface area or further aggregation in later synthesis steps. Treated solid powders were transferred to a round bottom flask attached to a Schlenk line and heated under vacuum (< 5 Pa, 473 K) for 2 h to remove free water molecules. The titanocene dichloride precursor was dissolved in chloroform (Fisher Chemicals, 20 cm^3 g_{MOx}^{-1}) in a separate beaker, and the solution was then added to the round bottom flask containing the dried metal oxide under Ar purge at room temperature. The light orange-red mixture was stirred (200 rotations per minute (rpm)) with the metal oxide powder for 0.5 h, after which, triethylamine (Et_3N) was added to achieve a molar ratio of Et_3N to titanocene dichloride equal to 3. The addition of Et_3N is intended to deprotonate the metal oxide surface to facilitate rupture of Ti-Cl bonds and adsorption of the Ti-complex to anionic oxygen sites. This process produces a white vapor of HCl, which indicates the grafting procedure is successful. The resulting slurry was stirred (~12 h) at ambient temperature, and subsequently, the solvent was removed by rotary evaporation (IKA, RV 10). The recovered solids were heat treated (823 K, 4 K min^{-1}) in flowing dry air (100 cm^3 min^{-1}, Airgas, Ultra Zero Grade) for 6 h to yield the Ti-MO_x catalysts, which appear as white powders.

3.2.2 Catalyst Characterization

The Ti content of the Ti-MO_x samples, reported in Table 3.1, were determined by energy dispersive x-ray fluorescence (EDXRF). Finely ground samples of Ti-MO_x (~ 50 mg) were placed in a 1 cm-diameter sample holder, sealed with an ultralene film, and loaded into the He-purged chamber of the EDXRF spectrometer (Shimadzu, EDX-7000). The sample was scanned between 0 and 30 keV, and the elemental composition of the sample was calculated using the relative intensities of the corresponding fluorescence peaks. Elemental analysis of the metal oxide supports

using EDXRF shows negligible changes in the Cl content of the samples before and after Ti grafting, which indicates the absence of residual Cl atoms from the titanocene dichloride precursor (Table B1).

The dispersity of Ti atoms grafted onto MO_x supports was examined by diffuse reflectance UV-Vis (DRUV-vis) spectroscopy to measure metal band gap energies using a UV-vis spectrophotometer (Varian Cary 5G). Ti-MO_x samples were mixed and ground with magnesium oxide (MgO; Sigma Aldrich, 99.995 %) at a MgO to Ti-MO_x mass ratio of 10:1, and pure MgO was used to obtain background spectra. Table 3.1 includes band gap energies determined by extrapolating the linear portion of the Tauc plots (Figure B1) to the horizontal axis to determine the energy of photons absorbed (eV). The high absorbance of ZnO in the similar region does not permit meaningful measurements of the band gap for Ti on ZnO (Figure B1). The densities of Ti atoms on the four supports ranges from 0.10 – 1.54 Ti atoms nm^{-2} and the band gaps range from 4.81 - 4.87 eV. These band gaps far exceed that for bulk TiO_2 (3.2 eV and indicate the grafted Ti atoms are highly disperse on the MO_x surfaces.[124] Figure 3.1 displays the band gaps, measured by DRUV-Vis spectroscopy, for SiO_2 materials with a range of Ti contents and surface densities. While Ti densities differ among the materials due to a variety of surface areas, Figure 3.1 demonstrates that densities less than 0.6 Ti atoms nm^{-2} show band gaps of higher energy than that of TiO_2 and maintain high monomer to oligomer ratios of Ti atoms. While we were unable to measure the band gap of Ti when grafted on ZnO, we assume the Ti-ZnO catalyst with a Ti density of 0.35 Ti atoms nm^{-2} is similarly and sufficiently disperse.

Table 3.1. Ti Loading, Ti Density, and Band Gap of Ti-MO_x Samples Used

Catalyst	Ti loading (wt %)[a]	Ti density (Ti atoms nm^{-2})	Band gap (eV)[b]
Ti-SiO_2	0.40	0.10	4.87
Ti-ZnO	0.017	0.35	n.d.[c]
Ti-GeO_2	0.0078	0.70	4.81
Ti-Al_2O_3	0.49	1.54	4.67

[a]measured by EDXRF (Section 3.2.2), [b]determined by DRUV-vis (Section 3.2.2, Figure B1), [c]not determined; UV-Vis absorption by grafted Ti atoms is convoluted by significant absorption by ZnO

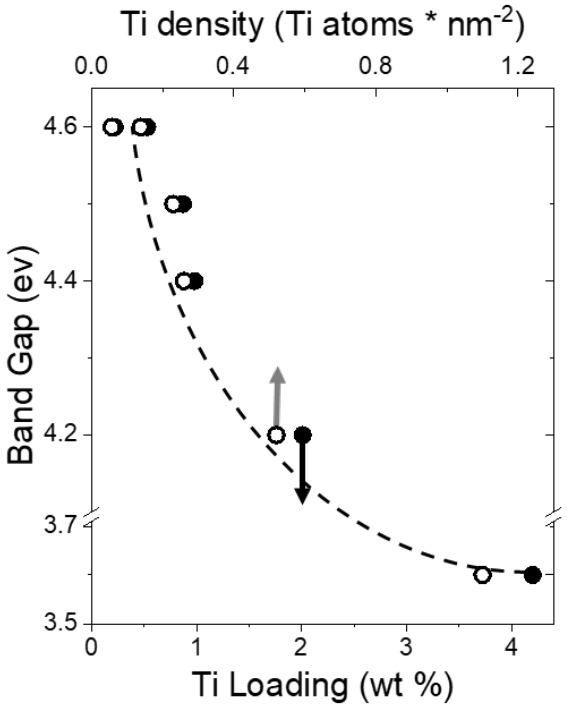

Figure 3.1. Band gap of Ti-SiO_2 as a function of Ti loading (solid circles) and Ti density (hollow circles), dashed curve provided to guide the eye.

3.2.3 Turnover Rate Measurements for Epoxidation and H_2O_2 Decomposition

Turnover rate measurements for 1-hexene epoxidation with H_2O_2 were performed in stirred batch reactors (700 rpm) at differential conversion (< 10 %). 1-Hexene (Millipore Sigma, ≥ 99%), H_2O_2 (Macron, 30% in H_2O), and decane (Millipore Sigma, ≥ 99%) as internal standard for gas chromatography, were stirred in CH_3CN (Millipore Sigma, ≥ 99.9%) held at temperature (313 - 338 K). An initial aliquot (~ 0.5 ml) was collected after 0.5 h to confirm the initial composition of the solution. Then, the Ti-MO_x catalyst (0.05 – 1 g) was added to initiate the reaction, and aliquots were collected at regular intervals using a syringe equipped with a polypropylene filter (Tisch Scientific, 0.05 μm) to separate catalyst particles from solution and halt the reaction. Products were analyzed with a gas chromatograph (Agilent, 5890) equipped with an HP-1 column (30 m, 0.32 mm, 0.25 μm), flame ionization detector, and liquid autosampler (Hewlett-Packard, HP 6890 Series). When performing rate measurements, the number of Ti atoms within the reactor was controlled in order to obtain quantifiable concentrations of the epoxide product across all catalysts. While the total number of Ti atoms within the reactor varied by a factor of 20, the mass of catalyst used would vary from 0.045 – 0.9 g based on the turnover rate and mass loading of the specific material. Replicated rate measurements indicate that the experimental uncertainty of these measurements is ~15%.

Hot filtration experiments were performed to determine if Ti atoms leach from each of the metal oxide support to form homogeneous complexes active for epoxidation. During a batch reaction, a large aliquot of the reaction mixture (~10 ml) was extracted at 20 - 100 min, filtered (0.05 μm syringe filter), and transferred into a stirred 20 ml vial heated at reaction temperature (313 - 323 K). Aliquots were taken from both the original reaction solution and the filtered solution over time and the concentrations of products were measured by gas chromatography. Hot filtration

tests demonstrate that Ti atoms do not leach from MO_x to form soluble complexes active for epoxidation (Figure B2). In addition, epoxidation rates normalized per gram of catalyst are more than 100 times lower for the bare metal oxide support (i.e., in the absence of Ti atoms) than for the corresponding Ti-MO_x materials (Figure B3). Moreover, Ti content was measured compared between the as-synthesized Ti-MO_x and catalysts filtered post-reaction, showing no loss of Ti atoms from the support. Together, these control experiments demonstrate that catalytic turnovers for 1-hexene epoxidation occur only at Ti-atoms bound to metal oxide surfaces.

Rates for hydrogen peroxide decomposition over Ti-MO_x were measured using colorimetric titration with a titrant solution of $CuSO_4(H_2O)_5$ (8.3 mM; VWR, 99%) and neocuproine hydrate (12 mM; SAGECHEM) in an aqueous solution of ethanol (4.3 M; Decon Laboratories, 100%). Aliquots (0.15 ml) from batch reactions (0.5 - 1 mM H_2O_2, 1.95 - 3.9 mM H_2O, 200-600 mg Ti-MO_x, 313 K) were titrated with a mixture of titrant (1 ml) and DI H_2O (0.85 ml), and the absorbance at 454 nm was measured with a UV-Vis spectrophotometer (Spectronic, 20 Genesys). Corresponding H_2O_2 concentration values were used to calculate H_2O_2 decomposition rates on Ti atoms (the difference between measured rates on Ti-MO_x and the bare support).

3.2.4 *In situ* UV-Vis and Raman Spectroscopy

In situ UV-Vis and Raman spectra of species derived from the activation of H_2O_2 on Ti-MO_x samples were acquired by placing catalyst pellets (30-50 mg) in a custom-built liquid flow cell. Steady-state spectra of the H_2O_2-derived surface species were collected in a solution of H_2O_2 (10 - 50 mM H_2O_2, 39 - 195 mM H_2O, 313 K) in flowing CH_3CN, introduced at 1 cm^3 min^{-1} by an HPLC pump (SSI, LS Class).

Intermediates formed during *in situ* H_2O_2 activation on Ti-MO_x were observed using a Raman spectrometer (Renishaw, InVia) equipped with a 442 nm laser that delivered a power density of 0.8 mW μm^{-2} at the catalyst sample, as measured directly by a power meter (Gentec-EO, PRONTO-Sl). Steady-state spectra were obtained with a long 50X objective and represent the average of 120 scans (12 scans s^{-1}) at a resolution of 2 cm^{-1}. These H_2O_2-derived species were also examined using a fiber-optic UV−vis spectrometer (Avantes, AvaFast 2048) and absorbance features were deconvoluted by performing baseline subtraction and Gaussian peak fittings using OriginPro software.

3.2.5 ^{1}H NMR Spectroscopy

H_2O uptake by MO_x was measured in CH_3CN as the change in [H_2O] in the bulk liquid phase concentration. Solutions of 0.3-0.5 M H_2O in 10 ml CH_3CN were prepared in 20 ml scintillation vials and one 0.5 ml aliquot was collected from each vial before adding 0.25 – 1 g of MO_x to their respective vial. The vials were sirred at 250 rpm, 313 K for 1.5 – 2 h before another aliquot was collected and filtered using a syringe filter (0.05 μm) to separate the solid from the solution. Moles of adsorbed H_2O was calculated from peak areas obtained with a ^{1}H NMR spectrometer (Unity, Inova 500 NB). 100 μL of the CH_3CN and H_2O sample was then mixed with 400 μL of deuterated methanol as solvent and 100 μL of acetone as an internal standard to prepare the NMR sample. The area of the H_2O feature at 4.5 ppm, acetone feature at 2.2 ppm, and the CH_3CN feature at 2.1 ppm were calculated. The quantity of H_2O adsorbed by the solid was calculated from the difference in bulk H_2O concentration before and after contact with the metal oxide.

3.3 Results and Discussion

3.3.1 Effects of Metal Oxide Support on Rates, Selectivities, and Mechanism for Epoxidation

Turnover rates for the epoxidation of 1-hexene with hydrogen peroxide over Ti-MO_x materials depend on the concentrations of 1-hexene ([C_6H_{12}]) and H_2O_2 ([H_2O_2]), because the concentrations of these reactants determine the number of reactive surface intermediates and the concentrations of fluid-phase coreactants during catalysis. Scheme 3.1 depicts the catalytic cycle for 1-hexene epoxidation and hydrogen peroxide decomposition over Ti-MO_x, and this cycle is functionally identical to those for described for styrene,[22, 23] cyclohexene,[23] 1-hexene,[9, 12] 1-octene,[12, 19] and 1-decene[12] epoxidation over Ti-silicate catalysts in prior publications. The mechanism consists of a series of elementary steps that involve quasi-equilibrated adsorption of C_6H_{12} (step 1) and H_2O_2 (step 2). The oxidant, H_2O_2, adsorbs to the Ti center and activates irreversibly to form a pool of Ti-OOH and Ti-(η^2-O_2) surface species that interconvert rapidly by facile proton transfer steps (step 3)[10, 23]. The Ti-OOH intermediates react in the kinetically relevant step either for epoxidation (step 4) or for the decomposition with fluid-phase H_2O_2 (step 6). Quasi-equilibrated desorption of the epoxide produces $C_6H_{12}O$ (step 5). Although step 6 appears as a single elementary step, this process likely involves homolysis of Ti-OOH (or Ti-(η^2-O_2)) and secondary radical reactions that form O_2 and H_2O, as anticipated for Ti-silicates.[80] Subsequently, the active site regenerates.

Turnover rates for alkene epoxidation as a function of the reactant concentrations provide evidence for the elementary steps in Scheme 3.1. Figure 3.2 shows epoxide formation rates normalized by the number of Ti atoms in the reactor. These rates possess a first-order dependence on [C_6H_{12}] and do not depend on [H_2O_2] at low ratios of [C_6H_{12}] to [H_2O_2], which suggests the most abundant reactive intermediate (MARI) derives from H_2O_2 at these conditions. At greater

[C_6H_{12}] to [H_2O_2] ratios, rates exhibit an increasingly weak dependence on [C_6H_{12}] and ultimately become constant. This trend signifies a gradual change in the identity of the MARI from a H_2O_2-derived complex to one formed from 1-hexene – likely 1,2-epoxyhexane. These trends reflect and agree with a previously determined rate expression and mechanism for alkene epoxidation with H_2O_2 over Ti atoms grafted onto SiO_2[23] and incorporated in zeolite BEA.[9, 10] The dependence of turnover rates on reactant concentrations appears consistent for Ti-SiO_2, Ti-ZnO, Ti-GeO_2, and Ti-Al_2O_3 catalysts, and consequently, all these materials likely follow a single mechanism for epoxidation. Yet, turnover rates vary by ~1000-fold among Ti-MO_x, and Ti-SiO_2 provides the greatest rates while Ti-Al_2O_3 gives the lowest.

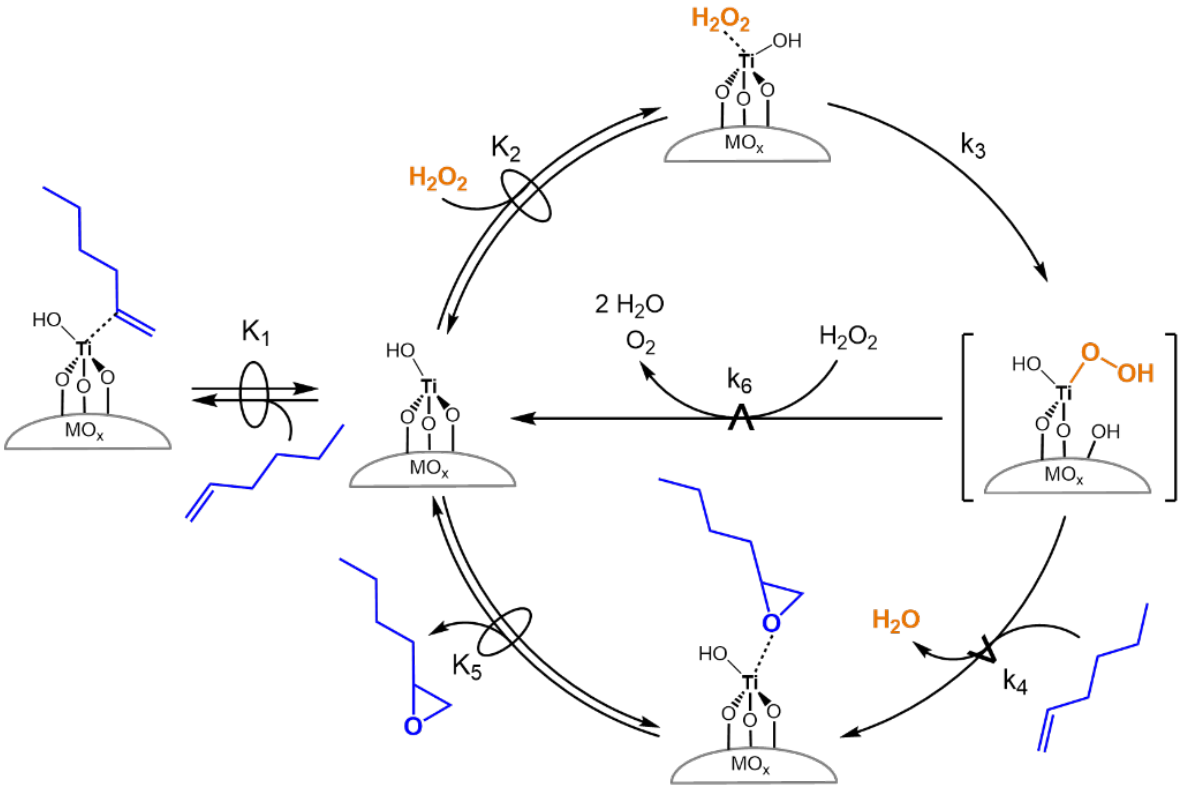

Scheme 3.1. Proposed mechanism for 1-hexene epoxidation with H_2O_2 and H_2O_2 decomposition over Ti-MO_x. The ⇌ symbol denotes a quasi-equilibrated step and the ↛ symbol signifies the kinetically relevant steps for the formation of products. Solvent molecules have been omitted for clarity. Adapted from reference [10].

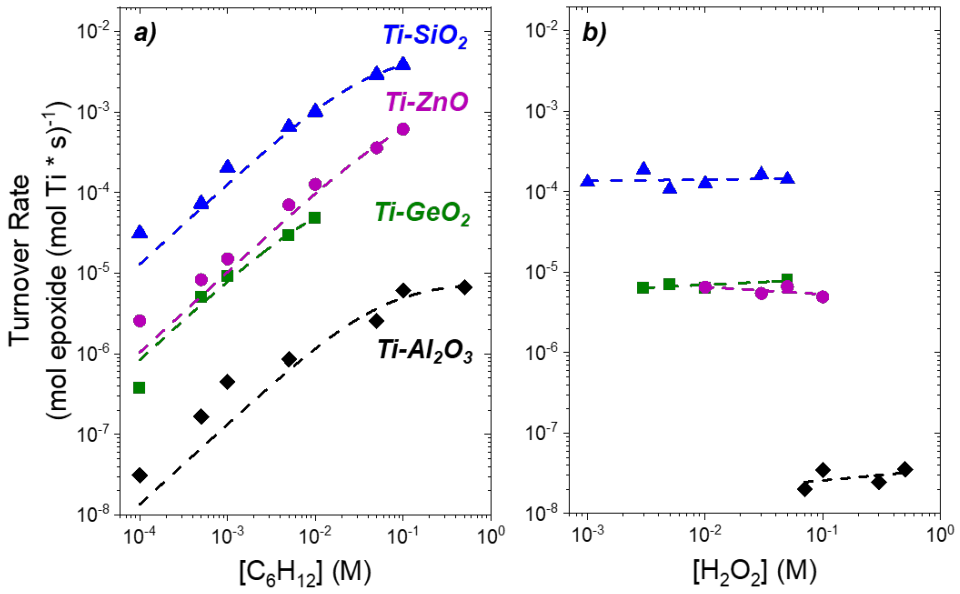

Figure 3.2. Turnover rates for 1-hexene epoxidation with H_2O_2 in CH_3CN over Ti-SiO_2 (blue triangles, 313 K), Ti-ZnO (purple circles, 313 K), Ti-GeO_2 (green squares, 323 K) Ti-Al_2O_3 (black diamonds, 313 K) as functions of (a) [C_6H_{12}] (10 mM H_2O_2, 39 mM H_2O), and (b) [H_2O_2] (0.5 mM C_6H_{12}).

Measured turnover rates for epoxidation reflect the forward rate of step 4 in the sequence of steps shown in Scheme 3.1. Here, the law of mass action predicts epoxidation rates depend linearly on both the number of the reactive Ti-OOH species ($[Ti-OOH]$) and [C_6H_{12}]. Consequently, an expression for the rate of 1-hexene epoxidation (r_E) takes the form:

$$r_E = k_4[Ti-OOH][C_6H_{12}] \tag{3.1}$$

where k_4 represents the rate constant for the kinetically relevant oxygen transfer step (step 4) in Scheme 3.1. Application of the pseudo steady state hypothesis provides a symbolic expression for $[Ti-OOH]$, and the substitution of this expression into Equation 1 makes r_E an explicit function of [H_2O_2] and [C_6H_{12}]. Subsequently, a site balance constrains the sum of the number of all possible adsorbed species to be equal to the total number of active sites ($[L]$). This yields a detailed

rate expression for epoxidation over supported Ti sites consistent with prior studies on related classes of materials.[10, 19, 23, 65]

$$\frac{r_E}{[L]} = \frac{\frac{k_3 k_4 K_2 [H_2O_2][C_6H_{12}]}{k_4[C_6H_{12}]+k_6[H_2O_2]}}{1+K_1[C_6H_{12}]+ K_2[H_2O_2]+\frac{k_3 K_2 [H_2O_2]}{k_4[C_6H_{12}]+k_6[H_2O_2]}+\frac{[C_6H_{12}O]}{K_5}} \quad (3.2)$$

where the denominator is comprised of five terms that represent the numbers of Ti sites that are occupied either by the solvent CH_3CN, C_6H_{12}, H_2O_2, activated forms of H_2O_2 (Ti-OOH or Ti-(η^2-O_2)), and 1,2-epoxyhexane, respectively. Appendix B2.5 shows a complete derivation that leads to Equation 3.2 and the simplified forms described below.

This full expression in Equation 3.2 simplifies considerably when the activated form of H_2O_2 ([*Ti-OOH*]) becomes the MARI.

$$\frac{r_E}{[L]} = k_4[C_6H_{12}] \quad (3.3)$$

Equation 3.3 predicts rates increase linearly with $[C_6H_{12}]$ and do not depend on $[H_2O_2]$, which agrees with the rate measurements in the range of the lowest $[C_6H_{12}]$ in Figure 3.2a. In this regime, turnover rates reflect a single rate constant (k_4), because this single elementary step consumes the most abundant reactive intermediate in the catalytic cycle (Ti-OOH) by reaction with 1-hexene via the kinetically relevant transition state for epoxidation. Ratios of $[C_6H_{12}]$ to $[H_2O_2]$ much greater than unity may cause Ti sites to be saturated by $C_6H_{12}O$, and correspondingly, Equation 3.2 collapses:

$$\frac{r_E}{[L]} = \frac{k_3 k_4 K_2 K_5 [H_2O_2][C_6H_{12}]}{[C_6H_{12}O](k_4[C_6H_{12}]+k_6[H_2O_2])} \quad (3.4)$$

Within this expression, the two groups of variables within the parenthetical portion of the denominator represent the rates of epoxidation (r_4) and H_2O_2 decomposition (r_6). These terms remain because these processes account for the consumption of the Ti-OOH species and appear in the expression for [*Ti-OOH*] given by the pseudo steady state hypothesis. Notably, Equation 3.4 shows that the apparent dependence of turnover rates at $C_6H_{12}O$-saturated sites depends on the relative magnitude of rates for epoxidation and H_2O_2 decomposition. Catalysts with higher selectivities toward epoxidation exhibit greater sensitivities to values of [H_2O_2] while those that preferentially decompose H_2O_2 exhibit epoxidation rates that depend more strongly on [C_6H_{12}].

Overall, comparisons between Figure 3.2 and Equations 3.1 – 3.3 demonstrate that 1-hexene epoxidation with H_2O_2 proceeds upon Ti-atoms supported on SiO_2, ZnO, GeO_2, and Al_2O_3 by the same sequence of elementary steps and involves similar kinetically relevant transition states (Scheme 3.2). The vast differences in turnover rates (factors of 10^3) at identical reaction conditions and with equivalent reactant coverages (Figure 3.2) indicates that the free energies of the reactive surface intermediates (e.g., Ti-OOH) and transition states depend strongly on the identity of the oxide to which Ti-atoms bind.

These differences in turnover rates may reflect variations in the electron affinities of the Ti active sites or the reactive Ti-OOH complexes as proposed by Fang et al. and Tilley et al. that grafted heteroatoms (F, Ge, Sn, Si) to silica supported Ti- or Ta centers by means of a bridging oxygen atoms and achieved 10-50% increases in epoxide selectivity.[18, 84, 108, 113] Such changes may resemble larger differences in rates (10^2-10^5) observed in comparisons between turnover rates of groups 4 - 6 transition metal atoms in the zeolite BEA* framework, which correlated with shifts in adsorption enthalpies for the epoxide product,[9] the LMCT of H_2O_2-derived intermediates, and the enthalpy for CH_3CN adsorption.[10, 23] Yet, other physical differences in the catalyst or the solid-

liquid interface may also bring about these differences in rates. In the next sections, we quantify activation barriers for 1-hexene epoxidation and H_2O_2 decomposition and compare these values to *in situ* spectroscopic observations that report on the electronic structure of the Ti-OOH intermediate and to characteristics of the solid-liquid interfaces formed by these Ti-MO*x* catalysts to deduce how the oxide support affects catalysis.

3.3.2 Activation Enthalpies and Entropies of Ti Sites Saturated with H_2O_2-Derived Intermediates

Scheme 3.2 illustrates the reaction of Ti-OOH with a fluid-phase molecule of 1-hexene to form the transition state for epoxidation, which subsequently evolves to produce the surface bound 1,2-epoxyhexane and water. This process involves charge transfer between Ti-OOH and C_6H_{12} and also requires the displacement and reorganization of solvent molecules near the surface to accommodate a transition state with a steric volume noticeably larger than that of the Ti-OOH intermediate. Apparent activation enthalpies ($\Delta H^{\ddagger}_{epox}$) and entropies ($\Delta S^{\ddagger}_{epox}$) for 1-hexene epoxidation measured at low ratios of [C_6H_{12}] to [H_2O_2], which ensure Ti-OOH is the MARI, reflect the differences between the stability of the epoxidation transition state and Ti-OOH and provide a basis for equitable comparisons among Ti-MO_x catalysts.

Figure 3.3 displays values of $\Delta H^{\ddagger}_{epox}$ and $\Delta S^{\ddagger}_{epox}$ that were calculated from the dependence of turnover rates on reaction temperature in the manner described by Eyring and Polanyi (Figure B7). Values of $\Delta H^{\ddagger}_{epox}$ for Ti-SiO_2 and Ti-GeO_2 are the lowest values, 33 ± 5 and 25 ± 2 kJ mol^{-1}, respectively. Values of $\Delta H^{\ddagger}_{epox}$ on Ti-Al_2O_3 and Ti-ZnO are more than 48 kJ mol^{-1} greater. With the exception of Ti-GeO_2, $\Delta H^{\ddagger}_{epox}$ values correlate with epoxidation turnover rates (Figure 3.2). Similar analysis for hydrogen peroxide decomposition barriers ($\Delta H^{\ddagger}_{decomp}$ and $\Delta S^{\ddagger}_{decomp}$) reveals

that $\Delta H^{\ddagger}_{decomp}$ values are greatest for Ti-SiO_2 and Ti-GeO_2 with somewhat lower values on Ti-Al_2O_3 and Ti-ZnO. For both epoxidation and decomposition reaction pathways, the trends in $\Delta H^{\ddagger}$ correlate with similar variations in $\Delta S^{\ddagger}$, which presumably reflect the reorganization of solvent molecules (CH_3CN and H_2O) caused by the formation of the transition state. Increasingly positive values of $\Delta S^{\ddagger}$ likely signify greater structural reorganization of the solvent near the active site.

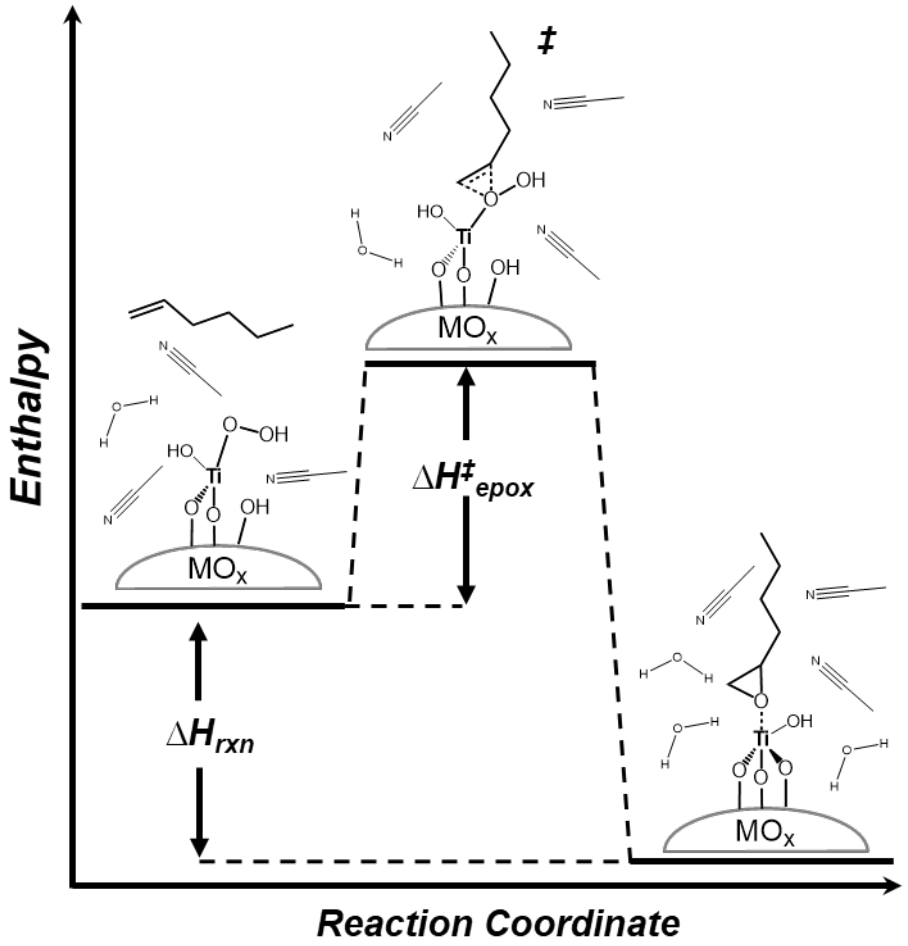

Scheme 3.2. Reaction coordinate diagram for the formation of the transition state for 1-hexene epoxidation by reaction between fluid-phase 1-hexene and Ti-OOH over Ti-MO_x catalysts. The physical states that correspond to the value of $\Delta H^{\ddagger}_{epox}$ and ΔH_{rxn} are depicted.

With the exception of Ti-GeO_2, apparent activation enthalpies for epoxidation correlate with epoxidation turnover rates (Figure 3.2). Furthermore, an increase in $\Delta S^{\ddagger}$ among these catalysts reflects conditions unfavorable for epoxidation, as turnover rates *decrease* with increasing $\Delta S^{\ddagger}$. Entropic changes primarily reflect changes in solvent reorganization near the active site which is especially pronounced in microporous supports (>1 nm pore diameter) that confine molecular transition states.[12, 22] The metal oxide materials used in this study are all mesoporous, therefore, the observed differences in activation entropies ($\Delta\Delta S^{\ddagger}_{epox}$) do not reflect the confinement of solvents and the associated limitations on hydrogen bonding. Consequently, differences in either the electronic structure of Ti active sites and reactive intermediates (inner sphere properties) or differences in solvent composition and organization near the surface (outer sphere interactions) likely cause these changes. To corroborate, we have identified supporting measurements to distinguish between these possibilities.

3.3.3 Electronic Structure of Reactive Intermediates

The differences between turnover rates and $\Delta H^{\ddagger}_{epox}$ values among Ti-MO_x materials may reflect changes in the electronic structure of the reactive Ti-OOH intermediates caused by inductive charge transfer through oxygen atoms that coordinate Ti atoms to the metal oxide surfaces. Differences in the electronic properties of transition metal (Ti, Zr, Hf, Ta, Nb, W) active sites in zeolite BEA influence rates and selectivities for 1-hexene epoxidation with H_2O_2.[9, 10, 23] These differences are explained by changes in electronic properties probed by the measurement of reactive intermediate electrophilicity and functional Lewis acidity of active metal centers. Specifically, when varying the active metal (Ti, Nb, W) and keeping the identity of the silicate or zeolite support constant, the electrophilicity of reactive intermediates (quantified with LMCT energies obtained by *in situ* UV-Vis spectroscopy) and measures of the functional Lewis acid

strength of active metal centers (quantified with measured substrate heats of adsorption) exhibited substantial differences. These differences led to significant changes in both rates and selectivities that favored epoxidation on Ti active sites.

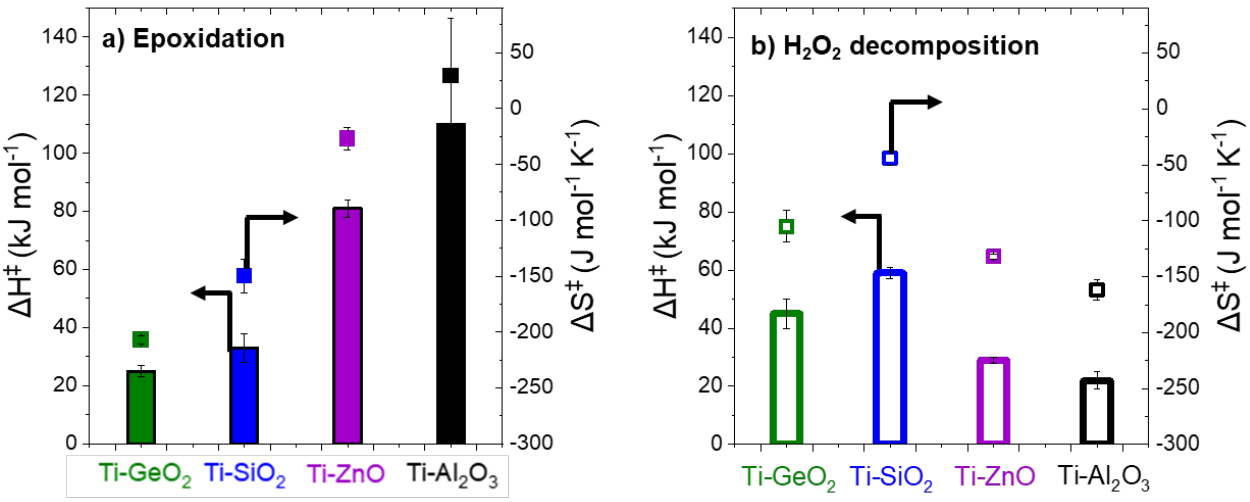

Figure 3.3. Activation enthalpies (bars) and entropies (square symbols) of (a) 1-hexene epoxidation (0.5 mM C_6H_{12}, 10 mM H_2O_2, 39 mM H_2O, 313-333 K), and (b) H_2O_2 decomposition (1 mM H_2O_2, 3.9 mM H_2O, 313-333 K) over Ti-MO_x.

In situ UV-Vis spectra (Figure B5) reveal the presence of reactive oxygen species on Ti-MO_x catalysts and yield values for LMCT energies. Ti-OOH species, which interconvert reversibly with Ti-(η^2-O_2)[74, 125], react with alkenes in the kinetically relevant step for epoxidations that use H_2O_2.[34, 80, 84] Figure 3.4b shows that values for $\Delta H^{\ddagger}_{epox}$ differ significantly despite the similarities between the LMCT energies for these Ti-MO_x materials. Therefore, variations in the electronic structure of these reactive Ti-OOH complexes do not appear responsible for the differences in epoxidation rates and barriers between these materials.

In situ Raman spectra acquired in a similar manner (Figure B6) show the vibrational frequencies for the ν(Ti-(η^2-O_2)) mode of H_2O_2-derived reactive intermediates occurs near 620

cm^{-1}.[9, 72] Variations in the Raman shift for the ν(Ti-(η^2-O_2) signify charge transfer between the peroxo intermediate and the Ti active site that influences bond strengths and reactivity. Figure 3.4a shows the Raman shift for ν(Ti-(η^2-O_2)) on Ti-MO_x catalysts appears to be independent of the support identity (note, results for Ti-GeO_2 are excluded due to a large GeO_2 feature around 630 cm^{-1} which masks the desired Ti-(η^2-O_2) Raman feature).[126, 127] Together, UV-Vis and Raman spectra suggest that H_2O_2-derived reactive species at Ti sites have similar electronic properties despite their coordination to distinct mesoporous metal oxides. Significantly, our prior examinations of alkene epoxidations on Ti, Nb, or W atoms incorporated into the siliceous framework of zeolite BEA demonstrated that $\Delta H^{\ddagger}_{epox}$ values were strong functions of ν(Ti-(η^2-O_2)) and LMCT energies (Figure 3.4, gray symbols).[9] These comparisons strongly suggest that differences in rates and barriers for epoxidation and H_2O_2 decomposition do not result from electronic or inner sphere interactions that influence the reactive Ti-OOH intermediates. These results resemble conclusions from Khodakov et al. during investigation of VO_x supported on Al_2O_3, SiO_2, HfO_2, TiO_2, and ZrO_2 in which they determined that the identity of the support did not intrinsically change turnover rates for oxidative dehydrogenation. Their findings suggested that observed differences in rates originated from differences in the VO_x surface structure, induced by unrecognized variations in surface coverages of V-atoms, and not from electronic interactions with the oxide supports.[128]

3.3.4 Solvent Organization and Composition at the Solid-Liquid Interface

In heterogeneous catalysis, solvent interactions near the solid-liquid interface can have significant impact on the stability of the epoxidation transition state and, therefore, rates and selectivities for this chemistry.[129] Heterogeneous supports in aqueous solutions have been characterized using values to quantify surface charge, specifically, point of zero charge (PZC) and

IEP. [129-131] Metal (hydr)oxides can obtain surface charge by one of two mechanisms: (1) protonation and deprotonation (i.e., PZC) and (2) exchange of anionic and cationic species within solution (i.e., IEP); these values can be measured by acid/base titrations and electrokinetic methods, respectively, to determine the pH or potential at which surface charge is zero.

Differences in covalent or ionic interactions within the reactive intermediate (Ti-OOH) do not appear to be responsible for measured differences in $\Delta H^{\ddagger}_{epox}$ because the values for activation barriers vary widely while spectroscopic probes of reactive species do not reveal significant difference. Consequently, the organization and composition of solvent molecules near the solid-liquid interfaces that contain these active sites may be the origin of differences in epoxidation kinetics. The four mesoporous oxide supports possess different hydroxyl group densities, pK_a values, and proclivities for hydrogen bond donation or acceptance. Figure 3.5 shows that $\Delta H^{\ddagger}_{epox}$ values for Ti-MO_x increase linearly with the median values for the IEP of the MO_x supports.[131] This strong correlation, combined with the indistinguishable differences among the electronic structures of the reactive intermediates, suggests excess contributions that depend upon the spatial distribution and organization of fluid-phase molecules near the surface lead to these changes.

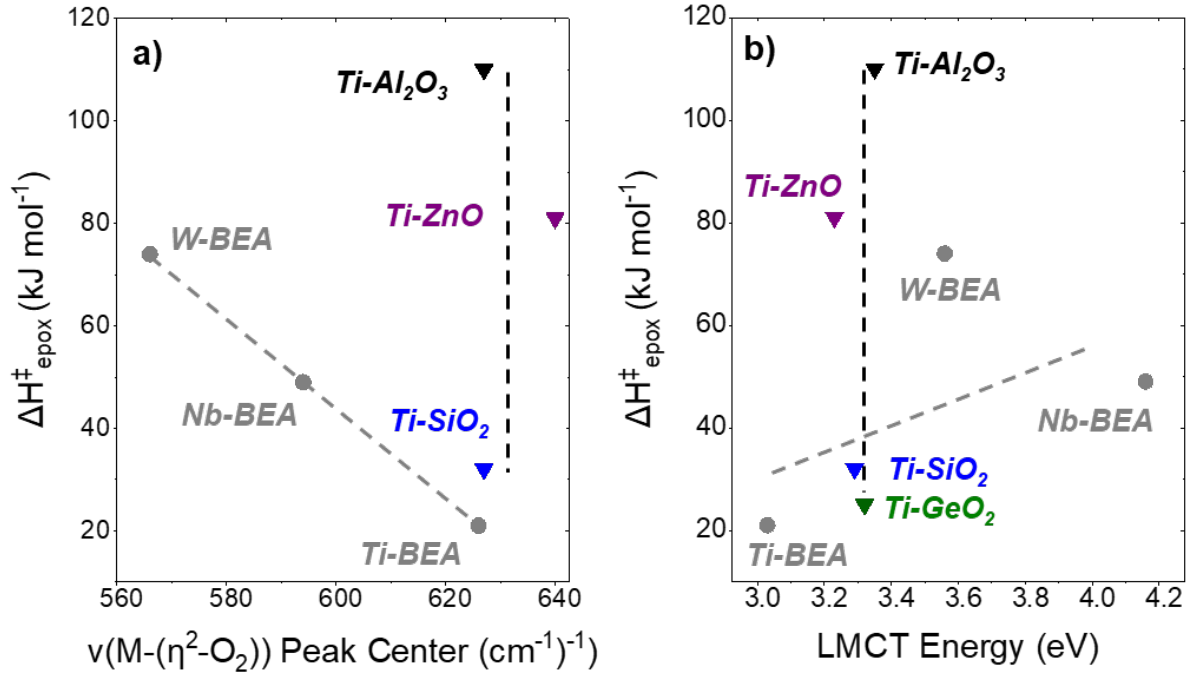

Figure 3.4. Values of $\Delta H^{\ddagger}_{epox}$ obtained on Ti-MOx (triangles, 0.5 mM C_6H_{12}, 10 mM H_2O_2, 39 mM H_2O, 313-333 K) and Ti-BEA, Nb-BEA, and W-BEA catalysts (circles, 0.5 mM H_2O_2 in CH_3CN, 313 K) as functions of (a) vibrational frequencies for the ν(Ti-O_2) mode of Ti-(η^2-O_2) complexes determined by *in situ* Raman spectroscopy, and (b) LMCT energies of Ti-OOH complexes measured by *in situ* UV-Vis spectroscopy. UV-Vis and Raman spectra were acquired in flowing solutions of H_2O_2 (10-50 mM H_2O_2 in CH_3CN, 313 K). Value of $\Delta H^{\ddagger}_{epox}$ for M-BEA catalysts are reproduced from Chapter 2.

Notably, $\Delta H^{\ddagger}_{decomp}$ values do not scale linearly with IEP, which may imply that this relationship emerges for bulkier transition state structures that interact with and displace greater quantities of solvent molecules. These differences in IEP among the metal oxide supports suggest that these surfaces carry different charges during catalysis in aqueous solutions, and therefore, the concentration of water near the surface and the active site may differ and be responsible for the variations in kinetics. As a corollary to this interpretation, changes in solvent composition or the complete elimination of solvent (i.e., conducting the reaction in a gas-phase reactor) may lead to

distinct differences in rates and selectivities among these materials.[11] To test this interpretation further, we determined the uptake of water to the MO_x surfaces within solutions that resemble the solvent for the reaction.

^{1}H NMR Spectroscopy was used to measure water adsorption from the bulk liquid-phase onto the surfaces of metal oxides from solutions similar to those used for catalysis (0.039 M H_2O in CH_3CN, 313 K). Figure 3.6 shows that $\Delta H^{\ddagger}_{epox}$ decrease with a roughly linear dependence on the surface coverage of water (μmol H_2O m^{-2}). GeO_2 demonstrates the greatest water uptake while Al_2O_3 exhibits the least. Greater quantities of water near the surface apparently enthalpically stabilize 1-hexene epoxidation transition states relative to the Ti-OOH reactive intermediates (Scheme 3.2). This trend differs from prior results in microporous Ti-BEA catalysts where greater quantities of water near actives produced a gain in $\Delta H^{\ddagger}_{epox}$, compensated by increasingly positive $\Delta S^{\ddagger}_{epox}$ values, which together resulted in greater turnover rates.[19] These enthalpy–entropy compensation relationships, which reflect physical changes in the organization of solvent molecules, depend strongly on the topology of zeolite catalysts and differ from comparable measurements obtained in bulk solvents (e.g., water).[11, 12 132]

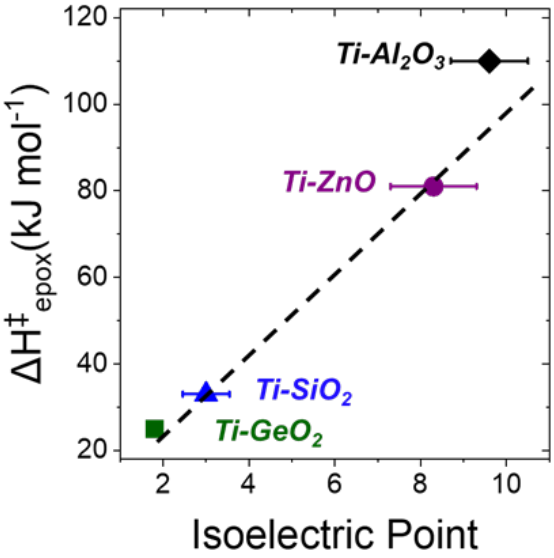

Figure 3.5. Average isoelectric point values for Ti-SiO_2 (blue triangle), Ti-ZnO (purple circle), Ti-GeO_2 (green square), Ti-Al_2O_3 (black diamond) as a function of apparent activation enthalpies for epoxidation $\Delta H^{\ddagger}_{epox}$ (0.5 mM C_6H_{12}, 10 mM H_2O_2, 39 mM H_2O, 313-333 K). [131]

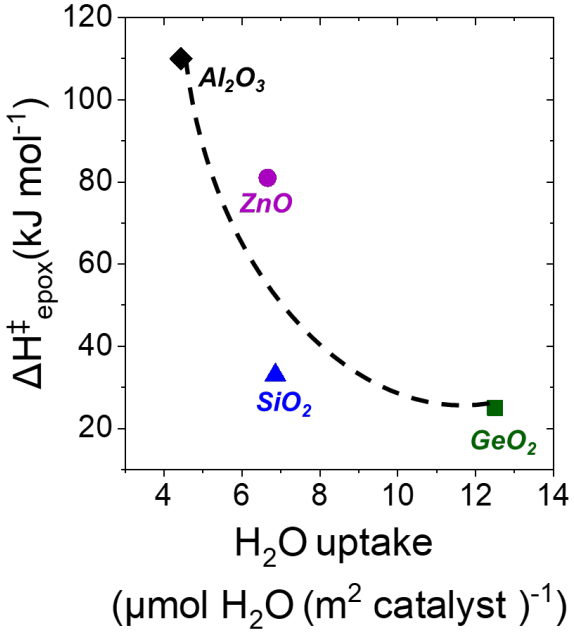

Figure 3.6. H_2O uptake in CH_3CN (0.01 M H_2O in CH_3CN) by bare MO_x at 313 K, 700 RPM.

The interpretation of epoxidation kinetics over Ti-MO_x materials reported here and their correlation to IEP and water uptakes indicate that similar physical processes give rise to the dependence of rates on supports. The directional changes in $\Delta H^{\ddagger}_{epox}$ (i.e., values decrease with increasing water near surfaces) and the relatively larger contributions of $\Delta H^{\ddagger}_{epox}$ values to activation free energies for epoxidation ($\Delta G^{\ddagger}_{epox} = \Delta H^{\ddagger}_{epox} - T\Delta S^{\ddagger}_{epox}$), however, differ from the trends in zeolite micropores. These differences presumably reflect significant changes in the intermolecular interactions that determine solvent organization at these protic interfaces. We hypothesize that interactions between protonated solvent clusters and anionic surfaces (and *vice versa*) may be responsible for the opposing trends.[133] Yet, the precise reasons for the differences remain unclear for now.

3.4 Conclusions

Ti atoms grafted on metal oxide surfaces function as Lewis acid centers that activate H_2O_2 for 1-hexene epoxidation. Rates and selectivities differ among this set of materials across multiple orders of magnitude, and these variations reflect 3-fold differences in $\Delta H^{\ddagger}_{epox}$ values. In situ UV-Vis and Raman spectroscopies were employed to investigate the electronic structure of reactive intermediates. Previous studies report significant changes in the electronic structure of metal centers which correlate differences in activation barriers for epoxidation. However, MOx-supported Ti shows no distinguishable differences be-tween the LMCT energies measured using in situ UV-Vis or in the vibrational structure of reactive surface species (e.g., ν(Ti-(η_2-O_2))) assessed by in situ Raman during H_2O_2 activation. Consequently, the differences in epoxidation kinetics cannot be correlated to changes in electronic structure due to inner sphere effects that impact Ti-OOH and Ti-O_2 intermediates.

Rather, the differences in turnover rates and $\Delta H^{\ddagger}_{epox}$ derive from variations in solvent structure and composition near the catalytic active sites. The structures of the solvent likely change with the surface charge (described by IEP values), which con-tribute additional intermolecular interactions that modify solvent structures and that depend on the composition of the metal oxide. Metal oxide supports with lower IEP values attract great-er quantities of H_2O to the interface, and these differences reduce $\Delta H^{\ddagger}_{epox}$ values. At present, the physical explanation for the differences between correlation of $\Delta H^{\ddagger}_{epox}$ and H_2O composition near active sites, together with comparison to trends observed in Ti-zeolites, indicate that charge separation (e.g., deprotonation of surface hydroxyls) provide orthogonal methods to modify interfacial solvent structures in ways important for catalysis.

CHAPTER 4

EFFECTS OF ALKYL CHAIN LENGTH ON VAPOR-PHASE ALKENE EPOXIDATIONS WITH H_2O_2 OVER TI-BEA[i]

4.1 Introduction

As one of the most prominent building blocks in industry, epoxides are utilized as precursors for a variety of polymers used in the manufacturing of numerous commodity and fine chemicals.[3] Catalysts to support epoxidation reactions with organic oxidants (e.g., tertbutyl-hydroperoxide[15, 43, 60, 134] and cumene hydroperoxide[42, 108]) have been studied for decades. The benchmark heterogeneous catalyst patented by ENIChem in 1983[106, 135] inspired more focus on Ti atoms atoms supported in microporous zeolite frameworks which can efficiently epoxidize propylene using an environment-friendly oxidant, H_2O_2. This discovery has led to the wide-spread use of supported transition metal atoms for highly efficient alkene epoxidation with H_2O_2 in the liquid-phase under mild conditions, as well as a handful of investigations in the vapor-phase. These studies have resulted in several breakthroughs that demonstrate epoxidation rates and selectivities are influenced by transition metal identity, and support additives[136, 137] which closely impact electronic properties of active sites. However, these generally agree on the irreversible activation of H_2O_2 to form the reactive intermediate, Ti-OOH, [6, 8, 14, 138] which is the dominant surface intermediate under many conditions.[9, 23, 139] Therefore, the rates depend strongly on the difference in stability between the hydrogen bonding Ti-OOH intermediate and the larger and more hydrophobic epoxidation transition state that includes the alkyl chain of the alkene substrate. Consequently, interactions

---

i This chapter has been reproduced from the following manuscript:
E. Zeynep Ayla, Ohsung Kwon, and David W. Flaherty, "Effects of Alkyl Chain Length on Vapor phase Epoxidations with H_2O_2 over Ti-BEA", *To be submitted*.

between the reactive species and pore walls in the presence of a solvent influences rates due to differences in excess contributions that modify the stability of the transition state, which results from the alkene interacting with Ti-OOH species.

These excess interactions impact numerous other reactions that occur at solid-liquid interfaces and appear most prevalently during reactions in microporous materials including Bronsted and Lewis acidic zeolites, metal-organic frameworks, and other zeotype materials. The ubiquity of these effects and the magnitude of the corresponding changes in rates and selectivities motivate comparison between kinetics of catalysis at solid-liquid and solid-gas interfaces in microenvironments. Recent studies aim to elucidate the effects of molecular interactions at solid-fluid interfaces for heterogeneous catalytic reactions, focusing on solvent reorganization which influences free energies of catalytic transition states.[11, 12, 20, 140] Di Iorio et al. report that the preferential formation of dimeric hydrogen-bonded butanol networks over extended butanol oligomers in pores of hydrophobic Sn-BEA stabilizes transition states for transfer hydrogenation between 2-butanol and cyclohexanone in these polar environments.[20] In non-polar systems, the presence of condensed fluid-phase alkenes in mesoporous Ni exchanged aluminosilicates (Ni-MCM-41) solvates alkene oligomerization and oligomer desorption transition states and therefore increases rates and suppresses deactivation of these catalysts.[141, 142] Recently, these effects were demonstrated to be absent from Ni exchanged microporous aluminosilicates (e.g., Ni-BEA, Ni-FAU), which was interpreted to show that intraporous density of alkenes was substantially lower in smaller pore materials.[143] Extensive studies by our group report on hydrogen-bonding networks present in solvents comprised of aqueous mixtures of organic solvents (e.g., CH_3CN[12, 30, 132], CH_3OH[132], C_2H_5OH and other n-alcohols[144], γ-butyrolactone[145]) near hydrophilic surfaces.[11] Liu et al. also showed decreasing activity of TS-1 for propylene epoxidation with H_2O_2 with increasing

chain length of protic solvents, which they attribute to decreasing electrophilicity and diffusion limitations.[21] In microporous environments (i.e., zeolite pores) dispersive interactions and networks of hydrogen-bonds between the extended pore structures, intrapore fluid-phase molecules, and reactive intermediates contribute to excess free energies that change apparent enthalpy and entropy barriers for alkene epoxidation reactions with H_2O_2 and modify enthalpies for epoxide adsorption to active sites when catalysts exist within liquid-[12, 102] or vapor[146] phase systems.

These excess free energies depend upon the composition and density of the fluid within the catalyst pores, which depend, in turn, on the topology and polarity of the catalyst pores, but also depend strongly on the structure of the substrate molecules. As a result, turnover rates and selectivities for alkene epoxidation and for epoxide adsorption change with the number of methylene groups (-CH_2-) within the substrate. Bregante et al. demonstrated the increasing sensitivity of solvation with substrate size and chain length and decreasing pore size, all of which correlate with changes in the free energies of liquid-phase epoxidation transition states in meso- and microporous catalysts. They report lower apparent activation barriers for epoxidation when transition states are allowed to access conformations of lower free energy which is made possible with larger pore size, shorter alkyl chains, or smaller (less bulky) oxidants.[102] More specifically, Potts et al. found that turnover rates for liquid-phase epoxidation with aqueous H_2O_2 in CH_3CN varied for linear primary alkenes (C_6-C_{18}) over Ti atoms supported in hydrophilic zeolite BEA pores, because the length of the alkyl chain correlates with the number of hydrogen-bonds that are disrupted and solvent molecules that are displaced from the environment near the active site.[147] Conversely, they found a more narrow correlation with hydrophobic Ti-BEA, which accommodates less solvent and less H_2O, forming less extensive H-bond networks. As a result,

changes in measured $\Delta S^{\ddagger}$ values, which result in significant differences between activation barriers are greater in hydrophilic environments (70 kJ mol^{-1}) rather than within hydrophobic pores (18 kJ mol^{-1}) for this aqueous reaction. Collectively, current studies suggest that factors that lower the free energy of epoxidation transition states depend strongly on solid-solvent-substrate interactions, especially in microporous environments. However, all these prior studies examined reactions within zeolite pores that likely possessed liquid-like densities of solvent molecules. In contrast, reactions performed at higher temperatures and low partial pressures (i.e., activities) of solvent molecules provide an opportunity to reduce the density of intrapore molecules and to determine the impact of dispersive interaction directly between reactive species and pore walls on these same reaction pathways. Hence, vapor-phase studies allow for the decoupling of solvent effects and the extraction of the intrinsic impact of the solvation of reactant and solvent molecules. We recently used this approach to demonstrate that both $\Delta H^{\ddagger}$ and $\Delta S^{\ddagger}$ values for 1-hexene epoxidation in hydrophobic and hydrophilic forms of Ti-BEA increase monotonically with the density of CH_3CN within pores, while the mechanism and identity of the kinetically relevant step remained constant.[146]

Here, we examine the effects of excess thermodynamic contributions on alkene epoxidation with H_2O_2 over Ti-BEA catalysts in the vapor-phase by varying the alkyl chain length (C_3-C_{10}) of straight-chain alkenes. We apply kinetic and spectroscopic methods to probe interactions between solvent and substrate molecules that lead to differences in apparent activation enthalpies ($\Delta H^{\ddagger}$) for epoxidation. Even though turnover rates and apparent activation enthalpies vary 30- and 5-fold, respectively, with increasing alkyl chain length, identification of similar kinetic regimes implies a similar epoxidation mechanism for all alkenes. In situ FTIR shows the displacement of greater amounts of solvent (CH_3CN) molecules with increasing chain length of epoxide that adsorbs

within the zeolite pore. This correlates with measured turnover rates and for alkene epoxidation and $\Delta H^{\ddagger}$. This indicates excess entropic contributions from solvent and substrate molecule reorganize within micropores to accommodate transition state formation. These correlations realize the significance of excess entropic contributions, even with minimal solvent concentrations and facilitate understanding of excess entropic contributions on epoxidation chemistry within micropores.

4.2 Materials and Methods

4.2.1 Catalyst Synthesis and Characterization

Ti-BEA was synthesized by post-synthetically modifying a commercial zeolie BEA support (TOSOH lot No. 94HA6X02Y; Si:Al = 20). This commercial zeolite BEA sample was dealuminated by suspension in HNO_3 (Macron Chemicals, 68-70 wt%) under reflux, to remove Al atoms from the framework, forming $Al(NO_3)$ in the process. The dealuminated BEA was washed with H_2O (17.5 MΩ cm, 60 $cm^3\ g^{-1}$), recovered by vacuum filtration, and then heated treated (823 K, 4 K min^{-1}) in flowing dry air (100 $cm^3\ min^{-1}$; Airgas, Ultra Zero Grade) for 6 h to remove residues from dealumination. Titanium atoms were incorporated into tetrahedral sites in the *BEA framework by introducing $TiCl_4$ (Sigma Aldrich, ≥99.0%), into an opaque, white suspension of dealuminated BEA in dichloromethane (Fisher Chemicals, 20 $cm^3\ g_{zeolite}^{-1}$) and stirring under reflux (313 K) overnight. The white solids were removed from the mixture by rotary evaporation (IKA, RV 10) and heated (823 K, 4 K min^{-1}) under air flow (100 $cm^3\ min^{-1}$; Airgas, Ultra Zero Grade) for 6 h to remove residues (e.g., water, organics) to yield Ti-BEA as a white powder.

An X-ray diffractometer (Siemens-Bruker, D5000), applying Cu Kα radiation, was used to measure the crystallinity of *BEA samples before and after Ti atom incorporation. Powder samples were loaded into a plastic sample holder and resulting diffractograms confirm that the BEA

framework remains intact after dealumination and post-synthetic modification processes (Appendix C1.1, Figure C1).

Elemental analysis to determine Ti content in Ti-BEA samples is performed using energy dispersive X-ray fluorescence. Ti-BEA samples (~50 mg) are finely ground and placed in a 1-cm diameter plastic cup lined with ultralene film and positioned in the He-purged spectrometer (Shimadzu, EDX-7000).The sample is scanned between 0 and 30 keV to reveal fluorescence peaks which correspond to a Ti weight loading of 0.22 wt% (<0.18 atoms (unit cell)$^{-1}$) for the batch of Ti-BEA used in this study (analyzed and calculated by PCEDX Navi software).

The dispersity of Ti atoms on the catalyst surface was measured using a diffuse-reflectance UV-Vis spectrometer (Varian Cary 5G). Ti-BEA samples were mixed and ground with a 1:10 mass ratio of MgO (Sigma Aldrich, 99.99%). Using pure MgO as a background, absorbance spectra was collected and processed to create Tauc plots which compare Kubelka-Munk absorbance values as a function of band gap. We extrapolate the linear portion of these plots to attain a band gap of Ti atoms in *BEA (4.35 eV) which implies the presence of predominantly monomeric Ti species on the catalyst surface (Appendix C1.2, Figure C2).

4.2.2 Gas-phase Epoxidation System

Scheme 4.1 presents a detailed diagram of the gas-phase epoxidation system, which is equipped with a fixed bed reactor, facilities to control the flow rates and partial pressures of reagents, an online gas chromatograph, and an infrared spectrometer (Scheme 4.1).

The tubular fixed bed reactor (McMaster-Carr, Teflon PFA) is enclosed within an insulated (Unitherm, ceramic fiberglass, 1” thick, 13” length, 12” width) and temperature controlled (Watlow PID controller) aluminum clam-shell (3” diameter, 12” length). The outlet of the reactor connects to an online gas chromatograph (Agilent, 7890B with a HP-INNOWAX column) for

product analysis. Liquid reactants (C_6H_{12}, C_8H_{16}, $C_{10}H_{20}$, H_2O_2) and solvent (CH_3CN) are injected through two syringe pumps (KD Scientific, Legato 100; operated by Adagio) in glass syringes (0.5 – 10 ml, Hamilton). A second mass flow controller is used to introduce gaseous reactants (C_3H_6 (Airgas, 5% in He), C_4H_8, (Airgas, 5% in He)) to the system. An atomizer nozzle (Sonaer, NS40K) assists H_2O_2 (1.1-2.6 kPa) vaporization before the oxidant reaches the reactor and catalyst bed. The anhydrous H_2O_2 solution is prepared following a previously published procedure[148] by adding MgO (7 g) into a solution of 1:3 volume ratio of H_2O_2 (Macron Chemicals, 30% in H_2O) to CH_3CN.

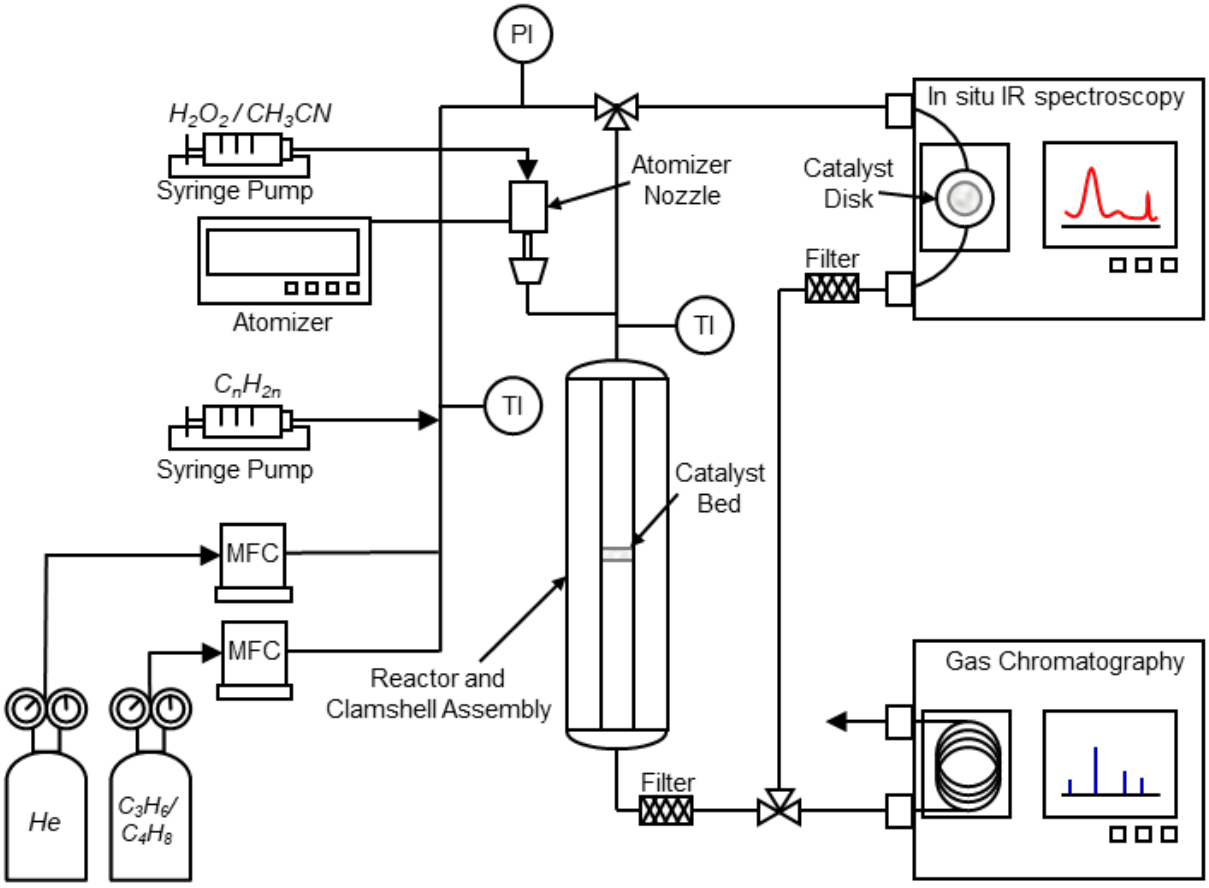

Scheme 4.1. Gas-phase epoxidation flow system includes a temperature-controlled tubular fixed bed reactor, gas chromatographer, and infrared spectrometer. The system is equipped with syringe pumps and mass flow controllers to introduce liquid reactants and gases, respectively. (TI: temperature indicator, PI: pressure indicator, MFC: Mass Flow Controller).

A tee valve upstream of the reactor inlet can divert gas and liquid flow to a transmission cell used in an infrared spectrometer (Bruker, Invenio). Outlet flow from the IR cell is directed to the GC, allowing for operando spectroscopic measurements. He flow (Airgas, Ultra High Purity), controlled by a mass flow controller (Bronkhorst, EL-FLOW; Labview), travels through silicon-coated (SilcoNert) stainless steel lines, heated with silicon rubber heating tapes (Omega), to the packed-bed reactor, the transmission cell for IR spectroscopy, and the gas chromatographer.

4.2.3 Turnover Rate Measurements for Epoxidation

Steady-state turnover rates for alkene epoxidation with H_2O_2 were measured in the gas-phase through the packed-bed reactor loaded with 3-10 mg of Ti-BEA (pelletized to 250-500 μm) supported on glass wool held in place by a glass rod. Epoxidation products were analyzed with gas chromatography (GC). The reactor was operated under conditions to avoid mass transfer effects and at differential conversion of all alkenes (> 8%). Measured rates are normalized by the number of incorporated Ti atoms, of which >94% were shown to be active for epoxidation using *in situ* site titrations in Chapter 1.[9]

4.2.4 *In situ* FTIR Spectroscopy to Observe Solvent Reorganization

An FT-IR spectrometer (Bruker, Invenio) with a HgCdTe detector (filled with liquid N_2) was used to quantify solvent and epoxide density within the catalyst micropores under flowing He. Infrared spectra (1300 – 4000 cm^{-1}, 4 cm^{-1} resolution, 10 kHz, 128 scans) were obtained by placing disk-shaped pellets of Ti-BEA samples (60-70 mg) into a custom-built transmission cell with CaF_2 windows, supported by two stainless steel rings. The cell was heated to and held at 573 K for 2 h with a temperature controller (Watlow, EZ-Zone, 5 $K \cdot min^{-1}$) to desorb any water or residual volatile species. A spectrum of an empty transmission cell without catalyst at the same temperature and He pressure was subtracted as background from all spectra. Acetonitrile (CH_3CN, Fisher

Chemical, HPLC grade, 0-50 kPa) and the epoxide (C_3H_6O (TCI America, >99.0 %), C_4H_8O (TCI America, >99.0 %), $C_6H_{12}O$ (TCI America, > 96.0 %), $C_8H_{16}O$ (TCI America, >96.0 %), $C_{10}H_{20}O$ (TCI America, >97.0 %) were vaporized through injection using two syringe pumps. First, CH_3CN was introduced to the system and allowed to equilibrize before injecting epoxide. Equilibrium absorbance spectra were collected while increasing epoxide partial pressures. The ν(C≡N) feature (2258 and 2296 cm^{-1} to CH_3CN molecules adsorbing to Si-O-Si and $(SiOH)_x$ functions)[19] is normalized by the absorbance areas of the ν(Si-O-Si) overtone stretch (1870 and 1990 cm^{-1})[149] to quantiy CH_3CN coverage per unit cell of Ti-BEA. An extinction coefficient was determined to estimate the amount of CH_3CN and epoxide molecules at varying partial pressures. Calculation of the extinction coefficient and subsequent analysis to determine the number of CH_3CN molecules displaced per unit cell is detailed in Appendix C3.

4.3 Results and Discussion

4.3.1 Selectivity Analysis

Butene and propene oxide form a combination of secondary and tertiary oxidation products like 1,2-propanediol or 1,2-butanediol, propionaldehyde, acetaldehyde, and formaldehyde, all of which form from propene oxide and butene oxide, respectively, as illustrated in Scheme 4.2. Following alkene epoxidation (step 1), the secondary diol product likely forms through hydrolysis as an intermediate (step 2), though quickly reacts to form propionaldehyde, acetaldehyde and/or formaldehyde (step 3), and thus, was not observed with GC.[150] Therefore, all reported turnover rates in this study are the sum of those for the epoxide, and the additional oxidation products reported in Scheme 4.2.

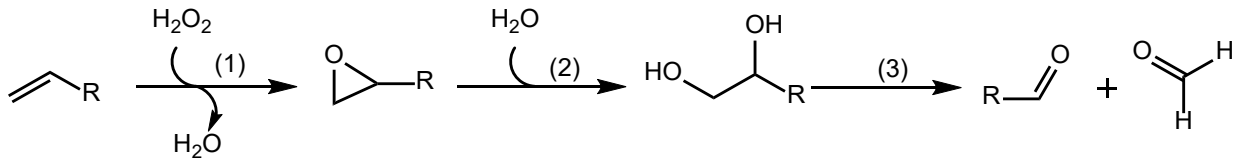

Scheme 4.2. Primary, Secondary, and Tertiary Production of Epoxide, Diol, Acetaldehyde/Propionaldehyde, and Formaldehyde

Conversion, X, values are calculated using Equation 4.1. It should be noted that because diol products are not observed using gas chromatography due to quick reaction to form aldehydes, the term F_{diol} is excluded from the numerator and denominator of Equation 4.1 and is represented by the sum of terms $F_{formaldehyde}$ and $F_{Propionaldehyde}$.

$$X = 100 \bullet \frac{F_{Epoxide}+F_{Acetaldehyde}+F_{Propionaldehyde}}{F_{Alkene}+F_{Epoxide}+F_{Acetaldehyde}+F_{Propionaldehyde}} \quad (4.1)$$

Equation 4.2 generally defines selectivity, S, for oxidation products shows in Scheme 4.1.

$$S = 100 \bullet \frac{F_{Epoxide}+F_{Acetaldehyde}+F_{Propionaldehyde}}{F_{Alkene}+F_{Epoxide}+F_{Acetaldehyde}+F_{Propionaldehyde}} \quad (4.2)$$

4.3.2 Alkene Epoxidation Kinetics and Mechanism

Turnover rates for alkene epoxidation with gaseous H_2O_2 over Ti-BEA depend on the partial pressures of alkene ($[C_nH_{2n}]$) and H_2O_2 ($[H_2O_2]$). Figure 4.1 shows that turnover rates for alkene epoxidation demonstrate a linear dependence on $[C_nH_{2n}]$ at low $[C_nH_{2n}]$:$[H_2O_2]$, which weakens as $[C_nH_{2n}]$:$[H_2O_2]$ increases. Rates are independent of $[H_2O_2]$ at low $[C_nH_{2n}]$:$[H_2O_2]$, which imply a MARI derived from H_2O_2 for all alkenes. Scheme 4.3 illustrates the sequence of elementary steps which are similar to those previously reported in liquid-phase[9, 23, 63, 65] and gas-phase[151] alkene epoxidation studies. The kinetic mechanism involves the quasi-equilibrated adsorption of alkene or H_2O_2 onto Ti sites (steps 1 and 2). H_2O_2 activates upon adsorption to form

Ti-OOH (or Ti-(η^2-O_2)) species, resulting in a broken framework bond (step 3). This reactive oxygen species can dissociate into H_2O by reaction with a nearby water molecule (step 6) or assist in the rate determining oxidation of an alkene molecule close to the active site (step 4). The resulting epoxide desorbs (step 5), regenerating the active Ti center.

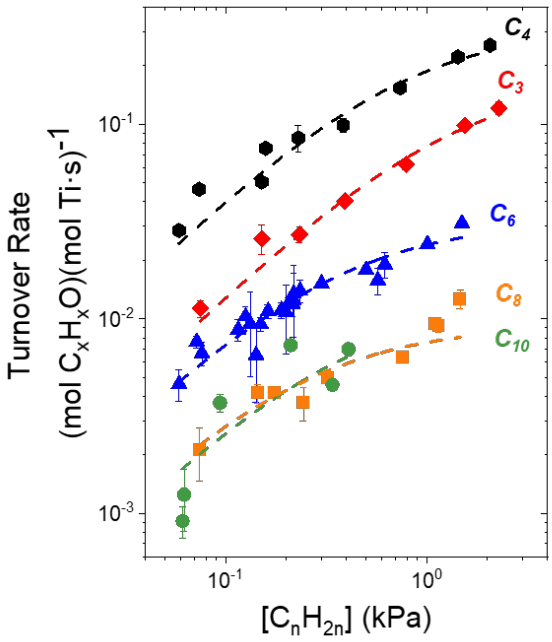

Figure 4.1. Turnover rates over Ti-BEA as functions of (a) [C_nH_{2n}] (1.6 kPa H_2O_2, 10.3 kPa CH_3CN, 383 K in He)

Measured turnover rates for epoxidation represent the forward rate of step 4 in the sequence of steps shown in Scheme 4.2. Here, epoxidation rates depend linearly on both the number of the reactive Ti-OOH species ($[Ti-OOH]$) and [C_nH_{2n}]. Consequently, an expression for the rate of alkene epoxidation (r_E) takes the form:

$$r_E = k_4[Ti-OOH][C_nH_{2n}] \tag{4.3}$$

where k_4 represents the rate constant for the kinetically relevant oxygen transfer step (step 4) in Scheme 4.3. Application of the pseudo steady state hypothesis provides a symbolic expression for

$[Ti-OOH]$, and the substitution of this expression into Equation 4.1 makes r_E an explicit function of [H_2O_2] and [C_nH_{2n}].

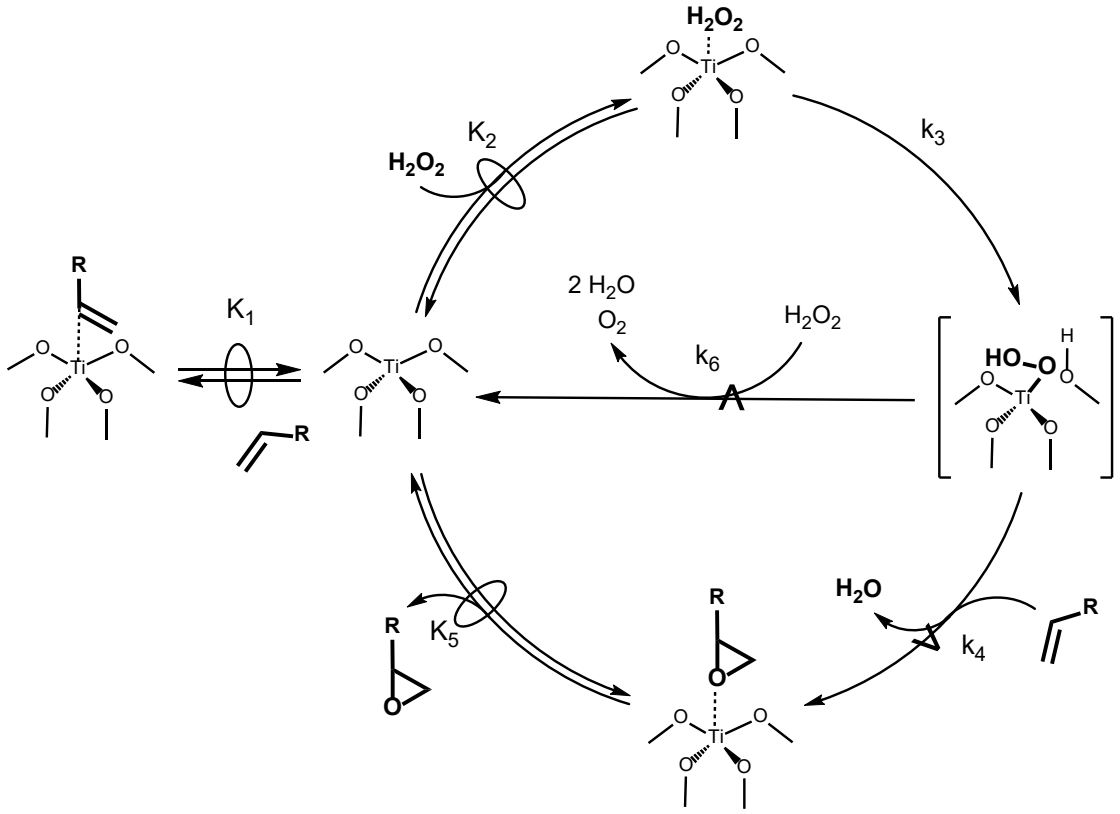

Scheme 4.3. Proposed mechanism for alkene epoxidation with H_2O_2 and H_2O_2 decomposition over Ti-BEA. The ⇌ symbol denotes a quasi-equilibrated step and the ↛ symbol signifies the kinetically relevant steps for the formation of products. Solvent molecules have been omitted for clarity. Adapted from reference [9].

Subsequently, a site balance constrains the sum of the number of all possible adsorbed species to be equal to the total number of active sites ($[L]$). This yields a detailed rate expression for epoxidation over supported Ti sites consistent with prior studies on related materials.[10, 19, 23, 65]

$$\frac{r_E}{[L]} = \frac{\frac{k_3 k_4 K_2 [H_2O_2][C_nH_{2n}]}{k_4[C_nH_{2n}]+k_6[H_2O_2]}}{1+K_1[C_nH_{2n}]+ K_2[H_2O_2]+\frac{k_3 K_2 [H_2O_2]}{k_4[C_nH_{2n}]+k_6[H_2O_2]}+\frac{[C_nH_{2n}O]}{K_5}} \quad (4.4)$$

where the denominator is comprised of five terms that represent the numbers of Ti sites that are occupied either by the solvent CH_3CN, C_nH_{2n}, H_2O_2, activated forms of H_2O_2 (Ti-OOH or Ti-(η^2-O_2)), and epoxide, respectively. Appendix C2.3 shows a complete derivation that leads to Equation 4.4 and the simplified forms described below.

This full expression in Equation 4.4 simplifies considerably when the activated form of H_2O_2 ([*Ti-OOH*]) becomes the MARI.

$$\frac{r_E}{[L]} = k_4[C_nH_{2n}] \tag{4.5}$$

Equation 4.5 predicts rates increase linearly with $[C_nH_{2n}]$ and do not depend on $[H_2O_2]$, which agrees with the rate measurements in the range of the lowest $[C_nH_{2n}]$ in Figure 4.1 and Appendix C2.2. In this regime, turnover rates reflect a single rate constant (k_4), because this single elementary step consumes the most abundant reactive intermediate in the catalytic cycle (Ti-OOH) by reaction with 1-hexene via the kinetically relevant transition state for epoxidation. Ratios of $[C_nH_{2n}]$ to $[H_2O_2]$ much greater than unity may cause Ti sites to be saturated by the epoxide, and correspondingly, Equation 4.4 collapses:

$$\frac{r_E}{[L]} = \frac{k_3k_4K_2K_5\,[H_2O_2][C_nH_{2n}]}{[C_nH_{2n}O](k_4[C_nH_{2n}]+k_6[H_2O_2])} \tag{4.6}$$

Within this expression, the two groups of variables within the parenthetical portion of the denominator represent the rates of epoxidation (r_4) and H_2O_2 decomposition (r_6). These terms remain because these processes account for the consumption of the Ti-OOH species and appear in the expression for [*Ti-OOH*] given by the pseudo steady state hypothesis. Notably, Equation 6 shows that the apparent dependence of turnover rates at $C_nH_{2n}O$-saturated sites depends on the relative magnitude of rates for epoxidation and H_2O_2 decomposition. Catalysts with higher selectivities toward epoxidation exhibit greater sensitivities to values of $[H_2O_2]$ while those that preferentially decompose H_2O_2 exhibit epoxidation rates that depend more strongly on $[C_nH_{2n}]$.

Overall, comparisons between Figure 4.1 and Equations 4.3 – 4.5 demonstrate that C_nH_{2n} epoxidation with H_2O_2 proceeds upon Ti-atoms supported in zeolite BEA by the same series of elementary steps and involves similar kinetically relevant transition states (Scheme 4.3). The differences in turnover rates (~33-fold) at identical reaction conditions and with equivalent reactant coverages (Figure 4.1) indicates that the free energies of the transition states likely depend strongly on the interactions between the solvent, zeolite pore, and increasing reactant alkyl chain length.

4.3.3 Activation Enthalpies and Entropies on Ti sites

Using transition state theory, Equation 4.5 can be redefined in terms of the apparent activation energy for epoxidation ($\Delta G^{\ddagger}_{epox}$) in Equation 4.7.[152]

$$\frac{r}{[L]} = \frac{k_B T}{h} \cdot \exp\left(-\frac{\Delta G^{\ddagger}_{epox}}{RT}\right)[C_nH_{2n}] \tag{4.7}$$

where k_B is the Boltzmann's constant, h is Planck's constant, R is the ideal gas constant, and T is temperature.

Scheme 4.4 depicts the adsorption of a fluid-phase alkene molecule into the zeolite pore and the consequent displacement of solvent molecules. The adsorbed alkene rearranges withing the micropore to react with the active site to form the transition state for epoxidation. The measured apparent activation barriers, $\Delta G^{\ddagger}_{epox}$, represent the difference between the reference state (achieved at low ratios of $[C_nH_{2n}]$ to $[H_2O_2]$) and the transition state. The reaction coordinate suggests that measured $\Delta G^{\ddagger}_{epox}$ includes contributions from the free energies of the transition state ($G^{\ddagger}$), the alkene ($G^{\ddagger}_{alkene}$), and Ti-OOH ($\Delta G_{Ti\text{-}OOH}$).

$$\Delta G^{\ddagger}_{epox} = G^{\ddagger} - G_{alkene} - G_{Ti-OOH} \tag{4.8}$$

Each term in Equation 4.8 reflects deviations from the standard state (G^0) of the component, *i*, and fluctuations due to excess enthalpic (H^{ε}) and excess entropic (S^{ε}) gains or losses.

$$G = G_i^0 + G_i^\varepsilon \tag{4.9}$$

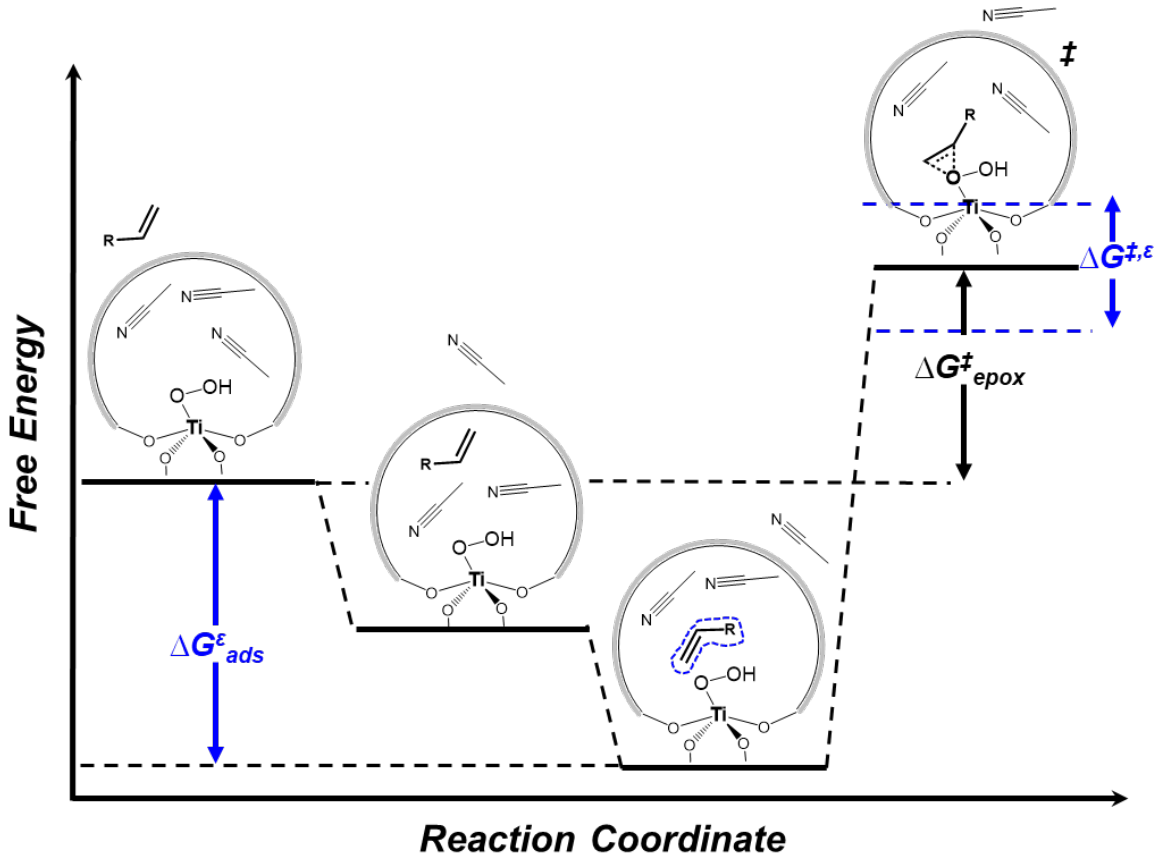

Scheme 4.4. Reaction coordinate diagram for the formation of the transition state for alkene epoxidation over Ti-BEA depicting excess contributions, ΔG^{ε} (blue arrows), from alkene interaction with the solvent and pore environment (adsorption, reorganization, etc.) within the zeolite micropore.

The relationship between measured activation enthalpies ($\Delta H^{\ddagger}$) and entropies ($\Delta S^{\ddagger}$) is depicted as a compensation plot in Figure 4.2a and corresponding values are listed in Table 4.1 for all alkenes. Values of $\Delta H^{\ddagger}$ for longer chain alkenes (C_6-C_{10}) are the lowest (14 - 59 kJ mol^{-1}), while the shorter chain lengths (C_3-C_4) exhibit the highest barriers (94 – 104 kJ mol^{-1}) and greatest turnover rates. Figure 4.2b relates $\Delta H^{\ddagger}$ values to alkyl chain length and shows that apparent activation enthalpies are a nonlinear function of carbon number. Values of $\Delta H^{\ddagger}$ decrease as we

increase chain length for shorter alkenes (C_3-C_6) and increase past a chain length of six carbons. This generally inverse correlation between turnover rates and apparent activation enthalpies and nonlinear relationship between alkyl chain length and $\Delta H^{\ddagger}$ can be explained by trends in excess contributions that influence the free energy of transition state formation[30, 132, 147], depicted in blue in Scheme 4.4.

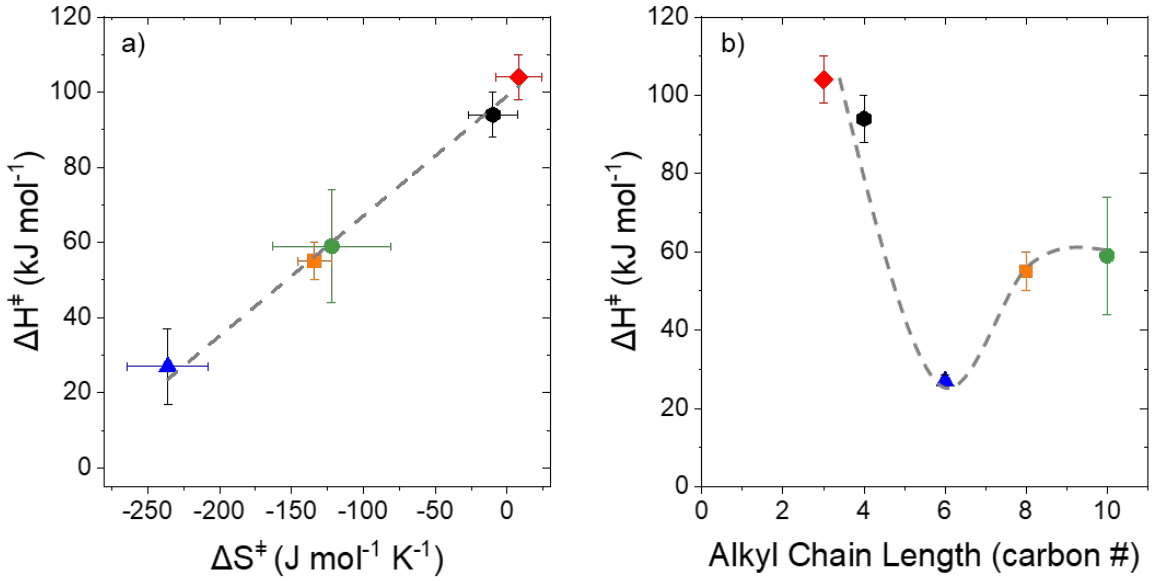

Figure 4.2. Correlation between apparent activation enthalpies ($\Delta H^{\ddagger}$) and (a) apparent activation entropies ($\Delta S^{\ddagger}$) for epoxidation of alkenes over Ti-BEA and (b) alkyl chain length at conditions that results in Ti-OOH MARI and CH_3CN filled pores. C_nH_{2n} epoxidation over Ti-BEA for C_3H_6 (red diamond, 0.13 kPa C_3H_6, 1.6 kPa H_2O_2, 10.3 kPa CH_3CN in He, 373-393 K), C_4H_8 (black hexagon, 0.075 kPa C_4H_8, 1.6 kPa H_2O_2, 10.3 kPa CH_3CN in He, 373-393 K), C_6H_{12} (blue triangle, 0.1 kPa C_6H_{12}, 1.6 kPa H_2O_2, 10.3 kPa CH_3CN in He, 373-393 K), C_8H_{16} (orange square, 0.065 kPa C_8H_{16}, 1.6 kPa H_2O_2, 10.3 kPa CH_3CN in He, 373-393 K), and $C_{10}H_{20}$ (green circle, 0.075 kPa $C_{10}H_{20}$, 1.6 kPa H_2O_2, 10.3 kPa CH_3CN in He, 373-393 K).

Table 4.1. Apparent activation enthalpies ($\Delta H^{\ddagger}_{epox}$) and entropies ($\Delta S^{\ddagger}_{epox}$) for epoxidation

Alkene	$\Delta H^{\ddagger}_{epox}$ (kJ mol^{-1})	$\Delta S^{\ddagger}_{epox}$ (J K^{-1} mol^{-1})
C_3H_6	104 ± 6	8 ± 16
C_4H_8	94 ± 6	-10 ± 17
C_6H_{12}	14 ± 10	-236 ± 28
C_8H_{16}	55 ± 5	-134 ± 12
$C_{10}H_{20}$	59 ± 15	-122 ± 41

Measured values of $\Delta S^{\ddagger}$ presented in Figure 4.2a likely represent the entropic contributions of the epoxidation transition state ($S^{\ddagger}$), the Ti-OOH MARI as the reference state ($\Delta S_{Ti\text{-}OOH}$), gaseous alkene ($\Delta S_{CnH2n,\,g}$), and the amount of acetonitrile molecules that are displaced from the pores of Ti-BEA to form the transition state ($n_{CH3CN} \cdot \Delta S_{CH3CN,\,ads\rightarrow g}$). While the entropy of the reference state, $S_{Ti\text{-}OOH}$,, remains constant for reactions with alkenes of all chain lengths, the changes in entropy during the formation of the transition state, depends on the reactant alkyl chain length. These entropic changes represent excess contributions from solvent displacement and were quantified using in situ FT-IR spectroscopy as described in Section 4.3.4.

4.3.4 *In situ* Infrared Spectroscopy to Probe Solvent Displacement by Epoxide

Solvent is displaced from zeolite pores to accommodate the formation of epoxidation transition states.[12] Here, we use in situ infrared spectroscopy to quantify the amount, $n_{CH3CN,}$ of CH_3CN removed from Ti-BEA micropores upon adsorption of epoxide molecules ($C_nH_{2n}O$), which closely resembles epoxidation transition states (Scheme 4.4). Figure 4.3 shows steady-state spectra of 1,2-epoxydecane (0 - 48 Pa) adsorption in Ti-BEA under constant CH_3CN pressure (10.3 kPa). Acetonitrile features (ν(C≡N), 2258 and 2296 cm^{-1}) represent the adsorption of CH_3CN

on to framework Si-O-Si and $(SiOH)_x$ functions)[19]. The integrated area of the C-H region (2850 – 3020 cm^{-1}) represents the -CH_n- groups of epoxide within the pore. The features of ν(O-H) around 3400 cm^{-1} represent the hydrogen bonding between pore silanols $(SiOH)_x$ and intrapore CH_3CN. The decrease in the intensity of this peak with increasing epoxide pressure indicates that these H-bonds are disrupted as CH_3CN is displaced and removed from the BEA pores. Importantly, the number of disrupted H-bonds will depend on the amount of displaced CH_3CN as well as the alkene chain length, as long chains interact with pore walls to a greater extent. Figure 4.4a shows the relationship between the number of acetonitrile molecules per unit cell of Ti-BEA as a function of epoxide partial pressure ($P_{epoxide}$). As the partial pressure of epoxide increases, the ν(C≡N) feature attenuates, indicating CH_3CN removal from the pores of Ti-BEA, a trend which applies to all studied alkyl chain lengths. The amount of displaced CH_3CN molecules per unit cell generally increases with alkyl chain length (Figure 4.4b). This suggests longer chain length alkenes must displace greater amounts of solvent molecules in order to enter and reorganize while forming the epoxidation transition state within Ti-BEA pores.

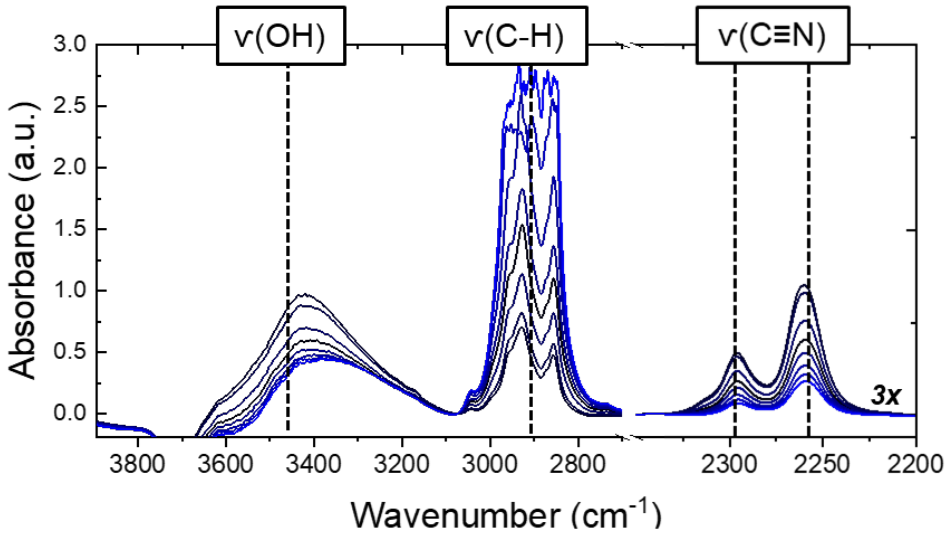

Figure 4.3. Steady-state *in situ* infrared spectra of CH_3CN-saturated (10.3 kPa) Ti-BEA while flowing $C_{10}H_{20}O$ (0 – 48 Pa) in He, 383 K.

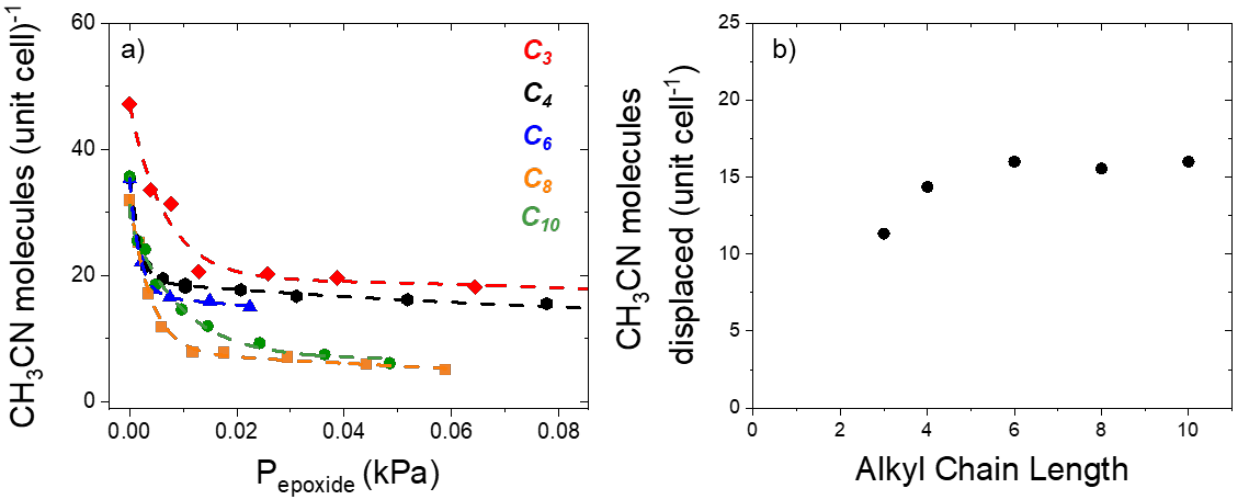

Figure 4.4. (a) Molecules of CH_3CN per unit cell of Ti-BEA (10.3 kPa CH_3CN, 383 K) as a function of epoxide partial pressure (0 – 96 kPa) and (b) molecules of CH_3CN displaced per unit cell of Ti-BEA as a function of alkyl chain length at the same epoxide pressure (3.5 Pa $C_nH_{2n}O$).

The relationships demonstrated in Figure 4.4, correlate with greater values for $n_{CH3CN} \cdot \Delta S_{CH3CN,ads\rightarrow g}$ which represents entropic gain due to solvent displacement and is consistent with the more negative $\Delta S^{\ddagger}$ measured for the epoxidation of longer chain length alkenes. These observations can explain the differences observed in the compensation plot (Figure 4.2) and epoxidation turnover rates (Figure 4.1). Smaller alkenes (propene and butene) displace small amounts of solvent while longer chain alkenes (hexene, octene, and decene) remove increasingly greater amounts of CH_3CN. Together, kinetic measurements of activation barriers and spectroscopic evidence for greater solvent displacement and H-bond disruption with increasing bulkiness of the substrate, reveal excess contributions that influence free energies of transition states and, therefore, turnover rates for epoxidation. These results suggest that performing epoxidation in the vapor-phase offers an opportunity to control solvent pressure and, therefore, the number of solvent molecules in the zeolite pore. This means excess properties can be directly

manipulated in favor of lower activation barriers for the epoxidation of alkenes with varying steric bulk.

4.4 Conclusions

Ti atoms incorporated into the zeolite BEA framework can oxidize alkenes (C_3H_6, C_4H_8, C_6H_{12}, C_8H_{16}, $C_{10}H_{20}$) with H_2O_2 in the vapor-phase. The epoxidation mechanism remains the same with increasing chain length, however, turnover rates and apparent activation enthalpies vary 33- and 7-fold, respectively, among all alkenes under similar surface coverages. These differences are likely a result of the outer-sphere interactions that involve solvent reorganization during the formation of the epoxidation transition state. Reactant alkyl chain length controls excess entropic interactions which influence apparent activation barriers for the formation of the epoxidation transition state. Here, we probe these interactions with *in situ* IR spectroscopy by quantifying solvent displacement as a function of alkyl chain length. Steady-state infrared spectra show increasing epoxide pressure leads to decreasing amounts of intrapore CH_3CN and H-bonding between solvent molecules and silanol groups within the micropores of Ti-BEA. The number of molecules of displaced CH_3CN correlates with alkyl chain length and $\Delta S^{\ddagger}$ for epoxidation and explains the observed differences in epoxidation turnover rates among the alkenes. These relationships provide a methodical approach to identify and deconvolute excess contributions that make up outer-sphere interactions and impact oxidation reactions in microporous catalytic environments.

CHAPTER 5

CONCLUSIONS AND FUTURE DIRECTIONS

5.1 Conclusions

Epoxidation with hydrogen peroxide is an important chemistry for creating polymer building blocks used in surfactants, solvents, and advanced materials. Groups 4 – 6 metals supported on microporous zeolites and non-porous metal oxides catalyze epoxidation with H_2O_2, where turnover rates and selectivities vary with the functional Lewis acid strength of the active site, acidity of the support in aqueous environments, and alkyl chain length of substrates. This dissertation reports on the influence of inner- and outer-sphere interactions on liquid- and vapor-phase alkene epoxidations with H_2O_2 over transition metal-incorporated zeolites and disperse Ti atoms on metal oxides. Modifying the elemental identity of the transition metal active site (Ti, Nb, W) in zeolite BEA affects the electrophilicity of reactive oxygen intermediates because of varying inner-sphere interactions leading to differences in energy barriers for the formation of the epoxidation transition state. On the other hand, when modifying the metal oxide support (SiO_2, Al_2O_3, ZnO, GeO_2) for Ti atom active centers, the covalent bonding structure at the active site (inner sphere) is preserved, while changing surface acidity causes variations in solvent structure (outer sphere) near the active site, resulting in differences in the epoxidation transition state free energy. Moreover, increasing alkene chain length for reaction in the confined micropores of zeolite BEA contributes to variations in solvent restructuring (outer-sphere) that occur to accommodate different transition states conformations due to steric interactions. These variations in active site electron affinity, metal oxide support acidity, and alkyl chain length lead to differences in rates and selectivities, as a result of thermodynamic contributions that determine the free energy of the

epoxidation transition state, and therefore, the measured activation enthalpies and entropies for these reactions.

Chapter 2 details the effects of differences in covalent bonding structure (inner-sphere interactions) on 1-hexene epoxidation with H_2O_2 over transition metal atoms incorporated into the zeolite BEA framework. We synthesized groups 4 – 6 (Ti, Nb, W) framework-substituted BEA through post-synthetic modification to study 1-hexene epoxidation with H_2O_2. Epoxidation turnover rates (5 mM 1-hexene, 10 mM H_2O_2, 313 K) are 250- and 60-fold lower on W-BEA and Nb-BEA than Ti-BEA, respectively. Epoxide selectivities (defined as epoxidation rates divided by total H_2O_2 consumption rates) at comparable conditions are greatest on Ti-BEA (93%), followed by Nb- (38%) and W-BEA (20%). These large differences in catalysis are not due to differences in the epoxidation mechanism or the coverage of reactive intermediates, which are functionally equivalent for these materials. Rather, the disparity in rates and selectivities reflect differences in the electrophilicity of the reactive metal-hydroperoxo and peroxo intermediates, which are inferred through measurements of apparent activation enthalpies ($\Delta H^{\ddagger}$). The heats of 1,2-epoxyhexane adsorption (ΔH_{Ads}) onto active sites measured by isothermal titration calorimetry, show W-BEA binds 1,2-epoxyhexane less strongly than Ti- and Nb-BEA. Values of $\Delta H^{\ddagger}$ decrease linearly with ΔH_{Ads}, showing that alkene epoxidation exhibits a strong linear free energy relationship. Collectively, these findings reveal a rare case in catalysis where both rates and selectivities can be improved through design principles that increase the functional Lewis acid strength of the active site for alkene epoxidation.

Chapter 3 aims to more closely examine solid-liquid interactions which constitute outer-sphere properties and provide evidence that the chemical identity of metal oxide supports predominantly impact intermolecular interactions and the composition of the solvent present near

solid-liquid interfaces for 1-hexene epoxidation with H_2O_2. We grafted Ti atoms onto inert metal oxide supports (SiO_2, γ-Al_2O_3, ZnO, GeO_2) with similar Ti densities and observe as much as 1000-fold differences in epoxidation turnover rates (1 mM 1-hexene, 10 mM H_2O_2, 313-323 K). Kinetic analysis confirms consistent epoxidation mechanism for all Ti-MO_x catalysts. In situ Raman and UV-Vis spectroscopy studies suggest that all Ti-MO_x activate H_2O_2 to form the same pool of reactive intermediates (Ti-OOH and Ti-(η^2-O_2)) with similar electronic structures. These results indicate that the identity of support has no effect on the epoxidation mechanism or the covalent interactions in supported active metal atoms and reactive oxygen species, ruling out inner-sphere effects as an explanation for the over 4-fold differences in apparent activation enthalpies ($\Delta H^{\ddagger}$). Instead, support properties that affect outer-sphere interactions offer an explanation for the observed differences in turnover rates and activation energies. The isoelectric point quantifies the acidity of the support and correlations with $\Delta H^{\ddagger}$ and H_2O uptake by the metal oxide (measured with NMR spectroscopy) signify that more acidic supports allow for greater water agglomeration near the surface (and active site), decreasing apparent activation enthalpies for epoxidation.

Chapter 4 investigates outer-sphere interactions that influence apparent activation barriers for vapor-phase alkene epoxidation with H_2O_2 over Ti-BEA in the absence of bulk solvent. Kinetic analysis indicates all alkenes follow the same epoxidation mechanism over Ti-BEA but demonstrate as much as 33-fold and 7-fold differences in turnover rates and apparent activation enthalpies, respectively. This study explores the excess enthalpic and entropic contributions that determine transition state free energies of catalytic reaction by increasing the alkyl chain length of the substrate for reaction in zeolite micropores. *In situ* infrared spectra examine the amount of displaced CH_3CN, disrupted hydrogen bonding, and adsorbed epoxide simultaneously to develop relationships between entropic gains/losses and bulkiness of the substrate. Greater ratios of CH_3CN

molecules are displaced and larger amounts of hydrogen bonding between Si-OH and CH_3CN are disrupted as alkene chain length increase, providing strong evidence for the type of outer-sphere interactions that impact free energies for reactions that occur within confined zeolite pores.

Altogether, this dissertation develops methods to deconvolute thermodynamic contributions that originate from inner- and outer-sphere interactions at or near active sites for alkene epoxidations with H_2O_2 over supported transition metal atoms. The applied kinetic, spectroscopic, and calorimetric techniques can be further employed to better understand and improve the design of solid catalysts for industrially-relevant chemistry.

5.2 Future Directions

5.2.1 Exploring Energy Barriers for Enantioselective Pathways for Allyl Alcohol Epoxidation with H_2O_2 and TBHP over Supported Transition Metal Catalysts with Various Chiral Ligands

Enantioselectivity is essential for the pharmaceutical industry where racemic mixtures find little use since specific enantiomers have distinct biological functions.[153] Approaches for achieving enantiopure (ee > 99 %) compounds include enantiomer separations, enantioselective syntheses, chiral pooling (using chiral building blocks derived from natural products) and enantioselective catalysis. Enantioselective catalysis has the potential to offer a relatively inexpensive, reproducible, and environment-friendly approach to transform prochiral compounds to desired enantiopure products. However, the development of enantioselective catalysts is limited by the availability of natural, biologically relevant substrates.[154]. Over the years, the development of enantioselective homogeneous metal complexes has been the most successful in attaining high stereo- or regio-selectivity, winning several Nobel Prizes in 2001 for asymmetric hydrogenation by Noyori and Knowles and enantioselective oxidation by Sharpless et al.[155] Chiral epoxides are

synthetic precursors for several biologically active compounds, including (S)-timolol, which is an andrenergic blocking agent used in antiarrhythmic drugs and (R)-(-)-mevalonolactone, which is broadly used in cellular regulation.[156]

The well-known Sharpless reaction employs homogeneous Ti-isopropoxide complexes to catalyze the asymmetric epoxidation of primary allylic alcohols in the presence of chiral diethyl tartrate ligands, *tert*-butyl hydroperoxide, and molecular sieves.[134] While progress for heterogeneous enantioselective catalysts has been slower, Basset and colleagues have adapted the Sharpless active site for heterogeneous application.[157, 158] Silica-supported Ta metal centers are prepared for enantioselective synthesis by the addition of chiral ligands ((+)-diisopropyl tartrate, (-)-diisopropyl tartrate) for asymmetric epoxidation of 2-propen-1-ol and *trans*-2-hexen-1-ol.[158] The limited availability and high cost of chiral ligands restricts the number and scope of catalytic studies. Because the enantiopurity (ee) is generally high for these catalysts (83-96 %), the goal is to reduce activation barriers for the reaction to increase turnover rates and prove the efficacy of H_2O_2 instead of *tert*-butyl hydroperoxide to minimize organic waste. In order to efficiently select the appropriate chiral ligand for supported active sites, it is helpful to examine the changing electronic or excess molecular interactions near the transition metal active sites. Preliminary experiments for this project have been conducted to achieve successful analysis of enantiomer mixtures by gas chromatography and work continues to determine epoxidation kinetics, mechanism, and reactive intermediates over group 5 metals supported on silica. The characterization of supported chiral environments can lead to the development of parameters to control enantioselectivity through chiral ligand identity, reaction solvent, and support interactions.

Group 5 transition metals (Ta, Nb) supported on silica (M-SiO_2) were synthesized following the grafting procedure used in Chapter 3 (Section 3.2.1) targeting a metal loading of 0.5 wt %. The

SiO_2 support (Davisil Grade 646, 35-60 mesh, pore size 150 Å, Sigma-Aldrich) was heated to 823 K (4 K min^{-1}) in flowing air (100 cm^3 min^{-1}, Airgas, Ultra Zero Grade) for 6 h to desorb any water and minimize loss of surface area or rearrangements during the synthesis procedure. The dried SiO_2 was placed in a round bottom flask attached to a Schlenk line under under vacuum (< 5 Pa) and heated to 473 K in an oil bath to remove remaining moisture, before the addition of $CHCl_3$ (Fisher Chemicals, 20 cm^3 g_{MOx}^{-1}) under Ar purge at ambient temperature. The metal precursor ($TaCl_4[C_5(CH_3)_5]$, 98% Strem Chemicals; $NbCl_2(C_{10}H_{10})$ 95% Sigma-Aldrich) was added to this slurry and allowed to stir for ~30 minutes. In order to facilitate deprotonation of the SiO_2 surface for the metal complexes to bind, triethylamine (Et_3N) was added at a molar ratio of Et_3N to metal precursor equal to 3. The addition of Et_3N produces HCl, indicated by the formation of a white vapor, signifying successful grafting of the metal precursors. After the mixture is stirred (~12 h) at room temperature, the solvent is removed by rotary evaporation (IKA, RV 10). The remaining solids are heat treated (823 K, 4 K min^{-1}) in air (100 cm^3 min^{-1}, Airgas, Ultra Zero Grade) for 6 h to yield the M-SiO_2 catalysts, which are white powders. Catalyst characterization will require EDXRF and DRUVS analysis to confirm metal loading and dispersity, respectively, as accomplished in Chapter 2 (Section 2.2.2) and Chapter 3 (Section 3.2.2).

Liquid-phase batch reactions were prepared to measure the trans-2-hexen-1-ol (96%, Sigma-Aldrich) epoxidation turnover rates with *tert*-butyl hydroperoxide (TBHP, 5.0-6.0 M in decane, Sigma Aldrich) over Ta- and Nb-SiO_2 catalysts, with and without the presence of a chiral ligand ((+)-diisopropyl tartrate (DIPT); 98%, ee:99%, Sigma-Aldrich). The catalyst (~500 mg Ta- or Nb-SiO_2) was allowed to stir in a solution of 0.1 M trans-2-hexen-1-ol, DIPT (1.5 molar ratio), and 3 ul benzene as an internal standard, in 30 ml dichloromethane (>99.5%, Fisher Chemicals) for ~30 min at 263 K (Isotemp chiller, Fisher Scientific) in a 150 ml jacketed glass reactor

(Chemglass) to allow the DIPT to titrate the Ta sites. After the collection of an initial aliquot using syringe with an attached polypropylene filter (Tisch Scientific, 0.05 μm), the oxidant was added (0.1 M TBHP) to start the reaction. Subsequent aliquots were collected at various time intervals and the products were examined using a gas chromatograph (Agilent 5890) equipped with a liquid autosampler and chiral column (Cyclosil-B, method described in Appendix D1.2). Preliminary results show very low conversion over Ta- and Nb-SiO_2 catalysts (~1% after 24 h, and ee%: 0) with and without the addition of DIPT. Enantioselective chromatography was achieved by studying the same reaction over the homogeneous Sharpless catalyst, Ti-isopropoxide (Appendix D). Future work will focus on improving conversion by increasing metal content on support, lowering temperature (253 K) and increasing reaction time (48 h) to more closely replicate conditions used by Basset and colleagues.[158]

Once enantioselective kinetics are observed over the supported group 5 metal catalysts, spectroscopic and calorimetric analysis can provide further characterization of the chiral active site environments. First, *in situ* UV-Vis spectra on these surfaces will assess ligand-to-metal transfer energies of Ta-OOH or Ta-(η^2-O_2) species to identify conditions (e.g., choice of oxidant and chiral ligands) in which a more electrophilic reactive intermediate is present, as preferred to oxidize the electron rich C=C bonds in alkenes. Next, isothermal titration calorimetry (ITC, Chapter 2, Section 2.2.5) can be used to titrate supported Ta or Nb atoms with chiral epoxide molecules to measure epoxide adsorption enthalpies, essentially reproducing the structure of epoxidation transition states to determine their relative stabilities, likely correlating with transition state free energies ($\Delta G^{\ddagger}_{epox}$), since stronger adsorption (lower $\Delta H_{ads,epox}$) implies more stable transition states. As established in **Chapters 2-4**, elemental identity of active metal, surrounding solvent molecules, and inherent support properties influence active site environments. Using *in*

situ UV-Vis and ITC to determine reactive intermediate electrophilicity and values for $\Delta H_{ads,epox}$ on supported metal sites titrated with chiral ligands, respectively, we can identify conditions to maximize the stability of transition states for desired chiral epoxidation reactions.

5.2.2 Investigation of Inner Sphere Interactions in Supported Metal Nanoparticles for One-pot Synthesis of H_2O_2 and Epoxidation of Propylene

While the Hydrogen Peroxide Propylene Oxide (HPPO) process presents a "green" route to propylene oxide production, yielding water as the only byproduct and circumventing the production of organic waste, the production of the oxidant is not so environment-friendly. Hydrogen peroxide is currently industrially produced via the anthraquinone auto-oxidation process.[159] The process is highly complex and energy-intensive, requiring several purification steps and excessive waste generation. Moreover, the safe transportation and storage of H_2O_2 can add to the current high costs of producing it.

Recent work by several groups have made progress in using gold supported on titania or titanosilicate (TS-1) zeolite supports to produce propylene oxide in the vapor-phase with H_2/O_2 mixtures.[160, 161] Haruta and coworkers were able to achieve high selectivity (>99 %) for the epoxidation of propylene over Au/TiO_2 catalysts.[160] Even though propylene conversion is low (around 1 % or less), they report that the gold incorporation method is essential to achieving high epoxide selectivity and favor deposition-precipitation over impregnation, because the former produces homogeneously dispersed gold particles with a narrow size distribution (3-5 nm). Delgass et al. improved on this observation with several publications providing evidence for improved epoxidation rates over small Au nanoparticles (2-5 nm) that are uniformly disperse and accessible by Ti sites in titanosilicalite pores.[162, 163] Following these discoveries, other metals and promoters were considered to improve the in situ generation of hydrogen peroxide.[164, 165] Au-

Pd/TiO_2-SiO_2 catalyst pellets coated with a TS-1 membrane and Pt promoted Pd/TS-1 catalysts were reported by Jin et al. and Meiers et al. to show increased yield and conversion when compared to Au/TiO_2 prepared by Haruta and colleagues.[165, 166] Lee and colleagues demonstrated that strong interaction between Cs promoters and Au in Au/TS-1 systems help stabilize small gold clusters inside the micropores of TS-1.[167] Furthermore, Lu et al. show that promoters such as K, Cs, Mg, Ca, and Ba can improve Au deposition and enhance rates by effecting the isoelectric point of the support.[168] Despite these improvements, the nature of the electronic and molecular interactions within these catalytic systems remains unclear and may impede its further advancement and industrial application.

This one-pot reaction requires the presence of two distinct types of active sites: one for the synthesis of H_2O_2 from H_2 and O_2, and another for the epoxidation of propylene, in close proximity to each other. Generally, the role of the gold or similar metallic species (Pt, Pd, Ag) is to form hydrogen peroxide from H_2 and O_2, which is then transferred to Ti sites where activates to form the Ti-hydroperoxo species active for propylene epoxidation, or undesired hydrogenation to propane (Scheme 5.1).[164]

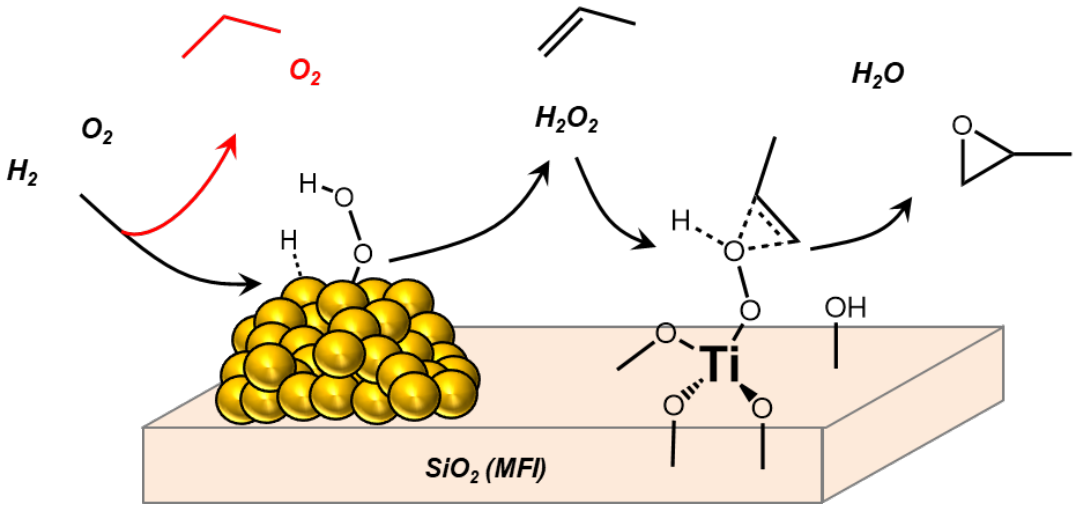

Scheme 5.1. Propylene epoxidation and hydrogenation with H_2/O_2 over Au/TS-1.

Varying the chemical identity of the promoters can alter the electronic environment of the nearby reactive intermediates for propylene epoxidation, affecting rates and selectivities. To study the effects of inner-sphere properties on reaction, we will synthesize Au nanoparticles supported in TS-1 zeolites using the deposition-precipitation method to achieve 0.3-1% Au loading and nanoparticles sizes between 3-5 nm.[160] Moreover, promoters like Cs, Mg, Ca, Br, or K, can be introduced through impregnation with inorganic salts.[169] Metal loading can be determined using EXDRF, MFI framework crystallinity using XRD, and Au nanoparticle size using transmission electron microscopy (TEM). Steady-state propylene epoxidation turnover rates can be measured by utilizing the vapor-phase epoxidation system introduced in **Chapter 4**. The catalyst is loaded into a temperature-controlled reactor through which C_3H_6, H_2, and O_2 pressures are controlled using mass flow controllers and organic products are quantified using gas chromatography. Epoxidation turnover over rates and mechanism can be determined for Au/TS-1 with and without various promoters. Finally, we can quantify the changes in inner sphere-interactions at the epoxidation active site (Ti-SiO_2 in TS-1) that occur when the elemental identity of the promoter is varied using the *in situ* UV-Vis and Raman spectroscopic techniques introduced in **Chapters 2 and 3**. Specifically, Au/TS-1 pellets impregnated with promoters will be examined under H_2O_2 flow as described in Chapter 2 (Section 2.2.4). *In situ* UV-Vis spectroscopy will be used to measure the ligand-to-metal charge transfer of Ti-OOH intermediates in the presence of various promoters. Similarly, in the presence of different promoters, *in situ* Raman spectroscopy will examine the Raman shift of Ti-(η^2-O_2) features. The measured values of ligand-to-metal charge transfer energies and Raman shift can provide evidence for the electrophilicity of the Ti-OOH or the charge density surrounding the Ti-(η^2-O_2) reactive intermediates that form upon H_2O_2 activation, respectively. We expect the measured differences, if any, will correlate with turnover rates and

activation enthalpies for propylene epoxidation. These results can offer strategies to systematically modify electronic interactions near the active site in favor of higher turnover rates and selectivity for propylene epoxidation.

REFERENCES

1. Fernandes, E. Propylene Oxide Market 2022.

2. Wood, L. Global Ethylene Oxide Market - Forecasts from 2021 to 2026 2022.

3. Oyama, S. T., *Mechanisms in Homogeneous and Heterogeneous Epoxidation Catalysis*. Elsevier: 2008; p 528.

4. Baer, H. B., Massimo; Forlin, Anna; Pottenger, Lynn H.; Lindner, Joerg, Propylene Oxide. In *Ullmann's Encyclopedia of Industrial Chemistry*, 2012.

5. Meng, Y. T., Francesco; Freites Aguilera, Adriana; Cai, Xiaoshuang; Russo, Vincenzo; Tolvanen, Pasi; Leveneur, Sébastien The Lord of the Chemical Rings: Catalytic Synthesis of Important Industrial Epoxide Compounds. *Catalysts* **2021,** *11*.

6. Russo, V.; Tesser, R.; Santacesaria, E.; Di Serio, M., Chemical and Technical Aspects of Propene Oxide Production via Hydrogen Peroxide (HPPO Process). *Industrial & Engineering Chemistry Research* **2013,** *52* (3), 1168-1178.

7. Guarino, B., The 'extremely flammable' chemical behind the fire in the flooded Texas plant. *The Washington Post* 2017.

8. Bassler, P. G., H. G.; Weidenbach, M., The New HPPO Process for Propylene Oxide: From Joint Development to Worldscale Production. *Chemical Engineering Transactions* **2010,** *21*, 571-576.

9. Ayla, E. Z.; Potts, D. S.; Bregante, D. T.; Flaherty, D. W., Alkene Epoxidations with H2O2 over Groups 4–6 Metal-Substituted BEA Zeolites: Reactive Intermediates, Reaction Pathways, and Linear Free-Energy Relationships. *ACS Catalysis* **2021,** *11* (1), 139-154.

10. Bregante, D. T.; Flaherty, D. W., Periodic Trends in Olefin Epoxidation over Group IV and V Framework-Substituted Zeolite Catalysts: A Kinetic and Spectroscopic Study. *Journal of the American Chemical Society* **2017,** *139* (20), 6888-6898.

11. Potts, D. S.; Bregante, D. T.; Adams, J. S.; Torres, C.; Flaherty, D. W., Influence of solvent structure and hydrogen bonding on catalysis at solid–liquid interfaces. *Chemical Society Reviews* **2021**.

12. Bregante, D. T.; Chan, M. C.; Tan, J. Z.; Ayla, E. Z.; Nicholas, C. P.; Shukla, D.; Flaherty, D. W., The shape of water in zeolites and its impact on epoxidation catalysis. *Nature Catalysis* **2021,** *4* (9), 797-808.

13. Thornburg, N. E.; Thompson, A. B.; Notestein, J. M., Periodic Trends in Highly Dispersed Groups IV and V Supported Metal Oxide Catalysts for Alkene Epoxidation with H2O2. *ACS Catalysis* **2015,** *5* (9), 5077-5088.

14. Kholdeeva, O. A.; Ivanchikova, I. D.; Maksimchuk, N. V.; Skobelev, I. Y., H2O2-based selective epoxidations: Nb-silicates versus Ti-silicates. *Catalysis Today* **2019,** *333*, 63-70.

15. Mimoun, H., Do metal peroxides as homolytic and heterolytic oxidative reagents. Mechanism of the halcon epoxidation process. *Catalysis Today* **1987,** *1* (3), 281-295.

16. Arcoria, A.; Ballistreri, F. P.; Tomaselli, G. A.; Di Furia, F.; Modena, G., Opposite regioselectivity in the epoxidation of geraniol and linalool with molybdenum and tungsten peroxo complexes. *Journal of Organic Chemistry* **1986,** *51* (12), 2374-2376.

17. Thomas, J. M. S., Gopinathan; Klunduk, Marek C.; Attfield, Martin P.; Maschmeyer, Thomas; Johnson, Brian F. G.; Bell, Robert G., The Identity in Atomic Structure and Performance of Active Sites in Heterogeneous and Homogeneous, Titanium−Silica Epoxidation Catalysts. *The Journal of Physical Chemistry B* **1999,** *103* (42), 8809-8813.

18. Cordeiro, P. J.; Tilley, T. D., Enhancement of Epoxidation Efficiencies for Ta-SBA15 Catalysts. The Influence of Modification with –EMe 3 (E = Si, Ge, Sn) Groups. *Langmuir* **2011,** *27* (10), 6295-6304.

19. Bregante, D. T.; Johnson, A. M.; Patel, A. Y.; Ayla, E. Z.; Cordon, M. J.; Bukowski, B. C.; Greeley, J.; Gounder, R.; Flaherty, D. W., Cooperative Effects between Hydrophilic Pores and Solvents: Catalytic Consequences of Hydrogen Bonding on Alkene Epoxidation in Zeolites. *Journal of the American Chemical Society* **2019,** *141* (18), 7302-7319.

20. Di Iorio, J. R.; Johnson, B. A.; Román-Leshkov, Y., Ordered Hydrogen-Bonded Alcohol Networks Confined in Lewis Acid Zeolites Accelerate Transfer Hydrogenation Turnover Rates. *Journal of the American Chemical Society* **2020,** *142* (45), 19379-19392.

21. Liu, X.; Wang, X.; Guo, X.; Li, G., Effect of solvent on the propylene epoxidation over TS-1 catalyst. *Catalysis Today* **2004,** *93-95*, 505-509.

22. Bregante, D. T.; Tan, J. Z.; Sutrisno, A.; Flaherty, D. W., Heteroatom substituted zeolite FAU with ultralow Al contents for liquid-phase oxidation catalysis. *Catalysis Science & Technology* **2020,** *10* (3), 635-647.

23. Bregante, D. T.; Thornburg, N. E.; Notestein, J. M.; Flaherty, D. W., Consequences of Confinement for Alkene Epoxidation with Hydrogen Peroxide on Highly Dispersed Group 4 and 5 Metal Oxide Catalysts. *ACS Catalysis* **2018,** *8* (4), 2995-3010.

24. Corma, A.; Navarro, M. T.; Pariente, J. P. R., Synthesis of an ultralarge pore titanium silicate isomorphous to MCM-41 and its application as a catalyst for selective oxidation of hydrocarbons. *Journal of the Chemical Society, Chemical Communications* **1994,** (2), 147.

25. Aigner, M.; Grosso-Giordano, N. A.; Okrut, A.; Zones, S.; Katz, A., Epoxidation of 1-octene under harsh tail-end conditions in a flow reactor I: a comparative study of crystalline vs. amorphous catalysts. *Reaction Chemistry & Engineering* **2017,** *2* (6), 842-851.

26. Wu, P.; Tatsumi, T.; Komatsu, T.; Yashima, T., A Novel Titanosilicate with MWW Structure: II. Catalytic Properties in the Selective Oxidation of Alkenes. *Journal of Catalysis* **2001,** *202* (2), 245-255.

27. Riedel, D. H. T., Joaquim; Wegerle, Ulrike; Parvulescu, Andrei-Nicolae; Schroeder, Alexander; Spiske, Luise; Urbanczyk, Daniel; Mueller, Ulrich; Witzl, Werner; Weidenbach, Meinolf. Process for preparing propylene oxide. U.S. Patent 9,738,616 B2, 2017.

28. Nijhuis, T. A.; Makkee, M.; Moulijn, J. A.; Weckhuysen, B. M., The Production of Propene Oxide: Catalytic Processes and Recent Developments. *Industrial & Engineering Chemistry Research* **2006,** *45* (10), 3447-3459.

29. Nijhuis, T. A.; Huizinga, B. J.; Makkee, M.; Moulijn, J. A., Direct Epoxidation of Propene Using Gold Dispersed on TS-1 and Other Titanium-Containing Supports. *Industrial & Engineering Chemistry Fundamentals* **1999,** *38* (3), 884-891.

30. Bregante, D. T.; Flaherty, D. W., Impact of Specific Interactions Among Reactive Surface Intermediates and Confined Water on Epoxidation Catalysis and Adsorption in Lewis Acid Zeolites. *ACS Catalysis* **2019**, 10951-10962.

31. Thornburg, N. E.; Nauert, S. L.; Thompson, A. B.; Notestein, J. M., Synthesis–Structure–Function Relationships of Silica-Supported Niobium(V) Catalysts for Alkene Epoxidation with H2O2. *ACS Catalysis* **2016,** *6* (9), 6124-6134.

32. Joergensen, K. A., Transition-metal-catalyzed epoxidations. *Chemical Reviews* **1989,** *89* (3), 431-458.

33. Notestein, J. M.; Iglesia, E.; Katz, A., Grafted Metallocalixarenes as Single-Site Surface Organometallic Catalysts. *Journal of the American Chemical Society* **2004,** *126* (50), 16478-16486.

34. Ivanchikova, I. D.; Skobelev, I. Y.; Maksimchuk, N. V.; Paukshtis, E. A.; Shashkov, M. V.; Kholdeeva, O. A., Toward understanding the unusual reactivity of mesoporous niobium silicates in epoxidation of C C bonds with hydrogen peroxide. *Journal of Catalysis* **2017,** *356*, 85-99.

35. Corma, A.; Fornes, V.; Pergher, S. B.; Maesen, T. L. M.; Buglass, J. G., Delaminated zeolite precursors as selective acidic catalysts. *Nature* **1998,** *396* (6709), 353-356.

36. Antonova, N. S.; Carbó, J. J.; Kortz, U.; Kholdeeva, O. A.; Poblet, J. M., Mechanistic Insights into Alkene Epoxidation with H_2O_2 by Ti- and other TM-Containing Polyoxometalates: Role of the Metal Nature and Coordination Environment. *Journal of the American Chemical Society* **2010,** *132* (21), 7488-7497.

37. Jiménez-Lozano, P.; Skobelev, I. Y.; Kholdeeva, O. A.; Poblet, J. M.; Carbó, J. J., Alkene Epoxidation Catalyzed by Ti-Containing Polyoxometalates: Unprecedented β-Oxygen Transfer Mechanism. *Inorganic Chemistry* **2016,** *55* (12), 6080-6084.

38. Maksimchuk, N. V.; Ivanchikova, I. D.; Maksimov, G. M.; Eltsov, I. V.; Evtushok, V. Y.; Kholdeeva, O. A.; Lebbie, D.; Errington, R. J.; Solé-Daura, A.; Poblet, J. M.; Carbó, J. J., Why Does Nb(V) Show Higher Heterolytic Pathway Selectivity Than Ti(IV) in Epoxidation with H2O2? Answers from Model Studies on Nb- and Ti-Substituted Lindqvist Tungstates. *ACS Catalysis* **2019**, 6262-6275.

39. Maksimchuk, N. V.; Maksimov, G. M.; Evtushok, V. Y.; Ivanchikova, I. D.; Chesalov, Y. A.; Maksimovskaya, R. I.; Kholdeeva, O. A.; Solé-Daura, A.; Poblet, J. M.; Carbó, J. J., Relevance of Protons in Heterolytic Activation of H2O2over Nb(V): Insights from Model Studies on Nb-Substituted Polyoxometalates. *ACS Catalysis* **2018,** *8* (10), 9722-9737.

40. Boronat, M.; Corma, A.; Renz, M.; Viruela, P. M., Predicting the Activity of Single Isolated Lewis Acid Sites in Solid Catalysts. *Chemistry - A European Journal* **2006,** *12* (27), 7067-7077.

41. Oxtoby, D. W. G., H.P.; Campion, A. , *Principles of Modern Chemistry*. 7th ed.; Cengage Learning: 2012.

42. Sheldon, R. A., Synthetic and mechanistic aspects of metal-catalysed epoxidations with hydroperoxides. *Journal of Molecular Catalysis* **1980,** *7* (1), 107-126.

43. Sheldon, R., Metal-catalyzed epoxidation of olefins with organic hydroperoxides I. A comparison of various metal catalysts. *Journal of Catalysis* **1973,** *31* (3), 427-437.

44. Buijink, J. K. F.; Van Vlaanderen, J. J. M.; Crocker, M.; Niele, F. G. M., Propylene epoxidation over titanium-on-silica catalyst—the heart of the SMPO process. *Catalysis Today* **2004,** *93-95*, 199-204.

45. Chiusoli, G. P., Maitlis, P. M., *Metal-catalysis in Industrial Organic Processes*. Royal Society of Chemistry: 2006.

46. Amini, M.; Haghdoost, M. M.; Bagherzadeh, M., Monomeric and dimeric oxido–peroxido tungsten(VI) complexes in catalytic and stoichiometric epoxidation. *Coordination Chemistry Reviews* **2014,** *268*, 83-100.

47. Mimoun, H., The role of peroxymetallation in selective oxidative processes. *Journal of Molecular Catalysis* **1980,** *7* (1), 1-29.

48. Mimoun, H.; Seree De Roch, I.; Sajus, L., Epoxydation des olefines par les complexes peroxydiques covalents du molybdene—VI. *Tetrahedron* **1970,** *26* (1), 37-50.

49. Di Furia, F.; Modena, G., Mechanism of oxygen transfer from peroxo species. **1982,** *54* (10).

50. Shen, Y.; Jiang, P.; Zhang, J.; Bian, G.; Zhang, P.; Dong, Y.; Zhang, W., Highly dispersed molybdenum incorporated hollow mesoporous silica spheres as an efficient catalyst on epoxidation of olefins. *Molecular Catalysis* **2017,** *433*, 212-223.

51. Kuwahara, Y.; Furuichi, N.; Seki, H.; Yamashita, H., One-pot synthesis of molybdenum oxide nanoparticles encapsulated in hollow silica spheres: an efficient and reusable catalyst for epoxidation of olefins. *Journal of Materials Chemistry A* **2017,** *5* (35), 18518-18526.

52. Barrio, L.; Campos-Martín, J. M.; De Frutos, M. P.; Fierro, J. L. G., Alkene Epoxidation with Ethylbenzene Hydroperoxides Using Molybdenum Heterogeneous Catalysts. *Industrial & Engineering Chemistry Research* **2008,** *47* (21), 8016-8024.

53. Prasetyoko, D.; Fansuri, H.; Ramli, Z.; Endud, S.; Nur, H., Tungsten Oxides-Containing Titanium Silicalite for Liquid Phase Epoxidation of 1-octene with Aqueous Hydrogen Peroxide. *Catalysis Letters* **2009,** *128* (1-2), 177-182.

54. Gelbard, G.; Gauducheau, T.; Vidal, E.; Parvulescu, V. I.; Crosman, A.; Pop, V. M., Epoxidation with peroxotungstic acid immobilised onto silica-grafted phosphoramides. *Journal of Molecular Catalysis A: Chemical* **2002,** *182-183*, 257-266.

55. Maheswari, R.; Pachamuthu, M. P.; Ramanathan, A.; Subramaniam, B., Synthesis, Characterization, and Epoxidation Activity of Tungsten-Incorporated SBA-16 (W-SBA-16). *Industrial & Engineering Chemistry Research* **2014,** *53* (49), 18833-18839.

56. Hammond, C.; Straus, J.; Righettoni, M.; Pratsinis, S. E.; Hermans, I., Nanoparticulate Tungsten Oxide for Catalytic Epoxidations. *ACS Catalysis* **2013,** *3* (3), 321-327.

57. Yan, W.; Ramanathan, A.; Ghanta, M.; Subramaniam, B., Towards highly selective ethylene epoxidation catalysts using hydrogen peroxide and tungsten- or niobium-incorporated mesoporous silicate (KIT-6). *Catal. Sci. Technol.* **2014,** *4* (12), 4433-4439.

58. Morales-Delarosa, S.; Campos-Martin, J. M.; Terreros, P.; Fierro, J. L. G., Catalytic Epoxidation of Cyclohexene with Tert-butylhydroperoxide Using an Immobilized Molybdenum Catalyst. *Topics in Catalysis* **2015,** *58* (4-6), 325-333.

59. Mizuno, N.; Yamaguchi, K.; Kamata, K., Epoxidation of olefins with hydrogen peroxide catalyzed by polyoxometalates. *Coordination Chemistry Reviews* **2005,** *249* (17-18), 1944-1956.

60. Kurusu, Y.; Masuyama, Y.; Saito, M.; Saito, S., Epoxidation with t-butyl hydroperoxide in the presence of molybdenum peroxide and polymer-immobilized molybdenum peroxide. *Journal of Molecular Catalysis* **1986,** *37* (2-3), 235-241.

61. Ross-Medgaarden, E. I.; Wachs, I. E., Structural Determination of Bulk and Surface Tungsten Oxides with UV−vis Diffuse Reflectance Spectroscopy and Raman Spectroscopy. *The Journal of Physical Chemistry C* **2007,** *111* (41), 15089-15099.

62. Lwin, S.; Li, Y.; Frenkel, A. I.; Wachs, I. E., Nature of WOx Sites on SiO2 and Their Molecular Structure–Reactivity/Selectivity Relationships for Propylene Metathesis. *ACS Catalysis* **2016,** *6* (5), 3061-3071.

63. Bregante, D. T.; Priyadarshini, P.; Flaherty, D. W., Kinetic and spectroscopic evidence for reaction pathways and intermediates for olefin epoxidation on Nb in *BEA. *Journal of Catalysis* **2017,** *348*, 75-89.

64. Tauc, J. M., A. , States in the Gap. *J. Non-Cryst. Solids* **1972**, 569–585.

65. Bregante, D. T.; Patel, A. Y.; Johnson, A. M.; Flaherty, D. W., Catalytic thiophene oxidation by groups 4 and 5 framework-substituted zeolites with hydrogen peroxide: Mechanistic and spectroscopic evidence for the effects of metal Lewis acidity and solvent Lewis basicity. *Journal of Catalysis* **2018,** *364*, 415-425.

66. Madon, R. J.; Boudart, M., Experimental criterion for the absence of artifacts in the measurement of rates of heterogeneous catalytic reactions. *Industrial & Engineering Chemistry Fundamentals* **1982,** *21* (4), 438-447.

67. Eaton, T. R.; Boston, A. M.; Thompson, A. B.; Gray, K. A.; Notestein, J. M., Counting Active Sites on Titanium Oxide-Silica Catalysts for Hydrogen Peroxide Activation through In Situ Poisoning with Phenylphosphonic Acid. *ChemCatChem* **2014,** *6* (11), 3215-3222.

68. Groves, J. T.; Nemo, T. E.; Myers, R. S., Hydroxylation and epoxidation catalyzed by iron-porphine complexes. Oxygen transfer from iodosylbenzene. *Journal of the American Chemical Society* **1979,** *101* (4), 1032-1033.

69. Tosheva, L.; Mihailova, B.; Valtchev, V.; Sterte, J., Zeolite beta spheres. *Microporous and Mesoporous Materials* **2001,** *48* (1-3), 31-37.

70. Neelakantan, P., Raman spectrum of acetonitrile. *Proceedings of the Indian Academy of Sciences - Section A* **1964,** *60* (6), 422-424.

71. Mihailova, B.; Valtchev, V.; Mintova, S.; Faust, A. C.; Petkov, N.; Bein, T., Interlayer stacking disorder in zeolite beta family: a Raman spectroscopic study. *Physical Chemistry Chemical Physics* **2005,** *7* (14), 2756.

72. Bordiga, S.; Damin, A.; Bonino, F.; Ricchiardi, G.; Lamberti, C.; Zecchina, A., The Structure of the Peroxo Species in the TS-1 Catalyst as Investigated by Resonant Raman Spectroscopy. *Angewandte Chemie International Edition* **2002,** *41* (24), 4734-4737.

73. Maniatakou, A.; Karaliota, S.; Mavri, M.; Raptopoulou, C.; Terzis, A.; Karaliota, A., Synthesis, characterization and crystal structure of novel mononuclear peroxotungsten(VI) complexes. Insulinomimetic activity of W(VI) and Nb(V) peroxo complexes. *Journal of Inorganic Biochemistry* **2009,** *103* (5), 859-868.

74. A. Zecchinaa , S. B., G. Spotoa, A. Damina, G. Berliera, F. Boninoa, C. Prestipinoaand C. Lamberti, In situ characterization of catalysts active in partial oxidations: TS-1 and Fe-MFI case studies. *Topics in Catalysis* **2002,** *21*, 67-78.

75. Bonino, F.; Damin, A.; Ricchiardi, G.; Ricci, M.; Spanò, G.; D'Aloisio, R.; Zecchina, A.; Lamberti, C.; Prestipino, C.; Bordiga, S., Ti-Peroxo Species in the TS-1/H2O2/H2O System. *The Journal of Physical Chemistry B* **2004,** *108* (11), 3573-3583.

76. Colomban, P. G., G. , Raman Scattering Theory and Elements of Raman Instrumentation. In *Raman Spectroscopy for Soft Matter Applications*, Amer, M. S., Ed. John Wiley & Sons, Inc.: 2009.

77. Hu, H.; Wachs, I. E.; Bare, S. R., Surface Structures of Supported Molybdenum Oxide Catalysts: Characterization by Raman and Mo L3-Edge XANES. *The Journal of Physical Chemistry* **1995,** *99* (27), 10897-10910.

78. Dengel, A. C.; Griffith, W. P.; Powell, R. D.; Skapski, A. C., Studies on transition-metal peroxo complexes. Part 7. Molybdenum(VI) and tungsten(VI) carboxylato peroxo complexes, and the X-ray crystal structure of $K_2[MoO(O_2)_2(glyc)]2H_2O$. *Journal of the Chemical Society, Dalton Transactions* **1987,** (5), 991.

79. Kholdeeva, O. A., Selective Oxidations Catalyzed by Mesoporous Metal Silicates. In *Liquid Phase Oxidation via Heterogeneous Catalysis: Organic Synthesis and Industrial Applications*, Clerici, M. G. K., O.A., Ed. John Wiley & Sons, Inc.: 2013; p 127.

80. Yoon, C. W.; Hirsekorn, K. F.; Neidig, M. L.; Yang, X.; Tilley, T. D., Mechanism of the Decomposition of Aqueous Hydrogen Peroxide over Heterogeneous TiSBA15 and TS-1 Selective Oxidation Catalysts: Insights from Spectroscopic and Density Functional Theory Studies. *ACS Catalysis* **2011,** *1* (12), 1665-1678.

81. Maurya, M. R., Bharti, N., Synthesis, thermal and spectral studies of oxoperoxo and dioxo complexes of vanadium(V), molybdenum(VI) and tungsten(VI) with 2-(a-hydroxyalkyl/aryl)benzimidazole. *Transition Metal Chemistry* **1999,** (24), 389-393.

82. Carati, A.; Flego, C.; Previde Massara, E.; Millini, R.; Carluccio, L.; Parker, W. O.; Bellussi, G., Stability of Ti in MFI and Beta structures: a comparative study. **1999,** *30* (1), 137-144.

83. Marchese, L.; Maschmeyer, T.; Gianotti, E.; Coluccia, S.; Thomas, J. M., Probing the Titanium Sites in Ti–MCM41 by Diffuse Reflectance and Photoluminescence UV–Vis Spectroscopies. *The Journal of Physical Chemistry B* **1997,** *101* (44), 8836-8838.

84. Brutchey, R. L.; Ruddy, D. A.; Andersen, L. K.; Tilley, T. D., Influence of Surface Modification of Ti–SBA15 Catalysts on the Epoxidation Mechanism for Cyclohexene with Aqueous Hydrogen Peroxide. *Langmuir* **2005,** *21* (21), 9576-9583.

85. Yang, G.; Pidko, E. A.; Hensen, E. J. M., Structure, Stability, and Lewis Acidity of Mono and Double Ti, Zr, and Sn Framework Substitutions in BEA Zeolites: A Periodic Density Functional Theory Study. *The Journal of Physical Chemistry C* **2013,** *117* (8), 3976-3986.

86. Tielens, F.; Shishido, T.; Dzwigaj, S., What Do the Niobium Framework Sites Look Like in Redox Zeolites? A Combined Theoretical and Experimental Investigation. *Journal of Physical Chemistry* **2010,** *114* (7), 3140-3147.

87. Nogier, J.-P.; Millot, Y.; Man, P. P.; Méthivier, C.; Che, M.; Dzwigaj, S., Nature, Environment and Quantification of Titanium Species in TiSiBEA Zeolites Investigated by XRD, NMR, DR UV–Vis and XPS. *Catalysis Letters* **2009,** *130* (3-4), 588-592.

88. Nunes, C. D.; Valente, A. A.; Pillinger, M.; Rocha, J.; Gonçalves, I. S., Molecular Structure–Activity Relationships for the Oxidation of Organic Compounds Using Mesoporous Silica Catalysts Derivatised with Bis(halogeno)dioxomolybdenum(VI) Complexes. *Chemistry - A European Journal* **2003,** *9* (18), 4380-4390.

89. Morey, M. S.; Bryan, J. D.; Schwarz, S.; Stucky, G. D., Pore Surface Functionalization of MCM-48 Mesoporous Silica with Tungsten and Molybdenum Metal Centers: Perspectives on Catalytic Peroxide Activation. *Chemistry of Materials* **2000,** *12* (11), 3435-3444.

90. Merle, N.; Le Quéméner, F.; Barman, S.; Samantaray, M. K.; Szeto, K. C.; De Mallmann, A.; Taoufik, M.; Basset, J.-M., Well-defined silica supported bipodal molybdenum oxo alkyl complexes: a model of the active sites of industrial olefin metathesis catalysts. *Chem. Commun.* **2017,** *53* (82), 11338-11341.

91. Chan, K. W.; Mance, D.; Safonova, O. V.; Copéret, C., Well-Defined Silica-Supported Tungsten(IV)–Oxo Complex: Olefin Metathesis Activity, Initiation, and Role of Brønsted Acid Sites. *Journal of the American Chemical Society* **2019,** *141* (45), 18286-18292.

92. Mougel, V.; Chan, K.-W.; Siddiqi, G.; Kawakita, K.; Nagae, H.; Tsurugi, H.; Mashima, K.; Safonova, O.; Copéret, C., Low Temperature Activation of Supported Metathesis Catalysts by Organosilicon Reducing Agents. *ACS Central Science* **2016,** *2* (8), 569-576.

93. Skara, G.; Baran, R.; Onfroy, T.; De Proft, F.; Dzwigaj, S.; Tielens, F., Characterization of zeolitic intraframework molybdenum sites. *Microporous and Mesoporous Materials* **2016,** *225*, 355-364.

94. Kurleto, K.; Tielens, F.; Handzlik, J., Isolated Molybdenum(VI) and Tungsten(VI) Oxide Species on Partly Dehydroxylated Silica: A Computational Perspective. *The Journal of Physical Chemistry C* **2020,** *124* (5), 3002-3013.

95. Sever, R. R.; Root, T. W., DFT Study of Solvent Coordination Effects on Titanium-Based Epoxidation Catalysts. Part Two: Reactivity of Titanium Hydroperoxo Complexes in Ethylene Epoxidation. *The Journal of Physical Chemistry B* **2003,** *107* (17), 4090-4099.

96. Crosman, A.; Gelbard, G.; Poncelet, G.; Parvulescu, V. I., Epoxidation of cyclohexene and indene with hydrogen peroxide in the presence of WO5 onto hydroxyapatite as catalyst. *Applied Catalysis A: General* **2004,** *264* (1), 23-32.

97. Tatsumi, T.; Yamamoto, K.; Tajima, H.; Tominaga, H.-O., Shape Selective Epoxidation of Alkenes Catalyzed by Polyoxometalate-Intercalated Hydrotalcite. *Chemistry Letters* **1992,** *21* (5), 815-818.

98. Cundari, T. R.; Drago, R. S., Molecular orbital investigation of ruthenium-oxo-catalyzed epoxidations. *Inorganic Chemistry* **1990,** *29* (3), 487-493.

99. Dobson, J. C.; Seok, W. K.; Meyer, T. J., Epoxidation and catalytic oxidation of olefins based on a RuIV:O/RuII-OH2 couple. *Inorganic Chemistry* **1986,** *25* (10), 1513-1514.

100. Raj, N. K. K.; Ramaswamy, A. V.; Manikandan, P., Oxidation of norbornene over vanadium-substituted phosphomolybdic acid catalysts and spectroscopic investigations. *Journal of Molecular Catalysis A: Chemical* **2005,** *227* (1-2), 37-45.

101. Kuznetsov, M. L.; Pessoa, J. C., Epoxidation of olefins catalysed by vanadium–salan complexes: a theoretical mechanistic study. *Dalton Transactions* **2009,** (28), 5460.

102. Bregante, D. T.; Tan, J. Z.; Schultz, R. L.; Ayla, E. Z.; Potts, D. S.; Torres, C.; Flaherty, D. W., Catalytic Consequences of Oxidant, Alkene, and Pore Structures on Alkene Epoxidations within Titanium Silicates. *ACS Catalysis* **2020**, 10169-10184.

103. Hammond, G. S., A Correlation of Reaction Rates. *Journal of the American Chemical Society* **1955,** *77* (2), 334-338.

104. Klein, D. R., *Organic Chemistry*. 2nd ed.; Wiley: 2013.

105. Mulliken, R. S., A New Electroaffinity Scale; Together with Data on Valence States and on Valence Ionization Potentials and Electron Affinities. *Journal of Chemical Physics* **1934,** *2*.

106. M. Taramasso, G. P., B. Notari Preparation of porous crystalline synthetic material comprised of silicon and titanium oxides. US 4410501, 1983.

107. Kholdeeva, O. A.; Maksimovskaya, R. I., Titanium- and zirconium-monosubstituted polyoxometalates as molecular models for studying mechanisms of oxidation catalysis. *Journal of Molecular Catalysis A: Chemical* **2007,** *262* (1-2), 7-24.

108. Oldroyd, R. D.; Sankar, G.; Thomas, J. M.; Özkaya, D., Enhancing the Performance of a Supported Titanium Epoxidation Catalyst by Modifying the Active Center. *The Journal of Physical Chemistry B* **1998,** *102* (11), 1849-1855.

109. Wolek, A. T. Y.; Ardagh, M. A.; Pham, H. N.; Alayoglu, S.; Datye, A. K.; Notestein, J. M., Creating Brønsted acidity at the SiO2-Nb2O5 interface. *Journal of Catalysis* **2021,** *394*, 387-396.

110. Niklas Pfriem, P. H. H., Sebastian Eckstein, Sungmin Kim, Qiang Liu, Hui Shi,Lara Milakovic, Yuanshuai Liu, Gary L. Haller, Eszter Baráth, Yue Liu, Johannes A. Lercher, Role of the ionic environment in enhancing the activity of reacting molecules in zeolite pores. *Science* **2021,** *372* (6465), 952-957.

111. Ardagh, M. A.; Bregante, D. T.; Flaherty, D. W.; Notestein, J. M., Controlled Deposition of Silica on Titania-Silica to Alter the Active Site Surroundings on Epoxidation Catalysts. *ACS Catalysis* **2020,** *10* (21), 13008-13018.

112. Tatsumi, T.; Koyano, K. A.; Igarashi, N., Remarkable activity enhancement by trimethylsilylation in oxidation of alkenes and alkanes with H2O2 catalyzed by titanium-containing mesoporous molecular sieves. *Chemical Communications* **1998,** (3), 325-326.

113. Fang, X.; Wang, Q.; Zheng, A.; Liu, Y.; Wang, Y.; Deng, X.; Wu, H.; Deng, F.; He, M.; Wu, P., Fluorine-planted titanosilicate with enhanced catalytic activity in alkene epoxidation with hydrogen peroxide. *Catalysis Science & Technology* **2012,** *2* (12), 2433.

114. Cheng, L.; Morrone, J. A.; Berne, B. J., Structure and Dynamics of Acetonitrile Confined in a Silica Nanopore. *The Journal of Physical Chemistry C* **2012,** *116* (17), 9582-9593.

115. Madon, R. J.; Iglesia, E., Catalytic reaction rates in thermodynamically non-ideal systems. *Journal of Molecular Catalysis A: Chemical* **2000,** *163* (1-2), 189-204.

116. Corma, A.; Esteve, P.; MartíNez, A., Solvent Effects during the Oxidation of Olefins and Alcohols with Hydrogen Peroxide on Ti-Beta Catalyst: The Influence of the Hydrophilicity–Hydrophobicity of the Zeolite. *Journal of Catalysis* **1996,** *161* (1), 11-19.

117. Gounder, R.; Davis, M. E., Beyond shape selective catalysis with zeolites: Hydrophobic void spaces in zeolites enable catalysis in liquid water. *AIChE Journal* **2013,** *59* (9), 3349-3358.

118. Bates, J. S.; Gounder, R., Kinetic effects of molecular clustering and solvation by extended networks in zeolite acid catalysis. *Chemical Science* **2021,** *12* (13), 4699-4708.

119. Eckstein, S.; Hintermeier, P. H.; Zhao, R.; Baráth, E.; Shi, H.; Liu, Y.; Lercher, J. A., Influence of Hydronium Ions in Zeolites on Sorption. *Angewandte Chemie International Edition* **2019,** *58* (11), 3450-3455.

120. Hibbitts, D. D.; Loveless, B. T.; Neurock, M.; Iglesia, E., Mechanistic Role of Water on the Rate and Selectivity of Fischer-Tropsch Synthesis on Ruthenium Catalysts. *Angewandte Chemie International Edition* **2013,** *52* (47), 12273-12278.

121. Sievers, C.; Noda, Y.; Qi, L.; Albuquerque, E. M.; Rioux, R. M.; Scott, S. L., Phenomena Affecting Catalytic Reactions at Solid–Liquid Interfaces. *ACS Catalysis* **2016,** *6* (12), 8286-8307.

122. Saavedra, J. D., H. A.; Pursell, C. J.; Grabow, L. C.; Chandler, B. D., The critical role of water at the gold-titania interface in catalytic CO oxidation. *Science* **2014,** *345* (6204), 1599-1602.

123. Maschmeyer, T.; Rey, F.; Sankar, G.; Thomas, J. M., Heterogeneous catalysts obtained by grafting metallocene complexes onto mesoporous silica. *Nature* **1995,** *378* (6553), 159-162.

124. Gao, X.; Bare, S. R.; Fierro, J. L. G.; Banares, M. A.; Wachs, I. E., Preparation and in-Situ Spectroscopic Characterization of Molecularly Dispersed Titanium Oxide on Silica. *The Journal of Physical Chemistry B* **1998,** *102* (29), 5653-5666.

125. Shetti, V. N.; Manikandan, P.; Srinivas, D.; Ratnasamy, P., Reactive oxygen species in epoxidation reactions over titanosilicate molecular sieves. *Journal of Catalysis* **2003,** *216* (1-2), 461-467.

126. Henderson, G. S.; Neuville, D. R.; Cochain, B.; Cormier, L., The structure of GeO2–SiO2 glasses and melts: A Raman spectroscopy study. *Journal of Non-Crystalline Solids* **2009,** *355* (8), 468-474.

127. Durben, D. J.; Wolf, G. H., Raman spectroscopic study of the pressure-induced coordination change inGeO2glass. *Physical Review B* **1991,** *43* (3), 2355-2363.

128. Khodakov, A.; Olthof, B.; Bell, A. T.; Iglesia, E., Structure and Catalytic Properties of Supported Vanadium Oxides: Support Effects on Oxidative Dehydrogenation Reactions. *Journal of Catalysis* **1999,** *181* (2), 205-216.

129. Noh, J. S.; Schwarz, J. A., Estimation of the point of zero charge of simple oxides by mass titration. *Journal of Colloid and Interface Science* **1989,** *130* (1), 157-164.

130. Mahmood, T.; Saddique, M. T.; Naeem, A.; Westerhoff, P.; Mustafa, S.; Alum, A., Comparison of Different Methods for the Point of Zero Charge Determination of NiO. *Industrial & Engineering Chemistry Research* **2011,** *50* (17), 10017-10023.

131. Kosmulski, M., Isoelectric points and points of zero charge of metal (hydr)oxides: 50years after Parks' review. *Advances in Colloid and Interface Science* **2016,** *238*, 1-61.

132. Tan, J. Z.; Bregante, D. T.; Torres, C.; Flaherty, D. W., Transition state stabilization depends on solvent identity, pore size, and hydrophilicity for epoxidations in zeolites. *Journal of Catalysis* **2022,** *405*, 91-104.

133. Grifoni, E.; Piccini, G.; Lercher, J. A.; Glezakou, V.-A.; Rousseau, R.; Parrinello, M., Confinement effects and acid strength in zeolites. *Nature Communications* **2021,** *12* (1).

134. Gao, Y.; Klunder, J. M.; Hanson, R. M.; Masamune, H.; Ko, S. Y.; Sharpless, K. B., Catalytic asymmetric epoxidation and kinetic resolution: modified procedures including in situ derivatization. *Journal of the American Chemical Society* **1987,** *109* (19), 5765-5780.

135. Notari, B., Titanium Silicalite: A New Selective Oxidation Catalyst. Elsevier: 1991; pp 343-352.

136. Miao, C.; Zhu, Q.; Yi, Y.; Su, J.; He, N.; Liu, J.; Guo, H., Gas-Phase Epoxidation of Propylene with Hydrogen Peroxide Vapor: Effect of Modification with NaOH on TS-1 Titanosilicate Catalyst in the Presence of Tetra-propylammonium Bromide. *Industrial & Engineering Chemistry Research* **2019,** *58* (27), 11739-11749.

137. Zhu, Q.; Miao, C.; Yi, Y.; Liu, C.; Guo, Y.; Feng, Z.; Guo, H., Solvent-free gas-phase epoxidation of propylene in fluidized bed reactor. *AIChE Journal* **2021,** *67* (5).

138. Klemm, E. D., E.; Schwarz, T.; Kruppa, T.; Lange De Oliveira, A.; Becker, F.; Markowz, G.; Schirrmeister, S.; Rudiger, S.; Caspary, K. J.; Schu, F.; Ho, D., Direct Gas-Phase Epoxidation of Propene with Hydrogen Peroxide on TS-1

Zeolite in a Microstructured Reactor. *Industrial & Engineering Chemistry Research* **2008,** *47*, 2086-2090.

139. Perez Ferrandez, D. M.; De Croon, M. H. J. M.; Schouten, J. C.; Nijhuis, T. A., Gas-Phase Epoxidation of Propene with Hydrogen Peroxide Vapor. *Industrial & Engineering Chemistry Research* **2013,** *52* (30), 10126-10132.

140. Dyson, P. J.; Jessop, P. G., Solvent effects in catalysis: rational improvements of catalysts via manipulation of solvent interactions. *Catalysis Science & Technology* **2016,** *6* (10), 3302-3316.

141. Agirrezabal-Telleria, I.; Iglesia, E., Stabilization of active, selective, and regenerable Ni-based dimerization catalysts by condensation of ethene withinordered mesopores. *Journal of Catalysis* **2017,** *352*, 505-514.

142. Agirrezabal-Telleria, I.; Iglesia, E., Mechanistic insights and consequences of intrapore liquids in ethene, propene, and butene dimerization on isolated Ni2+ sites grafted within aluminosilicate mesopores. *Journal of Catalysis* **2020,** *389*, 690-705.

143. Caulkins, R.; Joshi, R.; Gounder, R.; Ribeiro, F. H., Effects of Ethene Pressure on the Deactivation of Ni-Zeolites During Ethene Oligomerization at Sub-ambient Temperatures. *ChemCatChem* **2022,** *14* (1).

144. Torres, C. P., David S.; Flaherty, David W., Solvent Mediated Interactions on Alkene Epoxidations in Ti-MFI: Effects of Solvent Identity and Silanol Densities. **2022**.

145. Potts, D. S. K., Ohsung; Flaherty, David W. , Engineering the Solid-liquid Interface: Effects of Aqueous-Organic Solvent Mixtures on Competition Between Zeolite-Catalyzed Epoxidation and H_2O_2 Decomposition Pathways. **2022**.

146. Kwon, O. A., E. Zeynep; Potts, David S.; Flaherty, David W., Effects of Solvent-pore Interaction on Rates and Barriers for Vapor-phase Alkene Epoxidation with Gaseous H_2O_2 in Ti-BEA Catalysts. **2022**.

147. Potts, D. S. J., Vijaya Sundar; Kwon, Ohsung; Ghosh, Richa; Mironenko, Alexander V.; Flaherty, David W. , Effects of Interactions Between Alkyl Chains and Solvent Structures on Lewis-Acid Catalyzed Epoxidations. **2022**.

148. Ahn, S.; Nauert, S. L.; Hicks, K. E.; Ardagh, M. A.; Schweitzer, N. M.; Farha, O. K.; Notestein, J. M., Demonstrating the Critical Role of Solvation in Supported Ti and Nb Epoxidation Catalysts via Vapor-Phase Kinetics. *ACS Catalysis* **2020**, 2817-2825.

149. Harris, J. W.; Cordon, M. J.; Di Iorio, J. R.; Vega-Vila, J. C.; Ribeiro, F. H.; Gounder, R., Titration and quantification of open and closed Lewis acid sites in Sn-Beta zeolites that catalyze glucose isomerization. *Journal of Catalysis* **2016,** *335*, 141-154.

150. Antonelli, E.; D'Aloisio, R.; Gambaro, M.; Fiorani, T.; Venturello, C., Efficient Oxidative Cleavage of Olefins to Carboxylic Acids with Hydrogen Peroxide Catalyzed by Methyltrioctylammonium Tetrakis(oxodiperoxotungsto)phosphate(3−) under Two-Phase Conditions. Synthetic Aspects and Investigation of the Reaction Course. *The Journal of Organic Chemistry* **1998,** *63* (21), 7190-7206.

151. Kwon, S.; Schweitzer, N. M.; Park, S.; Stair, P. C.; Snurr, R. Q., A kinetic study of vapor-phase cyclohexene epoxidation by H2O2 over mesoporous TS-1. *Journal of Catalysis* **2015,** *326*, 107-115.

152. Eyring, H., The Activated Complex and the Absolute Rate of Chemical Reactions *Chemical Reviews* **1935,** *17*, 65-77.

153. Blaser, H.-U.; Pugin, B.; Spindler, F., Progress in enantioselective catalysis assessed from an industrial point of view. *Journal of Molecular Catalysis A: Chemical* **2005,** *231* (1-2), 1-20.

154. Blaser, H. U.; Spindler, F.; Studer, M., Enantioselective catalysis in fine chemicals production. *Applied Catalysis A: General* **2001,** *221* (1-2), 119-143.

155. Noyori, R., Asymmetric Catalysis: Science and Opportunities (Nobel Lecture). *Angew Chem Int Ed* **2002,** *41*, 2008-2022.

156. Choi, W. J.; Choi, C. Y., Production of chiral epoxides: Epoxide hydrolase-catalyzed enantioselective hydrolysis. *Biotechnology and Bioprocess Engineering* **2005,** *10* (3), 167-179.

157. Meunier, D.; De Mallmann, A.; Basset, J.-M., Asymmetric epoxidation of allylic alcohols catalyzed by (SiO)xTa(OEt)_(3-x)(dialkyl tartrate diolate): influence of the reaction conditions. *Topics in Catalysis* **2003,** *23* (1/4), 183-189.

158. Meunier, D. P., Arnaud; de Mallmann, Aimery; Basset, Jean-Marie, Silica-Supported Tantalum Catalysts for Asymmetric Epoxidations of Allyl Alcohols. *Angewandte Chemie International Edition* **1999,** *38* (23), 3540-3542.

159. Campos-Martin, J. M.; Blanco-Brieva, G.; Fierro, J. L. G., Hydrogen Peroxide Synthesis: An Outlook beyond the Anthraquinone Process. *Angewandte Chemie International Edition* **2006,** *45* (42), 6962-6984.

160. Haruta, M.; Uphade, B. S.; Tsubota, S.; Miyamoto, A., Selective oxidation of propylene over gold deposited on titanium-based oxides. *Research on Chemical Intermediates* **1998,** *24* (3), 329-336.

161. Cumaranatunge, L.; Delgass, W., Enhancement of Au capture efficiency and activity of Au/TS-1 catalysts for propylene epoxidation. *Journal of Catalysis* **2005,** *232* (1), 38-42.

162. Lee, W.-S. A., Cem M.; Stach, Eric A.; Ribeiro, Fabio H.; Delgass, Nicholas, Reproducible preparation of Au/TS-1 with high reaction rate for gas phase epoxidation of propylene. *Journal of Catalysis* **2012,** *287*, 178-189.

163. Cumaranatunge, L. D., Nicholas W., Enhancement of Au capture efficiency and activity of Au/TS-1 catalysts for propylene epoxidation. *Journal of Catalysis* **2005,** *232*, 38-42.

164. Puértolas, B. H., A.K.; García,T.; Solsona, B.; Torrente-Murciano, Laura, In-situ synthesis of hydrogen peroxide in tandem with selective oxidation reactions: A mini-review. *Catalysis Today* **2015,** *248*, 115-127.

165. Jin, Q.; Bao, J.; Sakiyama, H.; Tsubaki, N., Preparation, structure and performance of TS-1 zeolite-coated Au–Pd/TiO2–SiO2 capsule catalyst for propylene epoxidation with oxygen and hydrogen. *Research on Chemical Intermediates* **2011,** *37* (2-5), 177-184.

166. Meiers, R. D., U.; Holderich, W. F., Synthesis of Propylene Oxide from Propylene, Oxygen, and Hydrogen Catalyzed by Palladium–Platinum–Containing Titanium Silicalite. *Journal of Catalysis* **1998,** *176*, 376-386.

167. Lee, W.-S. A., Cem M.; Stach, Eric A.; Ribeiro, Fabio H.; Delgass, Nicholas, Enhanced reaction rate for gas-phase epoxidation of propylene using H2 and O2 by Cs promotion of Au/TS-1. *Journal of Catalysis* **2013,** *308*, 98-113.

168. Lu, J. Z., Xiaoming; Bravo-Suarez, Juan J.; Fujitani, Tadahiro; Oyama, S. Ted Effect of composition and promoters in Au/TS-1 catalysts for direct propylene epoxidation using H2 and O2. *Catalysis Today* **2009,** *147*, 186-195.

169. Wang, F. C., Q.; Ma, J., The study of the uncalcined Au catalyst and inorganic salts on direct gas-phase epoxidation of propylene. *Catalysis Communications* **2007,** *8* (12), 1947-1952.

170. Baran, R.; Millot, Y.; Onfroy, T.; Krafft, J.-M.; Dzwigaj, S., Influence of the nitric acid treatment on Al removal, framework composition and acidity of BEA zeolite investigated by XRD, FTIR and NMR. *Microporous and Mesoporous Materials* **2012,** *163*, 122-130.

171. Ziolek, M.; Sobczak, I.; Decyk, P.; Wolski, L., The ability of Nb2O5 and Ta2O5 to generate active oxygen in contact with hydrogen peroxide. *Catalysis Communications* **2013,** *37*, 85-91.

172. Ziolek, M.; Sobczak, I.; Decyk, P.; Sobańska, K.; Pietrzyk, P.; Sojka, Z., Search for reactive intermediates in catalytic oxidation with hydrogen peroxide over amorphous niobium(V) and tantalum(V) oxides. *Applied Catalysis B: Environmental* **2015,** *164*, 288-296.

173. Williams, C. C.; Ekerdt, J. G.; Jehng, J. M.; Hardcastle, F. D.; Turek, A. M.; Wachs, I. E., A Raman and ultraviolet diffuse reflectance spectroscopic investigation of silica-supported molybdenum oxide. *The Journal of Physical Chemistry* **1991,** *95* (22), 8781-8791.

174. Myers, R. T., The Periodicity of Electron Affinity. *Journal of Chemical Education* **1990,** *67*, 307-308.

175. Brown, T. L. L., Jr., H. E.; Bursten; B. E.; Murphy, C. J.; Woodward, P. M. , *Chemistry: The Central Science*. 12th ed.; Pearson: 2012.

176. Rajalakshmi, M.; Arora, A. K.; Bendre, B. S.; Mahamuni, S., Optical phonon confinement in zinc oxide nanoparticles. *Journal of Applied Physics* **2000,** *87* (5), 2445-2448.

177. Moulahi, A.; Sediri, F.; Gharbi, N., Hydrothermal synthesis of nanostructured zinc oxide and study of their optical properties. *Materials Research Bulletin* **2012,** *47* (3), 667-671.

APPENDIX A

SUPPLEMENTAL DATA AND ANALYSIS FOR CHAPTER 2

A1. *Ex situ* Characterization of M-BEA

A1.1 Diffuse Reflectance UV-Vis Spectra of M-BEA

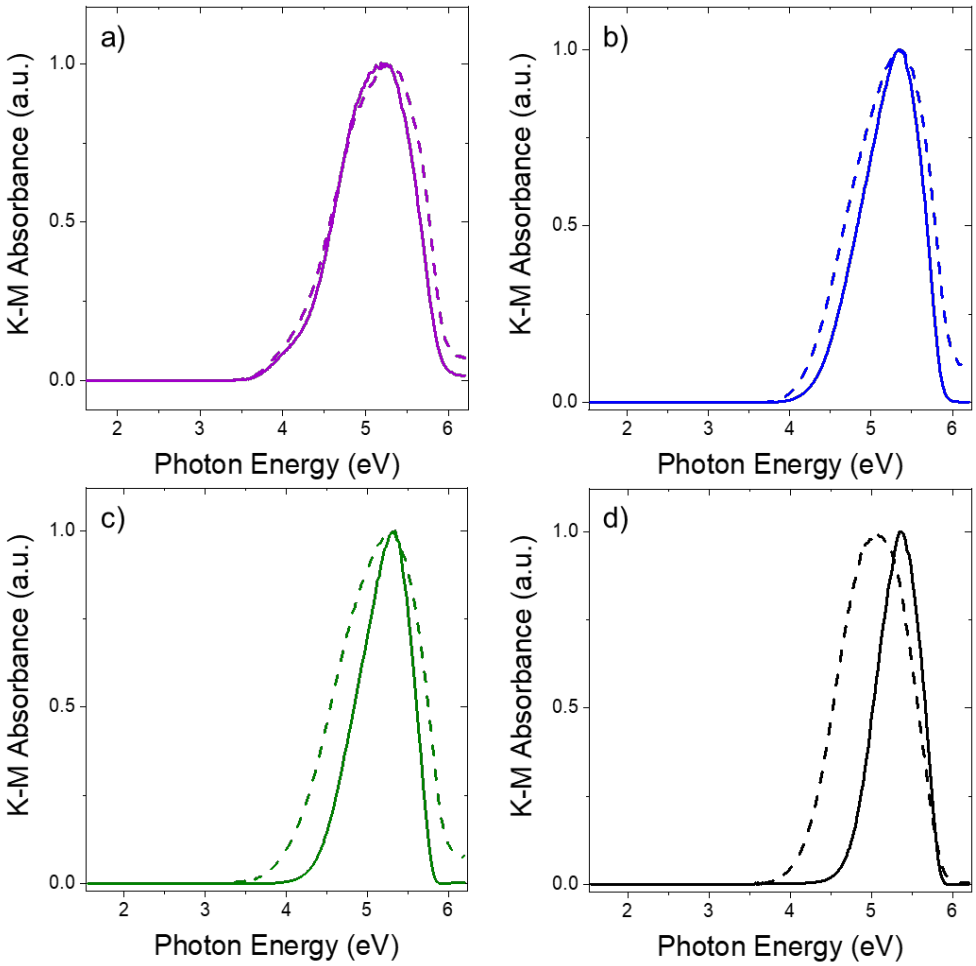

Figure A1. Tauc plots for M-BEA. Solid lines represent a low metal loading and dashed lines represent higher metal loading for (a) Mo-BEA, (b) Ti-BEA, (c) W-BEA, and (d) Nb-BEA.

The band gaps for M-BEA in these Tauc plots are much greater than those for their respective bulk metal oxides, implying the metals are dispersed when incorporated into the zeolite BEA framework. Calculated band gaps are summarized in **Table A1**.

Table A1. Metal loading and band gap for low and high metal loading M-BEA and band gap for corresponding metal oxide

Catalyst	Low metal loading (solid lines)		High metal loading (dashed lines)		Bulk metal oxide band gap (eV)
	Metal loading (%)	Band gap (eV)	Metal loading (%)	Band gap (eV)	
Mo-BEA	0.40	3.96	3.2	3.92	2.9
Ti-BEA	0.25	4.34	1.8	4.07	3.2
W-BEA	0.55	4.41	7.8	3.85	2.8
Nb-BEA	0.22	4.73	3.5	4.1	3.4

A1.2 X-ray Diffraction of M-BEA

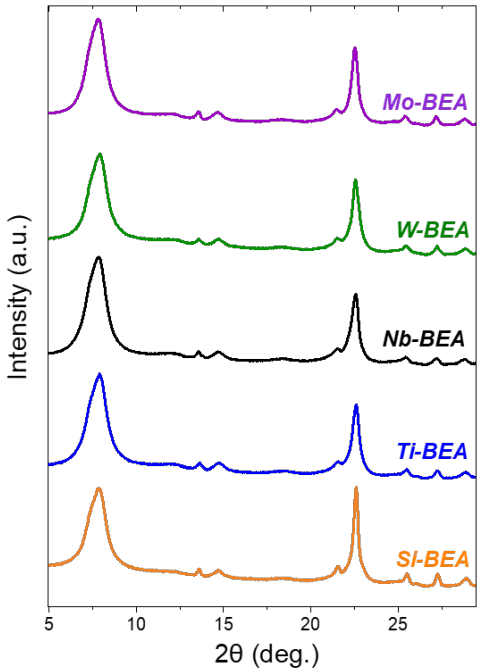

Figure A2. Powder X-ray diffractograms for 0.25 wt% Ti-BEA, 0.22 wt% Nb-BEA, 1.1 wt% W-BEA, and 0.4 wt % Mo-BEA under ambient conditions show the zeolite BEA structure is maintained after post-synthetic modification.

The similarities between the diffraction patterns of Si-BEA and metal-incorporated BEA suggest the structure of the BEA framework remains intact following dealumination and transition metal incorporation. At these low metal loadings (< 0.25 metal atoms per unit cell), the XRD features do not display observable shifts in the peak located at 22.5°. In our past work, we reported shifts towards greater diffraction angles when group 4 and 5 metals were incorporated into the BEA framework.[19] These shifts indicated an expansion of the zeolite lattice to accommodate these framework substituents.[19, 170] However, because these M-BEA have low metal density, the shift is less apparent in their diffractograms.

A1.3 Raman Spectra of Si-BEA and W-BEA

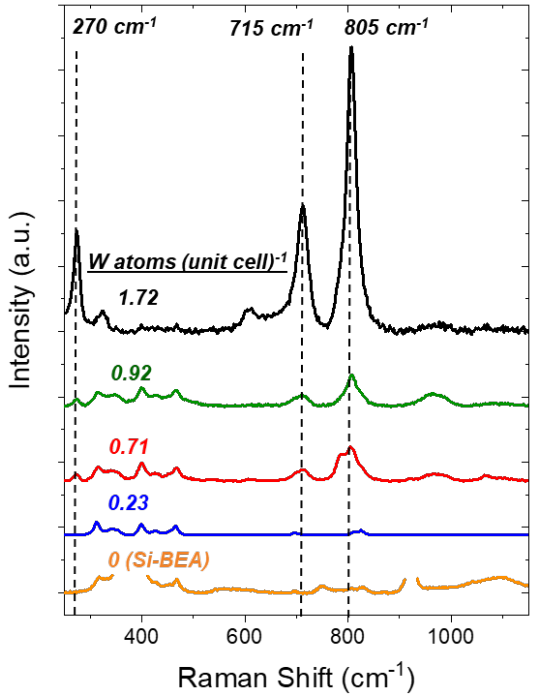

Figure A3. Raman spectra (442 nm, 0.8 mW μm^{-2}) of W-BEA pellets (~5-10 mg, 0.23 ( ), 0.71 (—), 0.93 (—), and 1.72 (—) W atoms per unit cell) under ambient conditions (Si-BEA (—) under 0.01 M H_2O_2 in CH_3CN flow 1 ml/min, 313 K). All spectra are rescaled to give a constant intensity for the 312 cm^{-1} feature of the BEA framework.

Ex situ Raman spectra of W-BEA show increasing intensities for the three vibrational modes indicative of bulk WO_3, which include 270 cm^{-1}, 715 cm^{-1}, and 805 cm^{-1}.[61] These trends show the emergence of extra-framework W atoms when loadings surpass 1 wt% (i.e., 0.23 W atoms per unit

cell) that increase further with greater W loadings. Features between 300-550 cm^{-1} correspond to vibrations of the BEA framework.[71]

A2 *In situ* Characterization for H_2O_2 Activation on M-BEA

A2.1 *In Situ* Raman Spectra of M-BEA

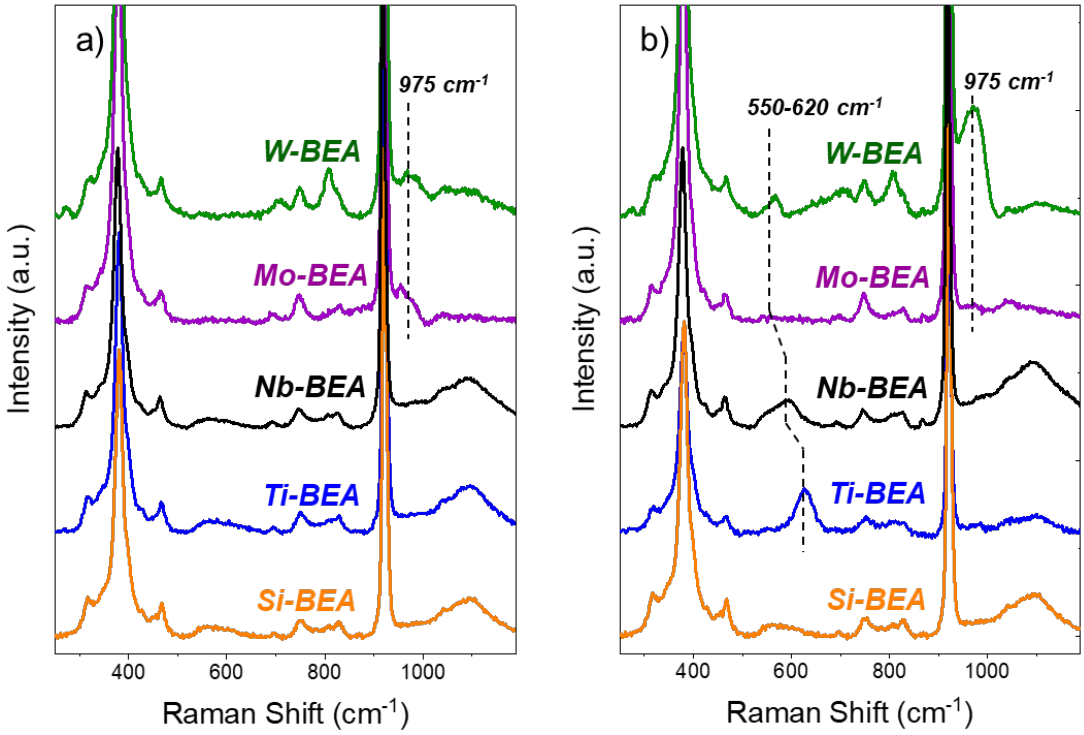

Figure A4. Raman spectra (442 nm laser, 0.8 mW μm^{-2}) of M-BEA samples obtained (a) during contact with neat CH_3CN for 0.5 h, and (b) after 0.5 h contact with a flowing solution of H_2O_2 in CH_3CN (10 mM H_2O_2, 39 mM H_2O in CH_3CN; 1 ml min^{-1}) at 313 K. Spectra of Si-, Ti-, Nb-, and W-BEA are taken at steady-state, whereas Mo-BEA shows further changes following 20 min. All spectra are normalized to the BEA framework feature at 312 cm^{-1}. M-BEA synthesized with high metal content (1.2 wt % Ti, 3 wt % Nb, 5 wt % W, 5 wt % Mo) are used to increase Raman peak intensity and clearly observe features unique to H_2O_2 activation on incorporated metal atoms.

Figure A4a shows features on M-BEA in flowing neat CH_3CN (1 ml min^{-1}) prior to contact with H_2O_2, and these spectra contain features indicative of oxygen ligands (e.g., metal-oxos; M=O) on Mo-BEA and W-BEA at 950-975 cm^{-1}.[61, 77] Features between 694-825 cm^{-1} are framework

vibrations of Si-BEA[71] and appear in all spectra. Subsequently, the liquid stream is changed to a H_2O_2 solution (10 mM H_2O_2, 39 mM H_2O in CH_3CN; 1 ml min^{-1}), and Figure A4b shows spectra obtained after 0.5 h. These spectra include a new vibrational feature between 550-620 cm^{-1} on Ti-BEA, Nb-BEA, and W-BEA, which corresponds to a Raman-enhanced vibration mode that represents the formation of metal-peroxo (M-η^2-O_2) species.[61, 72, 73] Metal-peroxo species exist in equilibrium with metal-hydroperoxo species (M-OOH),[23, 80] which can be detected by UV-Vis (Section A2.2.) but have yet to be reliably detected by Raman spectroscopy.[72] In contrast, Raman spectra of Mo-BEA in flowing H_2O_2 solutions exhibit a short-lived peak around 560 cm^{-1} (not shown here but in Figure 2.2), which indicates the initial formation of a Mo-η^2-O_2 intermediate. However, all features corresponding to Mo atoms within the BEA framework disappear after 0.5 h contact with flowing H_2O_2. These changes show the loss of Mo atoms from the zeolite framework, which agrees with results from energy-dispersive X-ray fluorescence (EDXRF) that show the loss of at least 90 % of Mo atoms from the sample after the experiment concludes.

Note: Figure A4a contains a feature around 560 cm^{-1} on Si-, Ti-, and Nb-BEA samples that may indicate a relatively lower degree of crystallinity of the BEA framework.[69] We believe the absence of this feature on W- and Mo-BEA, which are synthesized using the same parent batch of dealuminated BEA, may result from a slight change in the focus of the laser or shift in the position of the pellet during the experiment.

A2.2 *In situ* UV-Vis Spectra of M-BEA

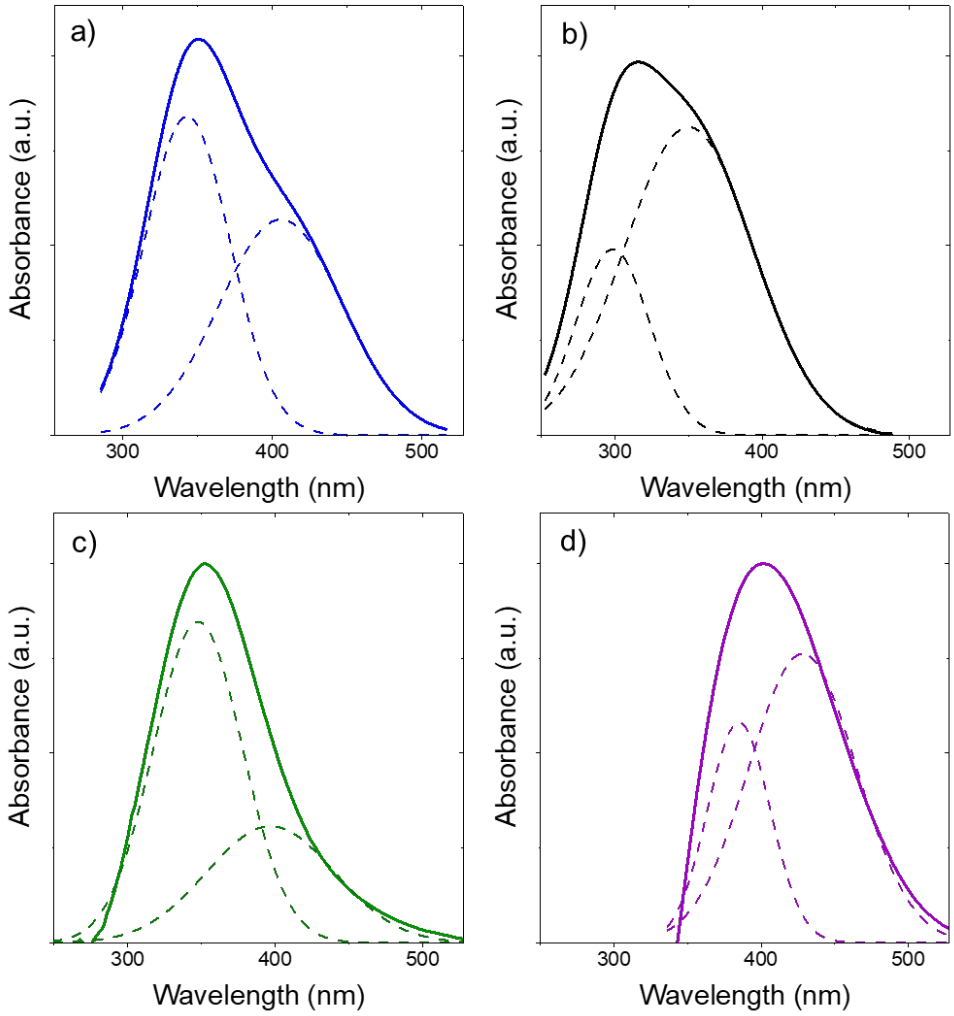

Figure A5. *In situ* UV-Vis spectra for (a) Ti-BEA (0.25 wt %), (b) Nb-BEA (0.22 wt %), (c) W-BEA (1.1 wt %), and (d) Mo-BEA (0.40 wt %) while flowing a solution of H_2O_2 (10 mM H_2O_2, 39 mM H_2O, in CH_3CN, 1 ml min^{-1}) at 313 K. Each spectrum shows the difference between the H_2O_2-activated sample and the corresponding UV-Vis spectrum for the bare M-BEA sample, and all difference spectra are normalized to the maximum absorbance value.

Figure A5 shows steady-state UV-Vis spectra of reactive intermediates formed upon M-BEA samples by activation of solution-phase H_2O_2 (10 mM H_2O_2, 39 mM H_2, in CH_3CN, 1 ml min^{-1}) at 313 K. These spectra are deconvoluted by subtracting a baseline and fitting Gaussian functions to two features (fixed baseline at 0, initial guesses for peak positions are determined by literature values for LMCT bands of M-(η^2-O_2) and M-OOH) using OriginPro software. The two resulting

features represent the individual contributions of M-(η^2-O_2) and M-OOH surface intermediates formed at framework transition metal atoms and to give the ligand-to-metal charge transfer (LMCT) energies for these oxygen ligands. M-(η^2-O_2) species absorb photons at higher energies (shorter λ) than M-OOH species.[72, 74, 81, 125, 171] The relative LMCT energies of active oxygen species correlates with the electrophilicity of the reactive intermediates, which can be related to turnover rates and apparent activation enthalpies for alkene epoxidation[10] and thiophene oxidations[65] on group 4 and 5 transition metal substituted BEA catalysts.

A2.3 Transient *In Situ* UV-Vis Spectra of W-BEA and Mo-BEA

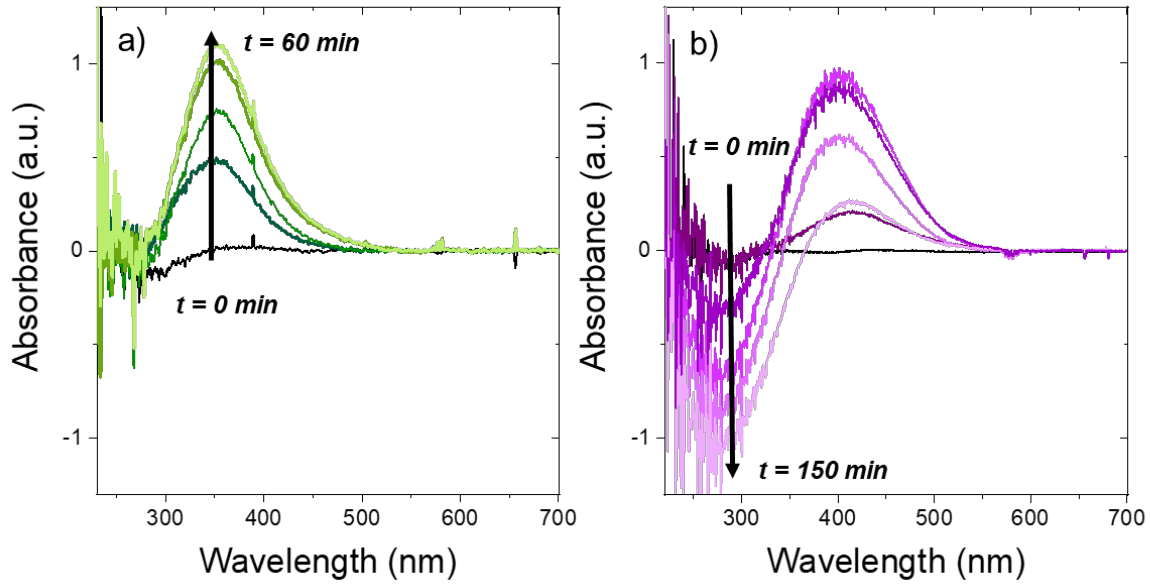

Figure A6. *In situ* UV-Vis spectra of (a) W-BEA (1.1 wt %), and (b) Mo-BEA (0.4 wt %) pellets within flowing solutions of H_2O_2 (10 mM H_2O_2, 39 mM H_2O, in CH_3CN, 1 cm^3 min^{-1}) at 313 K. Each spectrum shows the difference between the M-BEA sample after contact with H_2O_2 for a given period of time and the corresponding UV-Vis spectrum for the M-BEA sample in a solution of CH_3CN (39 mM H_2O in CH_3CN, 1 cm^3 min^{-1}) at 313K, and all difference spectra are normalized such that the maximum absorbance for the LMCT band in the series corresponds to a value of unity.

Figure A6 shows time-resolved *in situ* UV-Vis spectra for W-BEA and Mo-BEA within flowing H_2O_2 solutions (10 mM H_2O_2, 39 mM H_2, in CH_3CN, 1 ml min^{-1}) at 313 K. These series of spectra show the formation of M-η^2-O_2 and M-OOH intermediates with LMCT features for M-(η^2-O_2) at 310 nm (W-BEA) and 360 nm (Mo-BEA)[81] and for M-OOH at lower energies, as an extension of assignments for Ti-BEA and Nb-BEA.[74, 125, 172] The UV-Vis features for H_2O_2-activated W-BEA attain steady-state after 1 h, however, the intensity of the absorbance features for Mo-BEA increase initially but then decrease with time. The features at lower wavelengths (< 300 nm) represent charge transfer from Mo centers to the zeolite framework. These features become increasingly negative during the course of the experiment, which indicates the dissolution and loss of Mo atoms from the BEA framework[173] consistent with the discussion of Raman spectra and EDXRF results in Section A2.1.

A3. Product Distributions for Cis-Stilbene Epoxidation with H_2O_2 over M-BEA

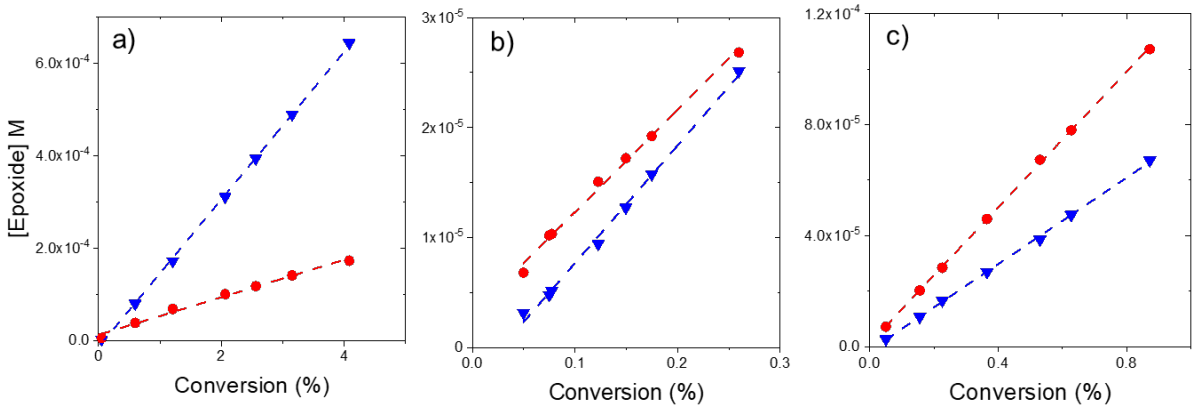

Figure A7. Concentrations of trans-stilbene epoxide (●) and cis-stilbene epoxide (▼) formed during the epoxidation of cis-stilbene (20 mM) with H_2O_2 as functions of cis-stilbene conversion over (a) Ti-BEA (0.25 wt %), (b) Nb-BEA (0.22 wt %), (c) W-BEA (1.1 wt %) in CH_3CN solutions (10 mM H_2O_2, 39 mM H_2O) at 313 K.

Figure A7 shows the concentrations of cis- and trans-stilbene epoxide formed by the epoxidation of cis-stilbene as functions of cis-stilbene conversion over Ti-, Nb-, and W-BEA samples in acetonitrile (20 mM cis-stilbene, 10 mM H_2O_2, 39 mM H_2O, in CH_3CN) at 313 K. These concentration profiles indicate that both epoxide isomers are primary products and the difference between their relative concentrations among the M-BEA catalysts suggest that distinct reactive

intermediates epoxidize alkenes on each material. Trans-stilbene epoxide forms through a multi-step homolytic mechanism for oxygen transfer from M-(η^2-O_2) intermediates to alkenes, which allows rotation of the C-C bond and gives nearly equimolar mixtures of trans- and cis-stilbene epoxides. In contrast, M-OOH and M=O species primarily produce cis-stilbene epoxide as a consequence of a concerted mechanism that does not permit isomerization during oxygen atom transfer to the C=C bond.[98, 99] Product distributions over M-BEA suggest Ti-BEA reacts primarily through Ti-OOH, because cis-stilbene epoxide is the predominant product. More similar quantities of cis- and trans-stilbene epoxides form over Nb-BEA and W-BEA, which implies that these catalysts epoxidize alkenes primarily with M-(η^2-O_2) species.

A4. *In Situ* Tert-Butyl Phosphonic Acid Site Titrations of M-BEA

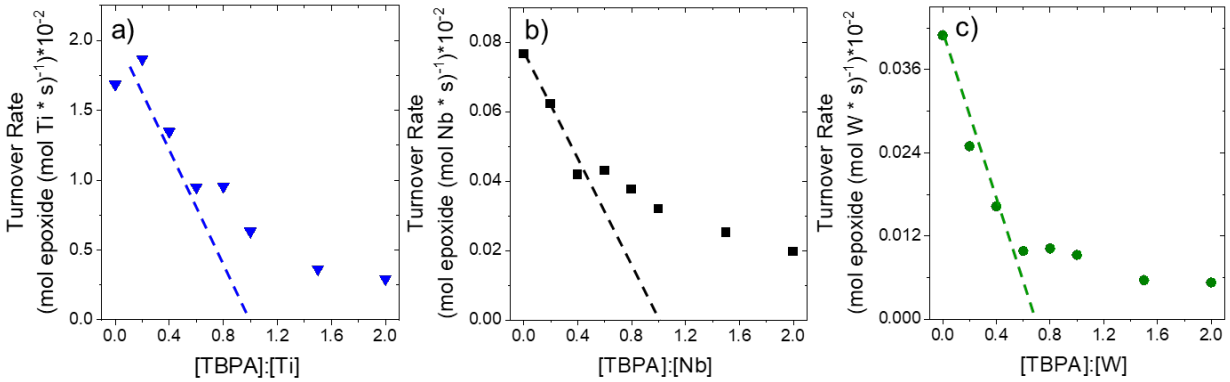

Figure A8. Tert-butyl phosphonic acid titrations of (a) Ti-BEA (0.25 wt %), (b) Nb-BEA (0.22 wt %), (c) W-BEA (1.1 wt %) during 1-hexene epoxidation with H_2O_2 in CH_3CN (10 mM C_6H_{12}, 10 mM H_2O_2, 39 mM H_2O, in CH_3CN) at 313 K.

The number of catalytically active metal atoms within each M-BEA sample were determined by *in situ* tert-butyl phosphonic acid (TBPA) site titrations. TBPA was introduced to a solution of 1-hexene and acetonitrile in a round bottom flask that contained the suspended M-BEA catalyst. The mixture was stirred for 0.5 h with the intent to equilibrate the coverage of TBPA on framework metal atoms. Then, H_2O_2 was added to initiate the reaction. The rates shown in Figure A8 are normalized by total metal content determined by EDXRF. As the ratio of the concentration of TBPA to total metal atoms ([TPBA]:[M]) increases, the normalized rates for epoxidation decrease,

because TBPA binds to a greater fraction of the metal sites. Extrapolation of the initial few linear points to the abscissa indicates that nearly 100 % of Ti and Nb atoms present form active sites for 1-hexene epoxidation, while ~70% of W atoms catalyze the epoxidation reaction. Inactivation of some incorporated W atoms is likely due to oligomerization (Figure A3 and Figure A9). Turnover rates, activation enthalpies, and enthalpies of 1,2-epoxyhexane adsorption reported in the main text were acquired from these specific M-BEA catalysts.

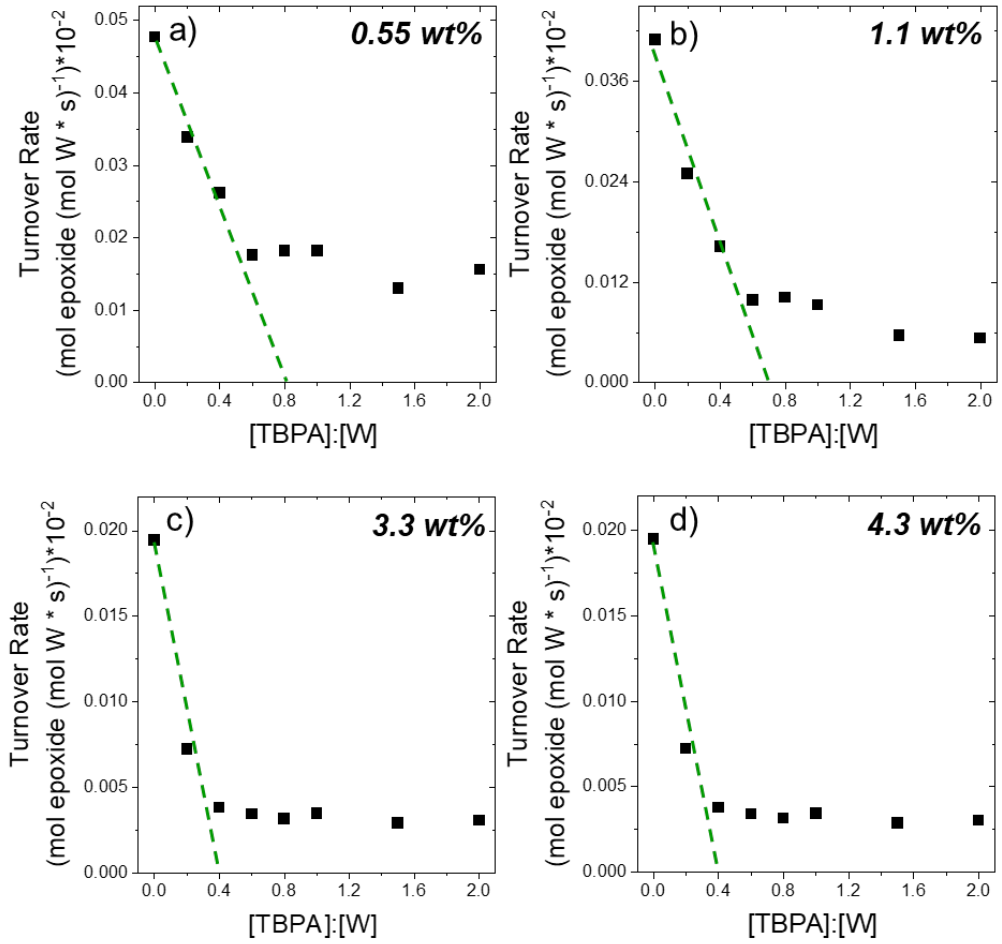

Figure A9. Tert-butyl phosphonic acid titrations of W-BEA with various W loadings (a) 0.55 wt %, (b) 1.1 wt %, (c) 3.3 wt %, and (d) 4.3 wt % during 1-hexene epoxidation with H_2O_2 in CH_3CN (10 mM C_6H_{12}, 1 mM H_2O_2, 39 mM H_2O, in CH_3CN) at 313 K.

Site titrations were performed as discussed in sections 2.2.2 and 2.3.2. As W loading (as measured by EDXRF) increases, percentage of sites active for 1-hexene epoxidation decreases. This is likely due to the tendency of W to oligomerize and form clusters of WO_3 as suggested by increasing band gap (Figure A1) and more intense Raman features for WO_3 (Figure A3) at higher W loadings. The percentage of active W atoms decreases with increasing W loading.

Table A2. Percentage of active W atoms and band gaps for W-BEA with increasing total W content.

W content (wt %)[a]	Metal atoms per unit cell	Band gap (eV)[b]	Active metal (%)[c]
0.55	0.12	4.41	80
1.1	0.23	4.30	70
3.3	0.71	4.13	50
4.3	0.93	4.10	40

[a]measured by EDXRF (Section 2.2.2), [b]determined by DRUV-vis (Section 2.2.2, Figure A1), [c]determined by *in situ* tert-butyl phosphonic acid titrations (Section 2.3.2, Figure A8)

A5. Derivation of Rate Expression for 1-Hexene Epoxidation with H_2O_2 and H_2O_2 Decomposition over M-BEA

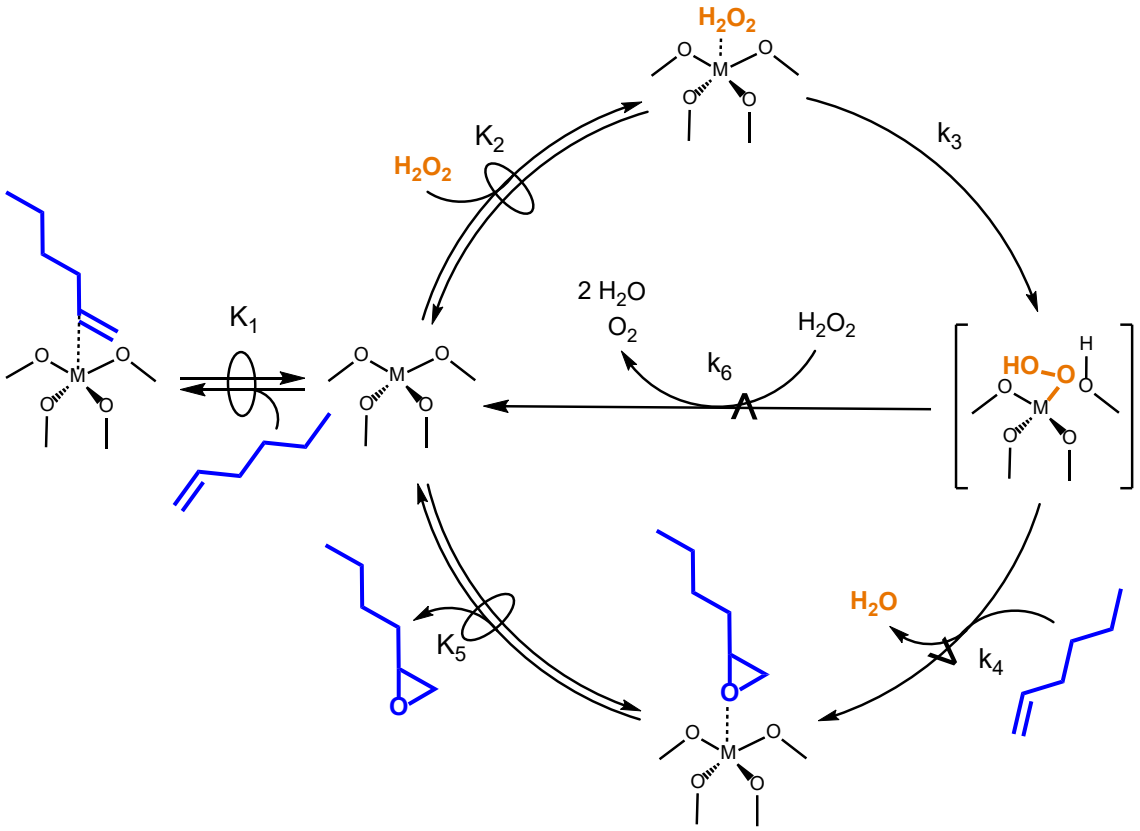

Scheme A1. (from Chapter 2). Proposed mechanism for 1-hexene epoxidation with H_2O_2 and H_2O_2 decomposition depicted for group 4 M-BEA. The ⇳ symbol denotes a quasi-equilibrated step and the A symbol signifies the kinetically relevant steps for the formation of distinct products.

Scheme 2 illustrates a series of elementary steps beginning with the quasi-equilibrated adsorption of 1-hexene (C_6H_{12}) (step 1) and hydrogen peroxide, H_2O_2 (step 2) which is followed by the irreversible activation of H_2O_2 to M-OOH (step 3) or M-(η^2-O_2). Activation of H_2O_2 can result in H_2O_2 decomposition (step 6) or kinetically relevant epoxidation (step 4) by reacting with a H_2O_2 molecule or C_6H_{12} molecule, respectively. The epoxide undergoes quasi-equilibrated adsorption to form 1,2-epoxyhexane [$C_6H_{12}O$] as the product. Measured rates result from the reaction of H_2O-derived surface species with a C_6H_{12} molecule represented by the following equation:

$$r_E = k_4[M-OOH][C_6H_{12}] \quad \text{(A1)}$$

Applying the pseudo-steady state hypothesis to M-OOH species, produces Equation A2:

$$r_E = \frac{k_3\, k_4\, K_2 [C_6H_{12}][H_2O_2][*]}{k_4[C_6H_{12}] + k_6[H_2O_2]} \tag{A2}$$

where r_E is the epoxidation rate, k_4 is the rate constant for step 4 in Scheme 2, and $[M-OOH]$ represents the number of H_2O_2-activated metal sites. The total number of sites, *[L]*, represents all occupied and unoccupied active sites:

$$[L] = [*] + [* C_6H_{12}] + [* H_2O_2] + [* OOH] + [* C_6H_{12}O] \tag{A3}$$

where $[*]$ is the number of unoccupied sites and $[* OOH]$, $[* C_6H_{12}]$, $[* H_2O_2]$, and $[* C_6H_{12}O]$ represent the number of activated H_2O_2, and adsorbed C_6H_{12}, H_2O_2, and $C_6H_{12}O$ respectively. Replacing each term with the associated rate and equilibrium constants, and reactant and product concentrations gives:

$$[L] = 1 + K_1[C_6H_{12}] + K_2[H_2O_2] + \frac{k_3K_2\,[H_2O_2]}{k_4[C_6H_{12}]+k_6[H_2O_2]} + \frac{[C_6H_{12}O]}{K_5} \tag{A4}$$

Bringing together equations A2 and A4 yields the rate expression for $C_6H_{12}O$ formation (equation 2 in Chapter 2):

$$\frac{r_E}{[L]} = \frac{\dfrac{k_3k_4K_2\,[H_2O_2][C_6H_{12}]}{k_4[C_6H_{12}] + k_6[H_2O_2]}}{1 + K_1[C_6H_{12}] + K_2[H_2O_2] + \dfrac{k_3K_2\,[H_2O_2]}{k_4[C_6H_{12}] + k_6[H_2O_2]} + \dfrac{[C_6H_{12}O]}{K_5}} \tag{A5}$$

Similarly, measured rates for H_2O_2 decomposition depend on the reaction between H_2O_2 and M-OOH or M-(η^2-O_2) to produce O_2 and H_2O.

$$r_D = k_6[M-OOH][H_2O_2] \tag{A6}$$

Using the same site balance, *[L]* as above, we define turnover rates for H_2O_2 decomposition as:

$$\frac{r_D}{[L]} = \frac{\dfrac{k_3k_4K_2\,[H_2O_2]^2}{k_4[C_6H_{12}]+k_6[H_2O_2]}}{1+K_1[C_6H_{12}]+K_2[H_2O_2]+\dfrac{k_3K_2\,[H_2O_2]}{k_4[C_6H_{12}]+k_6[H_2O_2]}+\dfrac{[C_6H_{12}O]}{K_5}} \tag{A7}$$

At low of $[C_6H_{12}]$: $[H_2O_2]$, the surface of M-BEA is saturated with species derived from H_2O_2 and rates of H_2O_2 decomposition increase as a linear function of $[H_2O_2]$.[10] The term that represents these species dominates, simplifying the rate expression to:

$$\frac{r_D}{[L]} = k_6[H_2O_2] \quad \text{(A8)}$$

A6. Heats per Injection of 1,2-Epoxyhexane and Thermograms for Isothermal Titration Calorimetry

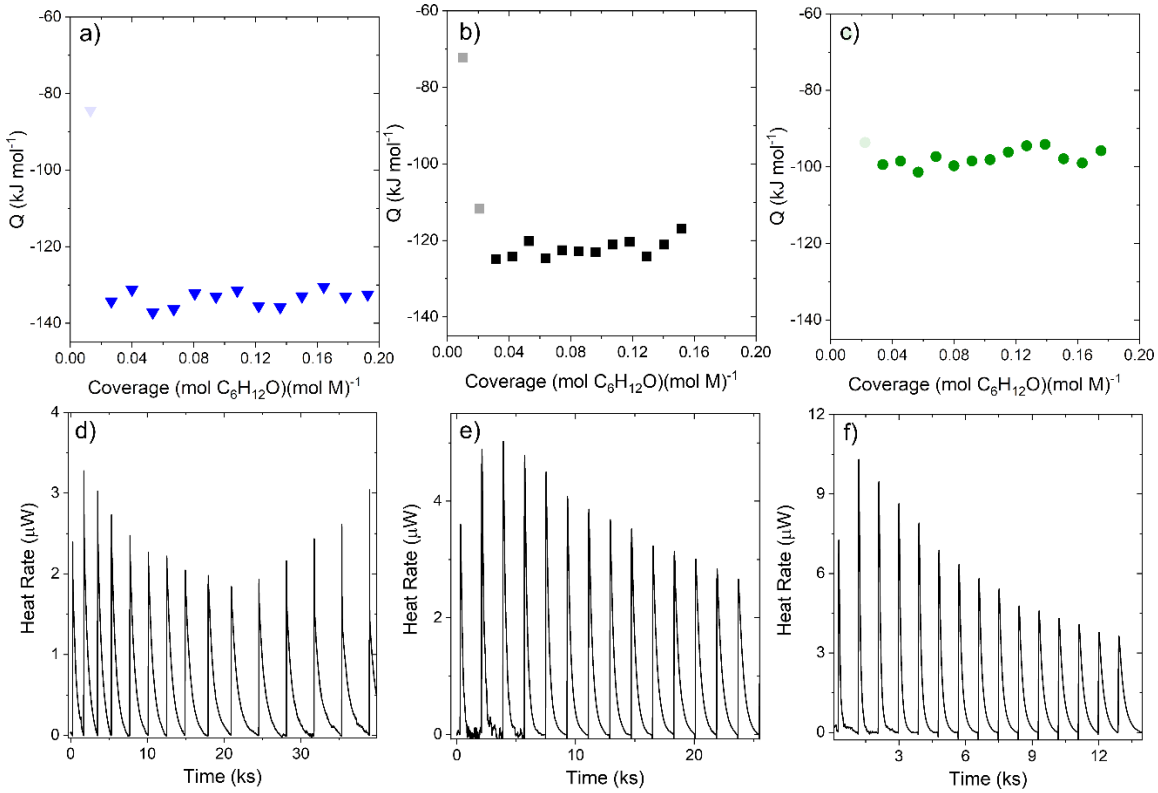

Figure A10. Heats released upon 1,2-epoxyhexane adsorption in CH_3CN (39 mM H_2O, 313 K) on (a) Ti-BEA (▼), (b) Nb-BEA (■), and (c) W-BEA (●) as a function of 1,2-epoxyhexane coverage and associated thermograms for (d) Ti-BEA, (e) Nb-BEA, and (f) W-BEA.

Adsorption enthalpies for 1,2-epoxyhexane ($\Delta H_{ads,epox}$) on M-BEA were measured by isothermal titration calorimetry. Values of $\Delta H_{ads,epox}$ were most negative for Ti-BEA suggesting Ti-BEA adsorbs the epoxide more strongly than Nb-BEA and W-BEA.

Note: The reason for the lower heat value for the initial injection of each thermogram above (Figure A10d-f) is due to the experimental set-up. For each experiment, before the titrant-filled syringe is loaded into the instrument, the tip of the syringe needle is blotted to remove small amount of excess liquid. This blotting, along with natural evaporation, removes a small amount of liquid at the tip of the needle. Moreover, during initial equilibration, diffusion occurs at the liquid at the tip of the needle due to the concentration gradient. This results in the first injection containing less titrant than intended and therefore, noticeable error in the first injection.

A7. Effects of Electronegativity on 1-Hexene Epoxidation Apparent Activation Enthalpies and 1,2-Epoxyhexane Adsorption Enthalpies

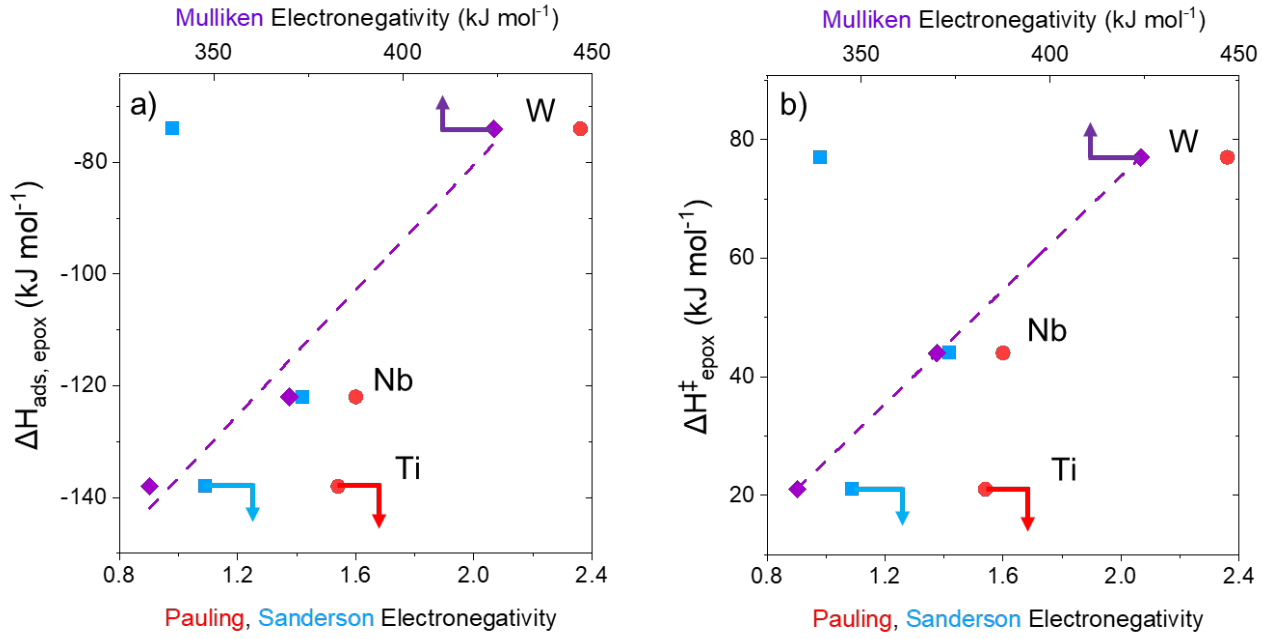

Figure A11. Measured (a) $C_6H_{12}O$ adsorption enthalpies $\Delta H_{ads,epox}$ and (b) apparent activation enthalpies $\Delta H^{\ddagger}_{epox}$ are plotted against Pauling[41] (●), Sanderson (■), and Mulliken electronegativities[105] (♦).

None of the electronegativity scales fit the initial hypothesis that more electronegative metals will lead to the synthesis of more electrophilic sites, and therefore lower activation barriers for epoxidation. However, a linear trend (opposite of our hypothesis) is observed for Mulliken electronegativity (average of electron affinity[174] and first ionization energy[175]) values as a function

of 1-hexene epoxidation enthalpies and 1,2-epoxyhexane adsorption enthalpies on M-BEA. Nb and W are more electronegative than Ti on the Mulliken scale which may explain the greater number of pendant oxygen ligands that form on these metals when they are incorporated into the zeolite BEA framework. However, these ligands ultimately result in a more diffuse electron density, making these oxygen species, some of which are reactive intermediates, less electrophilic. This may explain the higher epoxidation activation enthalpies for the more electronegative Nb and W in BEA and why 1,2-epoxyhexane binds weaker to Nb and W active sites than those of Ti in BEA.

APPENDIX B

SUPPLEMENTAL DATA AND ANALYSIS FOR CHAPTER 3

B1. *Ex situ* Characterization of Ti-MO_x

B1.1 Energy Dispersive X-ray Fluorescence (EDXRF) to Measure Residual Cl Content

Table B1. Cl Content of Metal Oxide Supports as Received and After Ti Grafting

MO_x	Cl content (wt %) (as-received)	Cl content (wt%) (following complete synthesis procedure)
ZnO	0.58 ± 0.02	0.77 ± 0.03
Al_2O_3	0.18 ± 0.01	0.16 ± 0.01
SiO_2	0.26 ± 0.01	0.26 ± 0.01
GeO_2	0.12 ± 0.00	0.10 ± 0.00

Table B1 shows results of elemental analyses of the metal oxide supports using EDXRF. The data show negligible differences between the chlorine content of the as-received metal oxide supports and the fully synthesized catalysts (i.e., after grafting Ti atoms and performing oxidative treatments), which indicates the titanocene dichloride precursor does not add persistent chlorine to the surface of the catalyst.

B1.2 Diffuse Reflectance UV-Vis Spectra of Ti-MO_x

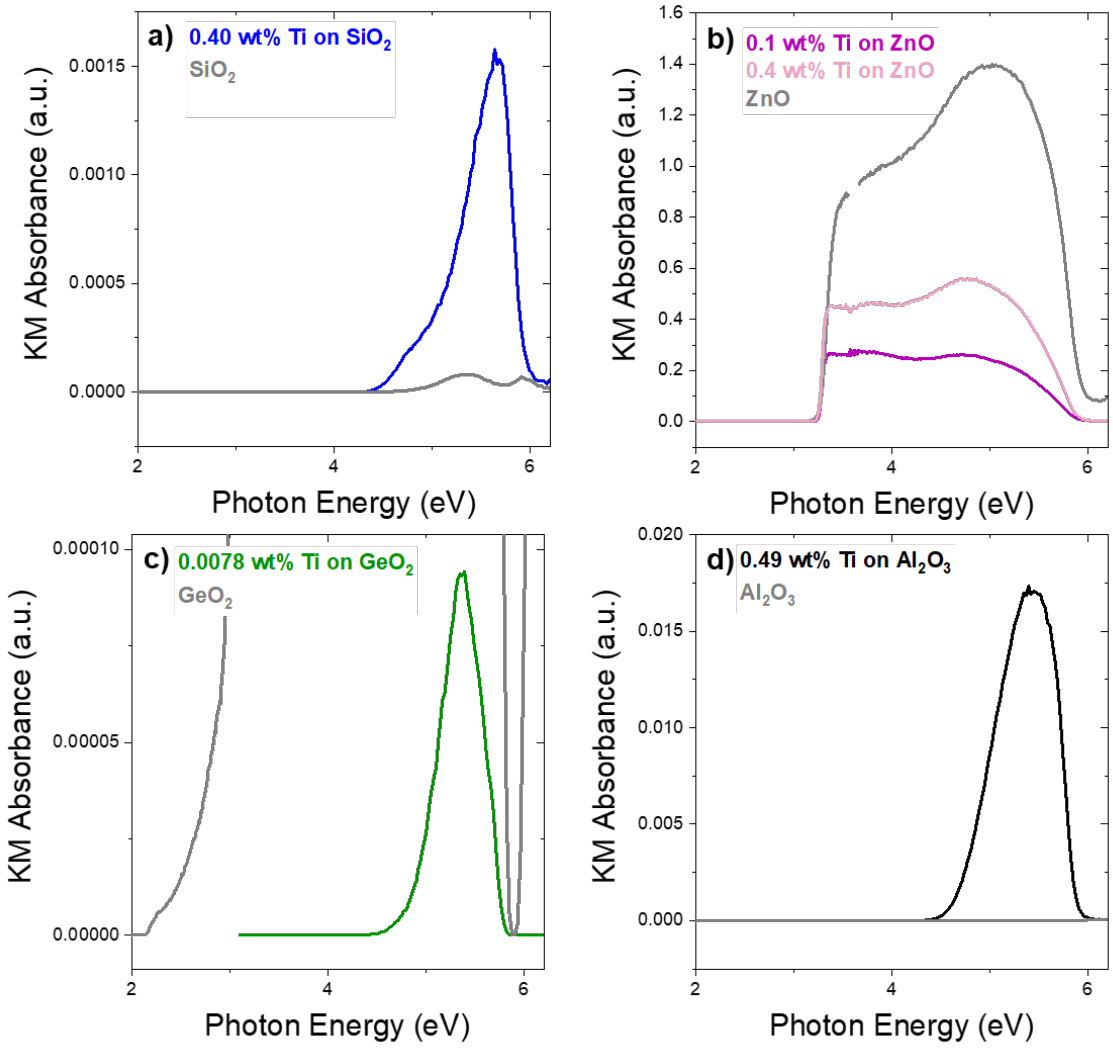

Figure B1. Tauc plots for (a) Ti-SiO_2 (blue, 0.55 wt %), (b) Ti-ZnO (purple, 0.017 wt %), (c) Ti-GeO_2 (green, 0.006 wt %), and (d) Ti-Al_2O_3 (black, 0.49 wt %).

Table B2. Ti loading and band gap for Ti-MO_x

Catalyst	Ti loading (%)	Band gap (eV)
Ti-SiO_2	0.40	4.87
Ti-ZnO	0.017	-
Ti-GeO_2	0.0078	4.81
Ti-Al_2O_3	0.49	4.67

B2. *In situ* Characterization of Ti-MO_x

B2.1 Hot Filtration to Check for Leaching of Ti from MO_x Supports

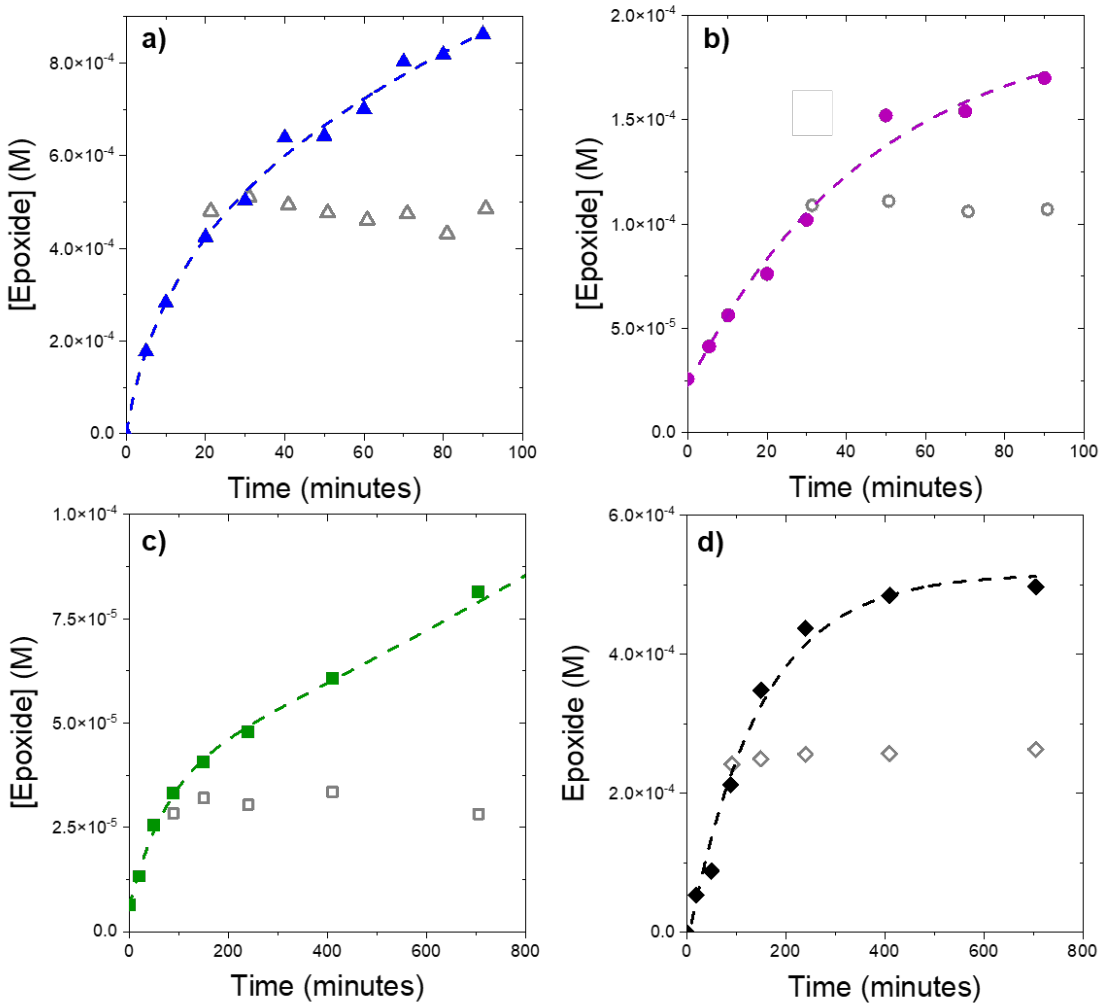

Figure B2. Measured 1,2-epoxyhexane concentration over time for (a) Ti-SiO_2 (blue triangles, 0.1 M C_6H_{12}, 0.01 M H_2O_2 in CH_3CN), (b) Ti-ZnO (purple circles, 0.5 M C_6H_{12}, 0.01 M H_2O_2 in CH_3CN), (c) Ti-GeO_2 (green squares, 0.5 M C_6H_{12}, 0.01 M H_2O_2 in CH_3CN), and (d) Ti-Al_2O_3, (black diamonds, 0.5 M C_6H_{12}, 0.01 M H_2O_2 in CH_3CN). Hollow grey data points indicate the 1,2-epoxyhexane concentration over time in an aliquot from which the catalyst was filtered using a syringe filter (0.05 μm) collected from the original reaction solution.

Results for hot filtration experiments are displayed in Figure B2 and indicate that no Ti species active for epoxidation leach from the support under reaction conditions. Additionally, EDXRF experiments show no difference in Ti content before and after reaction, corroborating these findings.

B2.2 Comparisons of 1-Hexene Epoxidation Rates Between Ti Grafted MO_x and Bare Supports

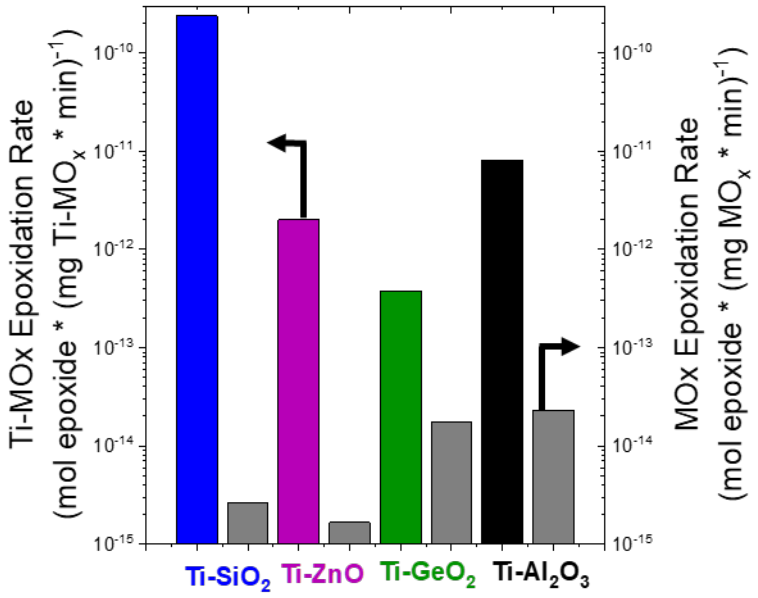

Figure B3. Rates for 1-hexene epoxidation with H_2O_2 (0.5 M C_6H_{12}, 0.01 M H_2O_2, 3.9 mM H_2O in CH_3CN, 313 K) for Ti-SiO_2 (blue), Ti-ZnO (purple), Ti-GeO_2 (green), Ti-Al_2O_3 (black) and corresponding bare metal oxide (gray) normalized by total mass of catalyst added (~500 mg).

Figure B3 demonstrates that we can differentiate the catalytic activity of grafted Ti atoms from the metal oxide support to report accurate turnover rates for epoxidation.

B2.3 Turnover Rates versus [H_2O] for Ti-SiO_2 and Ti-Al_2O_3

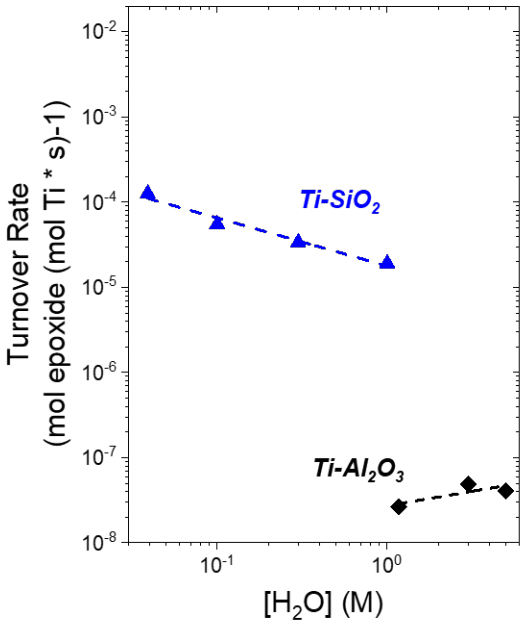

Figure B4. Turnover rates for 1-hexene epoxidation with H_2O_2 over Ti-SiO_2 (0.5 mM C_6H_{12}, 0.3 M H_2O_2 in CH_3CN, 313 K) and Ti-Al_2O_3 (0.5 mM C_6H_{12}, 0.3 M H_2O_2 in CH_3CN, 313 K).

Figure B4 shows that varying [H_2O] changes rates considerably on Ti-SiO_2 (r~ $[H_2O]^{-0.6}$) and has a weak positive effect on rates for Ti-Al_2O_3 (r~ $[H_2O]^{0.4}$). These relationships appear to agree with values for the rate constant (k_4) reflecting the [H_2O] through excess contributions to activation barriers than the direct involvement of H_2O molecules in the elementary steps.

B2.4 *In situ* UV-Vis Spectra for H_2O_2 Activation Ti-MO_x

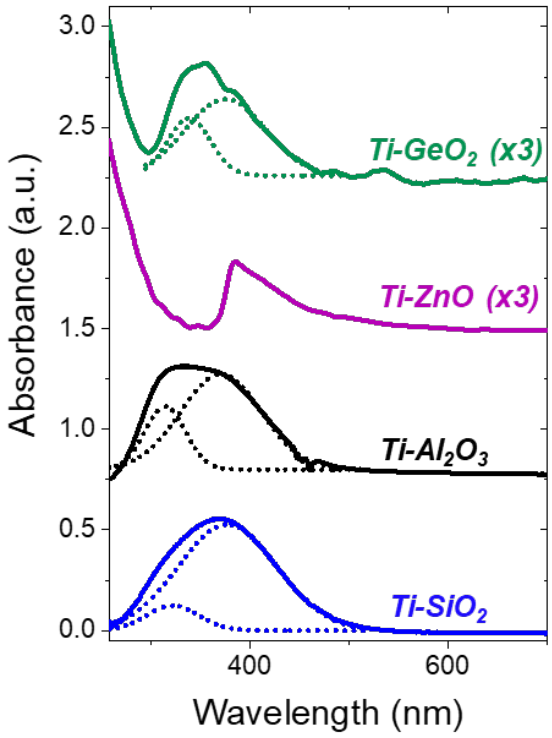

Figure B5. *In situ* UV-Vis spectra for Ti-SiO_2 (blue, 0.40 wt %), Ti-ZnO (purple, 0.017 wt %), Ti-GeO_2 (green, 0.0078 wt %), and Ti-Al_2O_3 (black, 0.49 wt %) while flowing a solution of H_2O_2 (10 mM (Ti-SiO_2), 50 mM (Ti-ZnO, Ti-GeO_2, Ti-Al_2O_3) H_2O_2, 39 mM H_2, in CH_3CN, 1 ml min^{-1}) at 313 K.

Figure B5 displays steady-state UV-Vis spectra of reactive intermediates formed on Ti-MO_x materials when H_2O_2 is activated *in situ* (10-50 mM H_2O_2, 39 mM H_2, in CH_3CN, 1 ml min^{-1}) at 313 K. Spectra are deconvoluted using OriginPro Software by subtracting a baseline and fitting Gaussian functions to two features (fixed baseline at 0, initial guesses for peak positions are determined by literature values for ligand-to-metal charge transfer (LMCT) energies of Ti-(η^2-O_2) and Ti-OOH). These features represent the individual contributions of Ti-(η^2-O_2) and Ti-OOH surface intermediates formed on supported Ti atoms and determine the LMCT energies of reactive oxygen ligands. Ti-(η^2-O_2) species absorb photons at higher energies (shorter λ) than Ti-OOH species.[72, 74, 125] These results demonstrate that there is no observable difference between LMCT energies for reactive oxygen ligands bound to Ti atoms supported on SiO_2, GeO_2, Al_2O_3, or ZnO.

Notably, the spectrum for Ti-ZnO spans only half of the range of wavelengths as the other three catalysts, which may suggest Ti-OOH species are most prevalent on this material.

Table B3. Ligand-to-metal charge transfer (LMCT) energies for Ti-OOH supported on MO_x

Catalyst	Ligand-to-metal charge transfer energies for Ti-OOH (eV)
Ti-SiO_2	3.28
Ti-ZnO	3.13
Ti-GeO_2	3.22
Ti-Al_2O_3	3.33

B2.5 *In situ* Raman Spectra for H_2O_2 Activation on Ti-MO_x

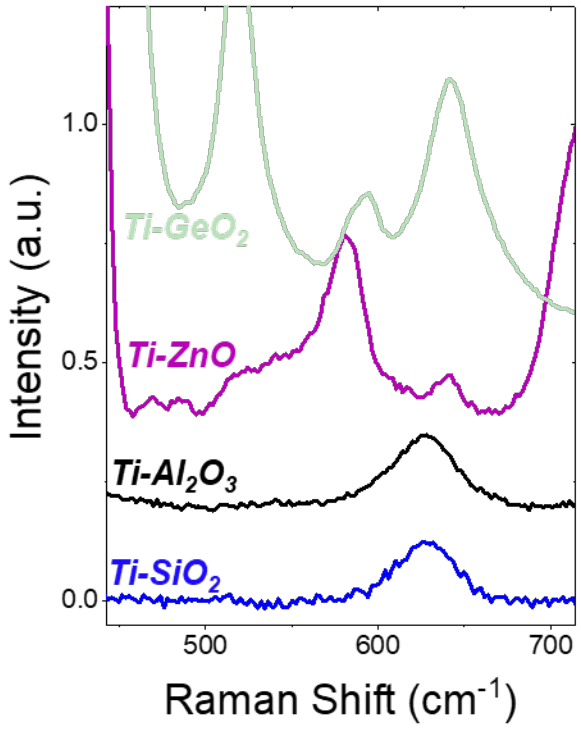

Figure B6. *In situ* Raman spectra (442 nm laser, 0.8 mW μm^{-2}) of (a) Ti-SiO_2 (blue, 0.40 wt %), (b) Ti-ZnO (purple, 0.017 wt %), (c) Ti-GeO_2 (green, 0.0078 wt %), and (d) Ti-Al_2O_3 (black, 0.49 wt %) while flowing a solution of H_2O_2 (10 mM (Ti-SiO_2), 50 mM (Ti-ZnO, Ti-GeO_2, Ti-Al_2O_3) H_2O_2, 39 mM H_2, in CH_3CN, 1 ml min^{-1}) at 313 K.

The *in situ* steady state Raman spectra collected while flowing 10 – 50 mM H_2O_2 in CH_3CN at 313 K for Ti-SiO_2, Ti-Al_2O_3, and Ti-ZnO all exhibit a peak between 628 – 640 cm^{-1} which indicates the formation of Ti-(η^2-O_2) moieties on the surface.[72] This Raman vibrational range is narrow compared to the differences (550 – 620 cm^{-1}) measured for Ti-(η^2-O_2), Nb-(η^2-O_2), and W-(η^2-O_2) features when Ti, Nb, and W are incorporated into the siliceous zeolite BEA framework.[9] This suggests that changing the identity of the support does not affect covalent interactions to the same extent as changing the identity of the active transition metal, further supporting conclusions from *in situ* UV-Vis experiments in B2.3.

Note: Ti-ZnO also contains feature representative of bare ZnO.[176, 177] Bending modes characteristic of GeO_2 can be observed in the broad region between 500-650 cm^{-1} and obscure potential features that would represent Ti-OOH, hindering us from making comparisons for Ti-GeO_2 catalysts.[126, 127]

B2.6 Derivation of Rate Expression for 1-Hexene Epoxidation with H_2O_2 and H_2O_2 Decomposition over Ti-MO_x

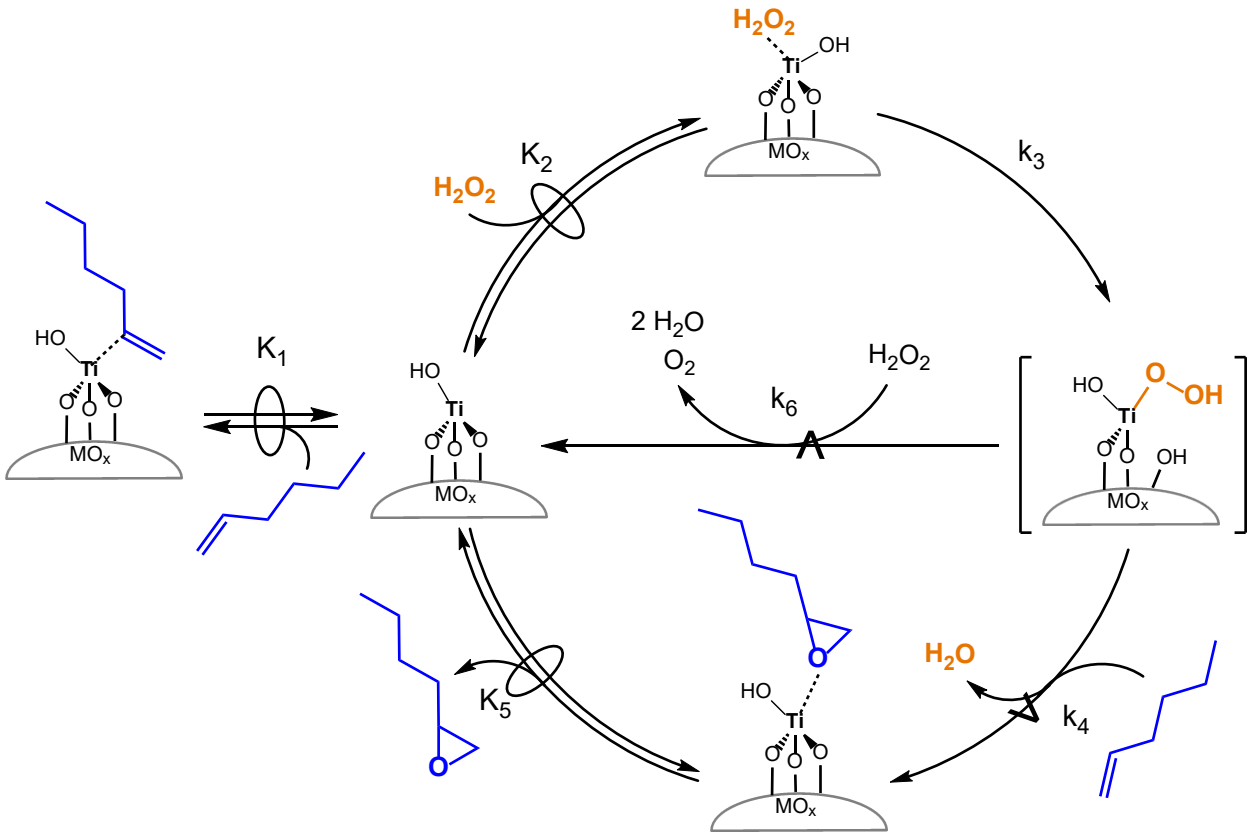

Scheme B1. (Reproduced from the Chapter 3) Proposed mechanism for 1-hexene epoxidation with H_2O_2 and H_2O_2 decomposition over Ti-MO_x. The ⇳ symbol denotes a quasi-equilibrated step and the ⇸ symbol signifies the kinetically relevant steps for the formation of products. Solvent molecules have been excluded for clarity.

The series of elementary steps for 1-hexene epoxidation over Ti-MO_x is initiated with the quasi-equilibrated adsorption of 1-hexene (C_6H_{12}) (step 1) and hydrogen peroxide, H_2O_2 (step 2). Next, the irreversible activation of H_2O_2 leads to the formation of titanium-hydroperoxo (Ti-OOH) (step 3) or titanium-peroxo (Ti-(η^2-O_2)) reactive species and can result in H_2O_2 decomposition by reacting with H_2O (step 6) or kinetically relevant oxygen transfer to C_6H_{12} (step 4). The quasi-equilibrated desorption of the epoxide to form 1,2-epoxyhexane [$C_6H_{12}O$] concludes the cycle. The following equation represents the measured rates for the reaction of H_2O-derived surface species with a C_6H_{12} molecule:

$$r_E = k_4[Ti - OOH][C_6H_{12}] \quad \text{(B1)}$$

We apply the pseudo-steady state hypothesis to Ti-OOH species to produce Equation B2:

$$r_E = \frac{k_3\, k_4\, K_2[C_6H_{12}][H_2O_2][*]}{k_4[C_6H_{12}]+k_6[H_2O_2]} \tag{B2}$$

where r_E is the epoxidation rate, k_4 is the rate constant for step 4 in Scheme B1, and $[Ti-OOH]$ represents the number of H_2O_2-activated metal sites. The total number of sites, *[L]*, corresponds to the sum of all possible surface occupancy states for active sites:

$$[L] = [*] + [* C_6H_{12}] + [* H_2O_2] + [* OOH] + [* C_6H_{12}O] \tag{B3}$$

where $[*]$ is the number of solvent occupied sites and $[* OOH]$, $[* C_6H_{12}]$, $[* H_2O_2]$, and $[* C_6H_{12}O]$ represent the number of sites occupied by activated H_2O_2, and molecularly adsorbed C_6H_{12}, H_2O_2, and $C_6H_{12}O$, respectively. Replacing each term with the corresponding rate and equilibrium constants, and reactant and product concentrations gives:

$$[L] = 1 + K_1[C_6H_{12}]+ K_2[H_2O_2] + \frac{k_3K_2\,[H_2O_2]}{k_4[C_6H_{12}]+k_6[H_2O_2]} + \frac{[C_6H_{12}O]}{K_5} \tag{B4}$$

Bringing together equations B2 and B4 yields the rate expression for $C_6H_{12}O$ formation (equation 3.2 in Chapter 3):

$$\frac{r_E}{[L]} = \frac{\frac{k_3k_4K_2\,[H_2O_2][C_6H_{12}]}{k_4[C_6H_{12}]+k_6[H_2O_2]}}{1+K_1[C_6H_{12}]+ K_2[H_2O_2]+\frac{k_3K_2\,[H_2O_2]}{k_4[C_6H_{12}]+k_6[H_2O_2]}+\frac{[C_6H_{12}O]}{K_5}} \tag{B5}$$

Similarly, measured rates for H_2O_2 decomposition depend on the reaction between H_2O_2 and M-OOH or M-(η^2-O_2) to produce O_2 and H_2O.

$$r_D = k_6[Ti-OOH][H_2O_2] \tag{B6}$$

Using the same site balance, *[L]* in Equation B4, we describe turnover rates for H_2O_2 decomposition as:

$$\frac{r_D}{[L]} = \frac{\frac{k_3 k_4 K_2 [H_2O_2]^2}{k_4[C_6H_{12}]+k_6[H_2O_2]}}{1+K_1[C_6H_{12}]+ K_2[H_2O_2]+\frac{k_3 K_2 [H_2O_2]}{k_4[C_6H_{12}]+k_6[H_2O_2]}+\frac{[C_6H_{12}O]}{K_5}} \quad \text{(B7)}$$

At low of $[C_6H_{12}]$: $[H_2O_2]$, the surface of Ti-MO_x is saturated with species derived from H_2O_2 and rates of H_2O_2 decomposition increase as a linear function of $[H_2O_2]$. The term that represents these species dominates, simplifying the rate expression to:

$$\frac{r_D}{[L]} = k_6[H_2O_2] \quad \text{(B8)}$$

B2.7 Eyring Plots for 1-Hexene Epoxidation and H_2O_2 Decomposition over Ti-MO_x

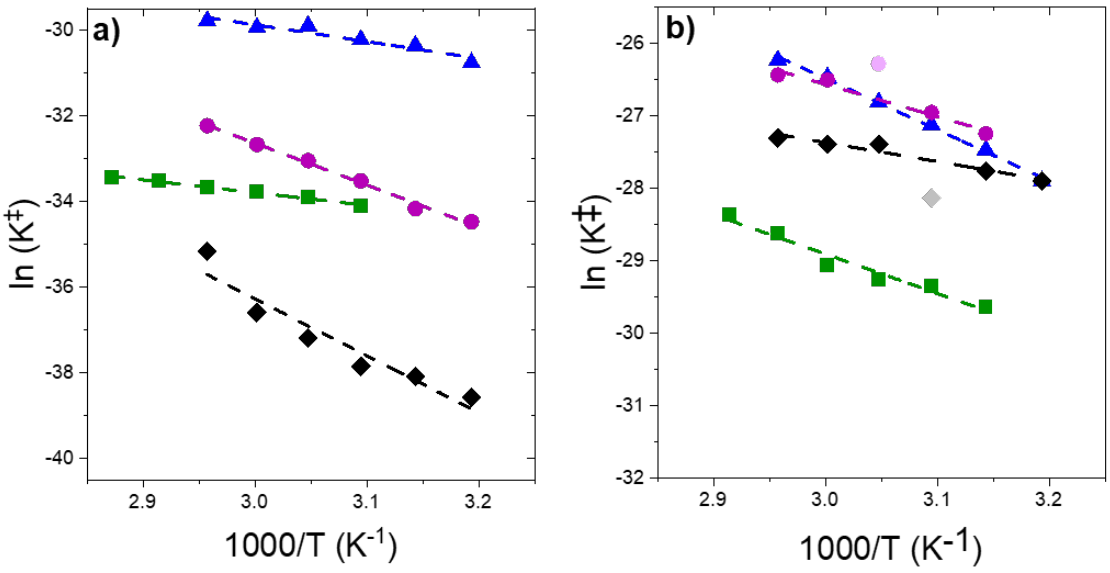

Figure B7. Natural logs of transition state constants as functions of inverse temperature for (a) Ti-SiO_2 (blue triangles, 0.5 mM C_6H_{12}, 0.01 M H_2O_2 in CH_3CN), (b) Ti-ZnO (purple circles, 0.5 mM C_6H_{12}, 0.01 M H_2O_2 in CH_3CN), (c) Ti-GeO_2 (green squares, 0.5 mM C_6H_{12}, 0.01 M H_2O_2 in CH_3CN), and (d) Ti-Al_2O_3, (black diamonds, 0.5 mM C_6H_{12}, 0.01 M H_2O_2 in CH_3CN).

Values of $\Delta H^{\ddagger}_{epox}$, $\Delta S^{\ddagger}_{epox}$, $\Delta H^{\ddagger}_{decomp}$, and $\Delta S^{\ddagger}_{decomp}$ were determined by fitting measured rates to temperature values using the relationships below.

$$K^{\ddagger}_{epox} = \exp\left(-\frac{\Delta H^{\ddagger}_{epox}}{RT}\right)\exp\left(\frac{\Delta S^{\ddagger}_{epox}}{R}\right) \tag{B9}$$

$$K^{\ddagger}_{decomp} = \exp\left(-\frac{\Delta H^{\ddagger}_{decomp}}{RT}\right)\exp\left(\frac{\Delta S^{\ddagger}_{decomp}}{R}\right) \tag{B10}$$

$$\frac{r}{[L]} = \frac{k_B T}{h}\cdot\exp\left(-\frac{\Delta H^{\ddagger}_{epox}}{RT}\right)\exp\left(\frac{\Delta S^{\ddagger}_{epox}}{R}\right)[C_6H_{12}] \tag{B11}$$

$$\frac{r}{[L]} = \frac{k_B T}{h}\cdot\exp\left(-\frac{\Delta H^{\ddagger}_{decomp}}{RT}\right)\exp\left(\frac{\Delta S^{\ddagger}_{decomp}}{R}\right)[H_2O_2] \tag{B12}$$

where $K^{\ddagger}_{epox}$ and $K^{\ddagger}_{decomp}$ are the transition state equilibrium constants for epoxidation and decomposition, respectively, k_B is the Boltzmann's constant, h is Planck's constant, R is the ideal gas constant, and T is temperature.

Table B4. Apparent activation enthalpies ($\Delta H^{\ddagger}_{epox}$, $\Delta H^{\ddagger}_{decomp}$) and entropies ($\Delta S^{\ddagger}_{epox}$. $\Delta S^{\ddagger}_{decomp}$) for epoxidation and hydrogen peroxide decomposition

Catalyst	$\Delta H^{\ddagger}_{epox}$ (kJ mol^{-1})	$\Delta S^{\ddagger}_{epox}$ (J K^{-1} mol^{-1})	$\Delta H^{\ddagger}_{decomp}$ (kJ mol^{-1})	$\Delta S^{\ddagger}_{decomp}$ (J K^{-1} mol^{-1})
Ti-SiO_2	33 ± 5	-150 ± 15	59 ± 2	-44 ± 6
Ti-ZnO	81 ± 3	-27 ± 10	29 ± 1	-132 ± 2
Ti-GeO_2	25 ± 2	-207 ± 4	45 ± 5	-105 ± 14
Ti-Al_2O_3	110 ± 17	-29 ± 52	22 ± 3	-162 ± 9

APPENDIX C

SUPPLEMENTAL DATA AND ANALYSIS FOR CHAPTER 4

C1. *Ex situ* and *In situ* Characterization of Ti-BEA

C1.1 X-Ray Diffraction Spectroscopy of deAl-BEA and Ti-BEA

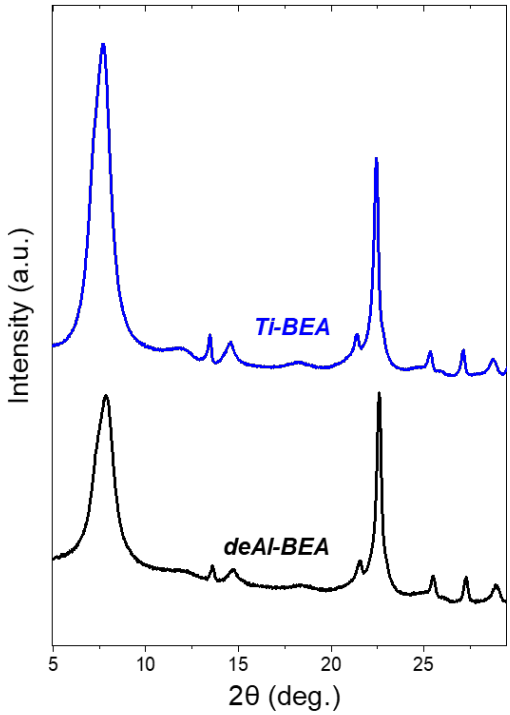

Figure C1. Powder X-ray diffractograms for dealuminated BEA (deAl-BEA, black) and 0.22 wt % Ti-BEA (blue) collected under ambient conditions.

No differences are observed between XRD peak locations which indicate the crystalline framework structure of BEA remains intact after Ti atom incorporation.[170]

C1.2 Diffuse Reflectance UV-Vis Spectra of Ti-MO_x

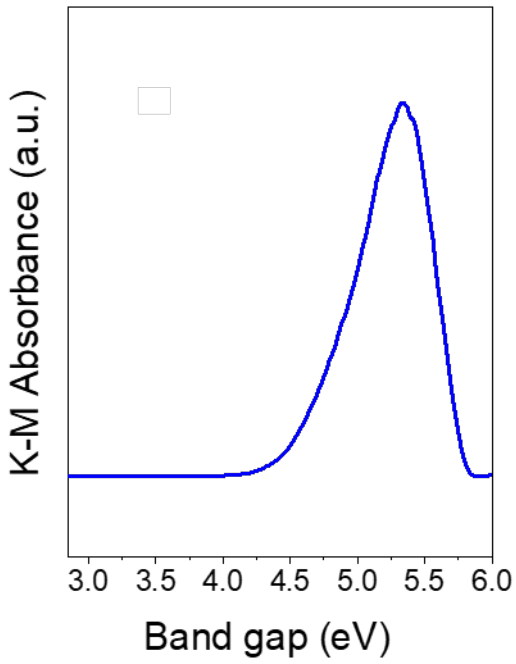

Figure C2. Tauc plot for Ti-BEA (0.22 wt %). Reflectance measured under ambient conditions.

The minimum metal band gap measured for the Ti-BEA catalyst used in this study is 4.35 eV, much greater than the value for bulk TiO_2 (3.2 eV) which indicates relatively disperse Ti species on the catalyst surface. Further evidence for isolated Ti sites, synthesized using the same post-synthetic modification procedure, comes from in situ active site titrations which demonstrates catalytically equivalent active sites with uniform access to nearby alkene molecules and is found in a previous study.[9]

C2. Kinetic and Thermodynamic Analysis for Alkene Epoxidation over Ti-BEA

C2.1 Calculation of Carbon Balance

The carbon balance, C, for the reaction of alkene was calculated using Equation C1.

$$C = \frac{n*F_{out}}{n*F_{in}} = \frac{\sum\left(nF_{CnH2n,out}+nF_{CnH2nO}+2F_{acetaldehyde}+3F_{propionaldehyde}+F_{formaldehyde}\right)}{nF_{CnH2n,in}} \quad \text{(C1)}$$

Where $F_{in}$is the molar flow rate of alkene molecules entering the reactor, F_{out} is the molar flow rate of alkene-derived molecules leaving the reactor, $F_{CnH2n,in}$ is the molar flow rate of alkene at the reactor inlet, $F_{CnH2n,out}$ is the molar flow rate of alkene at the reactor outlet, $F_i$are the molar flow rates of all alkene-derived components, some detected by the GC-FID.

Table C1. Carbon balance for all alkenes under similar reaction conditions

Reactant	Carbon Balance (%)
C_3H_6	95 ± 5 [a]
C_4H_8	98 ± 1 [b]
C_6H_{12}	86 ± 5 [c]
C_8H_{16}	64 ± 4 [d]
$C_{10}H_{20}$	72 ± 3 [e]

[a](0.13 kPa C_3H_6, 1.6 kPa H_2O_2, 10.3 kPa CH_3CN in He, 383 K), [b](0.075 kPa C_4H_8, 1.6 kPa H_2O_2, 10.3 kPa CH_3CN in He, 383 K), [c](0.1 kPa C_6H_{12}, 1.6 kPa H_2O_2, 10.3 kPa CH_3CN in He, 383 K), [d](0.065 kPa C_8H_{16}, 1.6 kPa H_2O_2, 10.3 kPa CH_3CN in He, 383 K), [e] (0.075 kPa $C_{10}H_{20}$, 1.6 kPa H_2O_2, 10.3 kPa CH_3CN in He, 383 K)

C2.2 Turnover rates for Propene, Butene, and Decene Epoxidation over Ti-BEA as Functions of [H_2O_2]

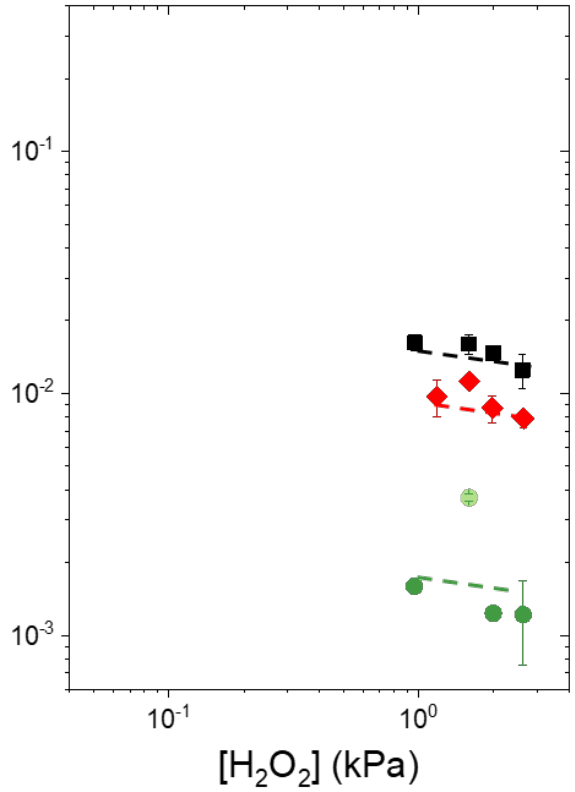

Figure C3. Turnover rates over Ti-BEA as functions of [H_2O_2] (0.13 kPa C_3H_6, 0.97 kPa $C_{10}H_{20}$, 10.3 kPa CH_3CN in 90 SCCM He, 383 K).

Figure C3 shows no dependence on oxidant pressure at low [C_nH_{2n}]:[H_2O_2] indicating a MARI derived from the oxidant, consistent with the rate expression derived below in Section C2.2.

C2.3 Derivation of Rate Expression for Alkene Epoxidation with H_2O_2 and H_2O_2 Decomposition over Ti-BEA

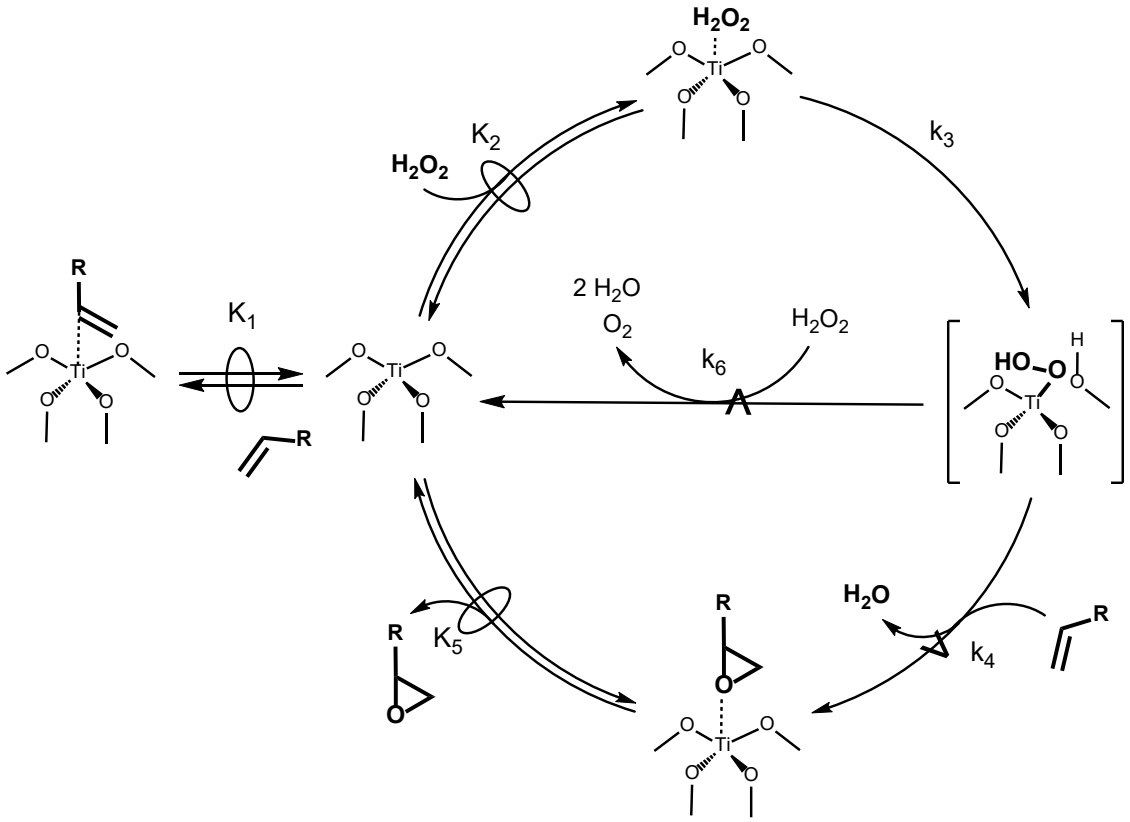

Scheme C1. (Reproduced from Chapter 4) Proposed mechanism for alkene epoxidation with H_2O_2 and H_2O_2 decomposition over Ti-BEA. The ⇌ symbol represents a quasi-equilibrated step and the ⇀ symbol signifies the kinetically relevant steps for the formation of products. Solvent molecules have been excluded for clarity.

Scheme C1 illustrates the elementary steps for alkene epoxidation over Ti-BEA and begins with the quasi-equilibrated adsorption of alkene (step 1) and hydrogen peroxide, H_2O_2 (step 2). Next, the irreversible activation of H_2O_2 forms titanium-hydroperoxo (Ti-OOH) (step 3) or titanium-peroxo (Ti-(η^2-O_2)) reactive species followed by H_2O_2 decomposition through reaction with H_2O (step 6) or kinetically relevant oxygen transfer to C_nH_{2n} (step 4). The cycle is complete

with quasi-equilibrated desorption of the epoxide [$C_nH_{2n}O$]. Equation C2 represents the measured rates for the reaction of H_2O_2-derived surface oxygen species with an alkene molecule:

$$r_E = k_4[Ti - OOH][C_nH_{2n}] \quad \text{(C2)}$$

The application of the pseudo-steady state hypothesis to Ti-OOH species produces Equation C2:

$$r_E = \frac{k_3\, k_4\, K_2[C_nH_{2n}][H_2O_2][*]}{k_4[C_nH_{2n}]+k_6[H_2O_2]} \quad \text{(C3)}$$

where r_E is the epoxidation rate, k_4 is the rate constant for step 4 in Scheme C1, and $[Ti - OOH]$ represents the number of H_2O_2-activated metal sites. The total number of sites, *[L]*, corresponds to the sum of all possible surface occupancy states for active sites:

$$[L] = [*] + [* C_nH_{2n}] + [* H_2O_2] + [* OOH] + [* C_nH_{2n}O] \quad \text{(C4)}$$

where $[*]$ is the number of solvent occupied sites and $[* OOH]$, $[* C_nH_{2n}]$, $[* H_2O_2]$, and $[* C_nH_{2n}O]$ represent the number of sites occupied by activated H_2O_2, and molecularly adsorbed C_nH_{2n}, H_2O_2, and $C_nH_{2n}O$, respectively. Replacing each term with the corresponding rate and equilibrium constants, and reactant and product concentrations gives:

$$[L] = 1 + K_1[C_nH_{2n}]+ K_2[H_2O_2] + \frac{k_3K_2\,[H_2O_2]}{k_4[C_nH_{2n}]+k_6[H_2O_2]} + \frac{[C_nH_{2n}O]}{K_5} \quad \text{(C5)}$$

Bringing together equations C3 and C5 yields the rate expression for $C_nH_{2n}O$ formation (equation 4.2 in Chapter 4):

$$\frac{r_E}{[L]} = \frac{\frac{k_3k_4K_2\,[H_2O_2][C_nH_{2n}]}{k_4[C_nH_{2n}]+k_6[H_2O_2]}}{1+K_1[C_nH_{2n}]+ K_2[H_2O_2]+\frac{k_3K_2\,[H_2O_2]}{k_4[C_nH_{2n}]+k_6[H_2O_2]}+\frac{[C_nH_{2n}O]}{K_5}} \quad \text{(C6)}$$

Similarly, measured rates for H_2O_2 decomposition depend on the reaction between H_2O_2 and Ti-OOH or Ti-(η^2-O_2) to produce O_2 and H_2O.

$$r_D = k_6[Ti - OOH][H_2O_2] \quad \text{(C7)}$$

Using the same site balance, *[L]* in Equation C5, we describe turnover rates for H_2O_2 decomposition as:

$$\frac{r_D}{[L]} = \frac{\frac{k_3 k_4 K_2 [H_2O_2]^2}{k_4[C_nH_{2n}]+k_6[H_2O_2]}}{1+K_1[C_nH_{2n}]+K_2[H_2O_2]+\frac{k_3 K_2 [H_2O_2]}{k_4[C_nH_{2n}]+k_6[H_2O_2]}+\frac{[C_nH_{2n}O]}{K_5}} \quad \text{(C8)}$$

At low of $[C_nH_{2n}]$: $[H_2O_2]$, the surface of Ti-BEA is saturated with species derived from H_2O_2 and rates of H_2O_2 decomposition increase as a linear function of $[H_2O_2]$. The term that represents these species dominates, simplifying the rate expression to:

$$\frac{r_D}{[L]} = k_6[H_2O_2] \quad \text{(C9)}$$

C2.4 Eyring and Compensation Plots for Alkene Epoxidation over Ti-BEA

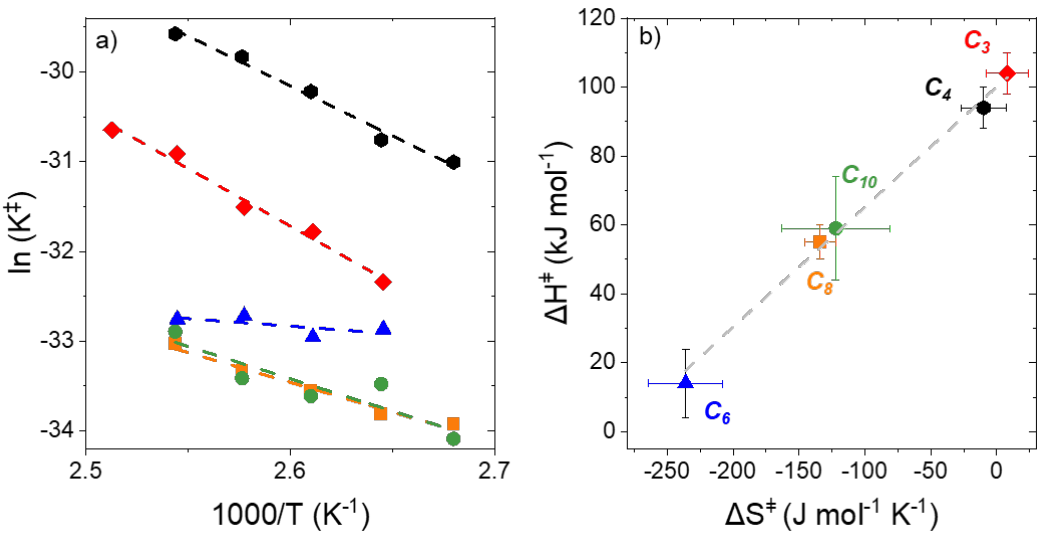

Figure C4. (a) Natural logs of transition state constants as functions of inverse temperature and (b) $\Delta H^{\ddagger}_{epox}$ as a function of $\Delta S^{\ddagger}_{epox}$ for C_3H_6 (red diamonds, 0.13 kPa C_3H_6, 1.6 kPa H_2O_2, 10.3 kPa CH_3CN in He, 373-393 K), C_4H_8 (black hexagons, 0.075 kPa C_4H_8, 1.6 kPa H_2O_2, 10.3 kPa CH_3CN in He, 373-393 K), C_6H_{12} (blue triangles, 0.1 kPa C_6H_{12}, 1.6 kPa H_2O_2, 10.3 kPa CH_3CN in He, 373-393 K), C_8H_{16} (orange squares, 0.065 kPa C_8H_{16}, 1.6 kPa H_2O_2, 10.3 kPa CH_3CN in He, 373-393 K), and $C_{10}H_{20}$ (green circles, 0.075 kPa $C_{10}H_{20}$, 1.6 kPa H_2O_2, 10.3 kPa CH_3CN in He, 373-393 K).

Values of $\Delta H^{\ddagger}_{epox}$ and $\Delta S^{\ddagger}_{epox}$ were determined by fitting measured rates to temperature values using the relationships below.

$$K^{\ddagger}_{epox} = \exp\left(-\frac{\Delta H^{\ddagger}_{epox}}{RT}\right)\exp\left(\frac{\Delta S^{\ddagger}_{epox}}{R}\right) \quad \text{(C10)}$$

$$\frac{r}{[L]} = \frac{k_B T}{h}\cdot \exp\left(-\frac{\Delta H^{\ddagger}_{epox}}{RT}\right)\exp\left(\frac{\Delta S^{\ddagger}_{epox}}{R}\right)[C_n H_{2n}] \quad \text{(C11)}$$

where $K^{\ddagger}_{epox}$ is the transition state equilibrium constant for epoxidation, k_B is the Boltzmann's constant, h is Planck's constant, R is the ideal gas constant, and T is temperature.

Table C2. Apparent activation enthalpies ($\Delta H^{\ddagger}_{epox}$) and entropies ($\Delta S^{\ddagger}_{epox}$) for epoxidation

Alkene	$\Delta H^{\ddagger}_{epox}$ (kJ mol^{-1})	$\Delta S^{\ddagger}_{epox}$ (J K^{-1} mol^{-1})
C_3H_6	104 ± 6	8 ± 16
C_4H_8	94 ± 6	-10 ± 17
C_6H_{12}	14 ± 10	-236 ± 28
C_8H_{16}	55 ± 5	-134 ± 12
$C_{10}H_{20}$	59 ± 15	-122 ± 41

C3. FT-Infrared Spectroscopy

C3.1 Calculation of CH_3CN Extinction Coefficient

Applying the Beer-Lambert relationship, we determine the extinction coefficient, ϵ, for vapor-phase CH_3CN.

$$Abs_{\nu(C\equiv N)} = \varepsilon * [CH_3CN] * l_{empty} \quad \text{(C12)}$$

where $Abs_{\nu(C\equiv N)}$ is the total absorbance area of the ν(C≡N) feature (2258 and 2296 cm^{-1}), ε is the extinction coefficient for vapor phase CH_3CN (M^{-1} mm^{-1}), $[CH_3CN]$ is the concentration of acetonitrile molecules (mol L^{-1}), and l_{empty} is the length of the path within the empty IR transmission cell (mm).

Assuming CH_3CN is an ideal gas and applying the gas law to determine $[CH_3CN]$ from the supplied pressure of CH_3CN, the extinction coefficient, ε, was measured to be 8.21 M^{-1} mm^{-1} (Figure C5).

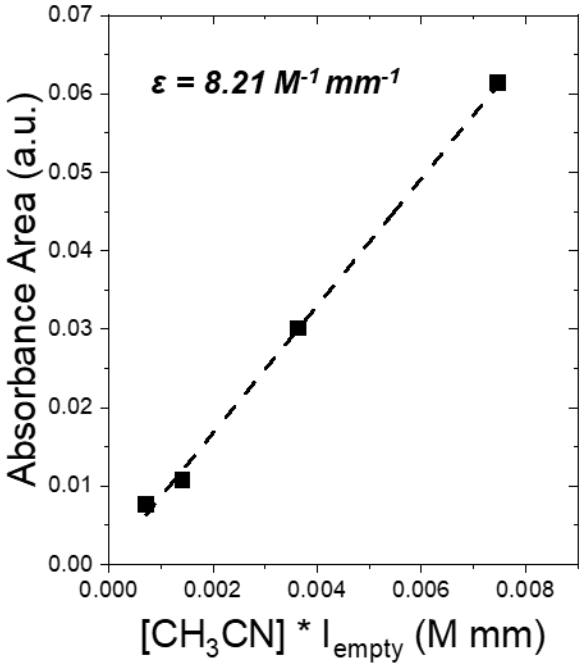

Figure C5. Absorbance area of ν(C≡N) features versus the product of CH_3CN concentration and path length to determine extinction coefficient, ε.

C3.2 Measurement and Calculation of CH_3CN displacement

Using the Beer-Lambert relationship and the measured extinction coefficient, we determine the concentration of CH_3CN, $[CH_3CN]$, in the transmission cell in the presence of a Ti-BEA pellet.

$$[CH_3CN](M) = \frac{Abs_{\nu(C\equiv N)}}{(\varepsilon * l_{pellet})} \quad \text{(C13)}$$

where $Abs_{\nu(C\equiv N)}$ is the total absorbance area of the ν(C≡N) feature (2258 and 2296 cm^{-1}), ε is the extinction coefficient for vapor phase CH_3CN (M^{-1} mm^{-1}), $[CH_3CN]$ is the concentration of acetonitrile molecules (mol L^{-1}), and l_{pellet} is the thickness of the Ti-BEA pellet inside the IR transmission cell (mm).

We report the number of CH_3CN molecules per Ti-BEA unit cell as calculated below.

$$CH_3CN\ moles\ (unit\ cell)^{-1} = [CH_3CN](M)/[unit\ cell])(M)$$

$$[unit\ cell] = \frac{number\ of\ unit\ cells}{pellet\ mass\ (mg)} * pellet\ density\ \left(\frac{mg}{mm^3}\right) * \frac{1 * 10^6\ mm^3}{L}$$

$$CH_3CN\ molecules\ (unit\ cell)^{-1} = CH_3CN\ moles\ (unit\ cell)^{-1}\left(6.022 * 10^{23}\ \frac{molecules}{mol}\right)$$

To account for variation in thickness across all pellets used, we normalize all values of $Abs_{\nu(C\equiv N)}$ by a calibration factor derived from the relationship between the number of silanols in the beam path and the total number of BEA unit cells $[unit\ cell]$, assuming uniform pellet thickness. The number of silanols in the beam path corresponds to the absorbance area of the ν(Si-O-Si) overtones (1865 cm^{-1} and 1990 cm^{-1}) of the BEA framework.[19] Since epoxide adsorption is irreverisble under these conditions, a new pellet is used when measuring CH_3CN displacement with each epoxide (C_nH_2n, n = 3,4,6,8,10). An example IR spectrum (Figure C6) shows the ν(Si-O-Si) feature, which is measured for every pellet.

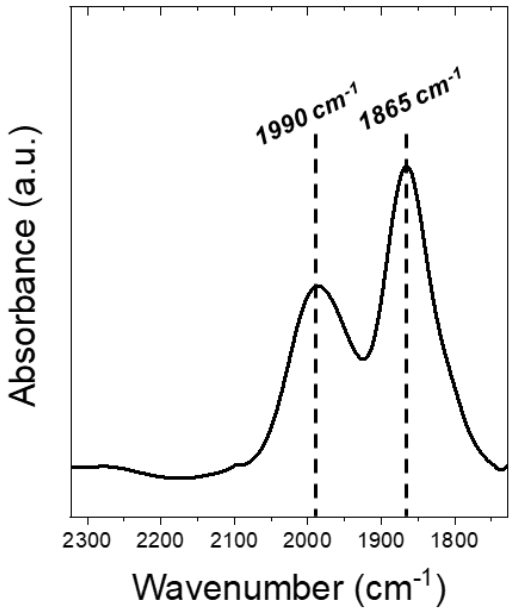

Figure C6. FT-IR absorbance spectrum of Ti-BEA (573 K in He).

C3.3 FTIR Absorbance Spectra of Ti-BEA and CH_3CN with Varying Epoxide Pressure

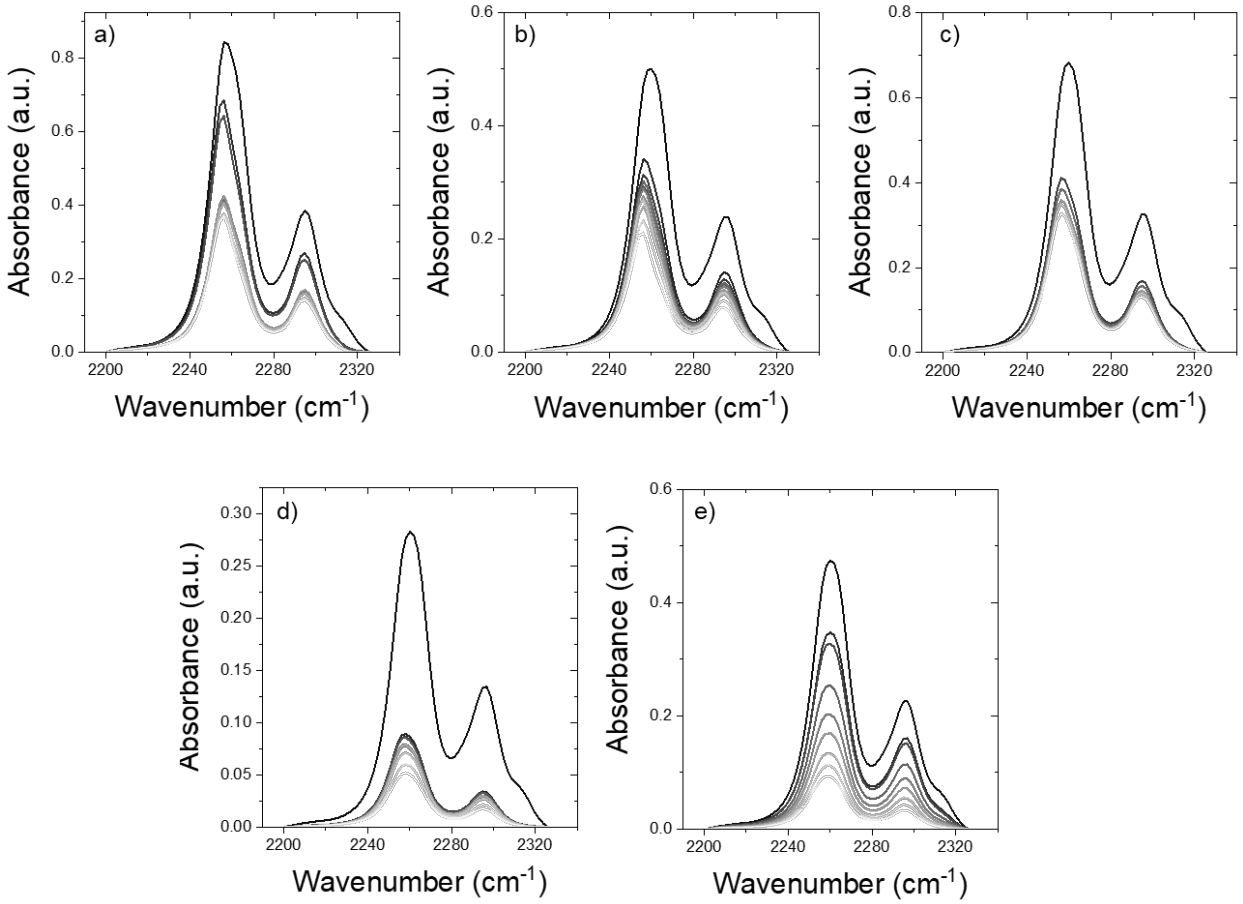

Figure C7. FT-IR absorbance spectra of Ti-BEA20 under constant CH_3CN pressure (10.3 kPa, 383 K, 22.6 sccm He) with increasing epoxide pressure (black to gray) for (a) C_3H_6O (0 – 97 kPa C_3H_6O), (b) C_4H_8O (0 - 207 Pa C_4H_8O), (c) $C_6H_{12}O$ (0 – 22 Pa $C_6H_{12}O$), (d) $C_8H_{16}O$ (0 – 59 Pa $C_8H_{16}O$) and (e) $C_{10}H_{20}O$ (0 - 48 Pa $C_{10}H_{20}O$).

IR spectra of Ti-BEA under reaction conditions (10.3 kPa CH_3CN, 383 K) while increasing epoxide partial pressure demonstrate the amount of CH_3CN molecules displaced from the zeolite pore. This resembles the formation of the epoxidation transition state for alkenes of varying chain length and the solvent reorganization that occurs during the reaction.

APPENDIX D

SUPPLEMENTAL DATA AND ANALYSIS FOR CHAPTER 5 FUTURE DIRECTIONS

D1.1 Homogeneous Trans-2-hexen-1-ol Epoxidation with TBHP and Ti-isopropoxide

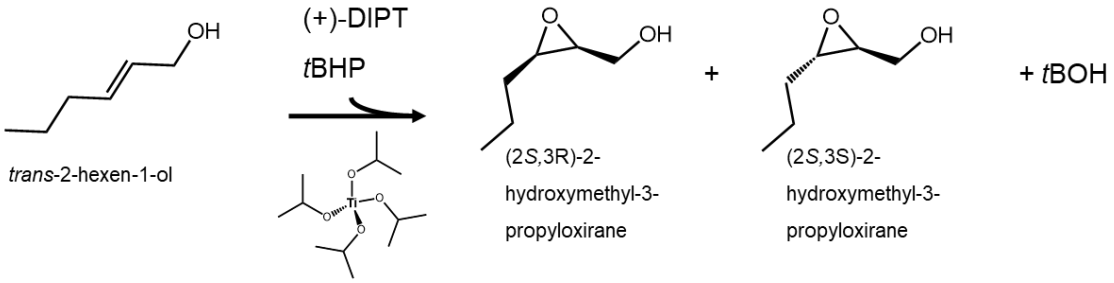

Scheme D1. Trans-2-hexen-1-ol epoxidation with TBHP and Ti-isopropoxide yields enantiomers and TBOH.

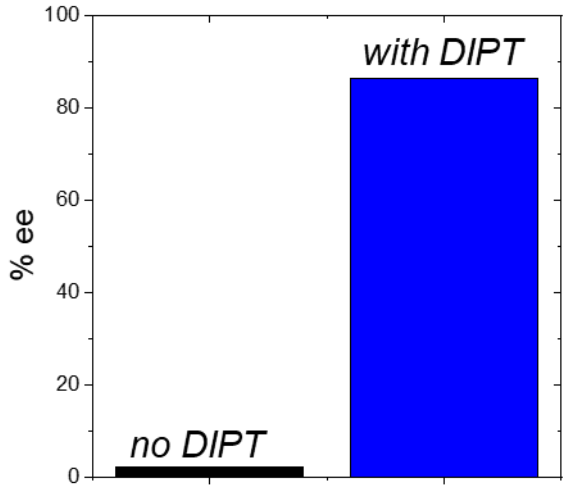

Figure D1. Enantioselectivity (ee%) for trans-hexenol epoxidation with TBHP with and without DIPT (0.0086 mol Ti, 0.1 M trans-hexenol, 0.1 M TBHP, 263 K, 3 g of 4A molecular sieves, 300 rpm).

D1.2 Enantioselective Analysis with Gas Chromatography

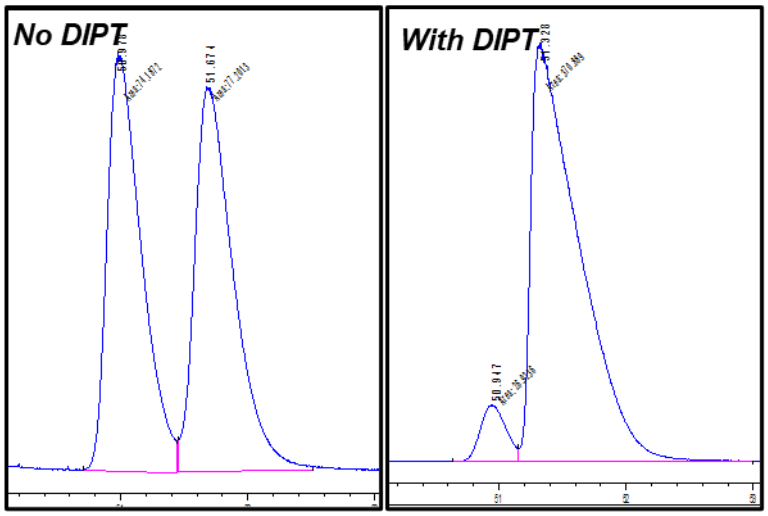

Figure D2. Gas chromatographs showing the retention times of trans-2-hexen-1-ol epoxidation products ((2*S*,3R)-2-hydroxymethyl-3-propyloxirane and (2*S*,3S)-2-hydroxymethyl-3-propyloxirane). (Agilent 5890 GC, Cyclosil-B column; Method: split Ratio: 50:1, injection volume: 0.2 ul, inlet temperature: 230ºC, FID temp: 280ºC, initial temp: 40ºC, initial hold: 5 min, ramp: 0.5ºC/min, final temp: 67ºC, final hold: 0 min).